NASA/TP-2002-211965

A Discrete-Vortex Method for Studying the Wing Rock of Delta Wings

Thomas G. Gainer
Langley Research Center, Hampton, Virginia

December 2002

The NASA STI Program Office . . . in Profile

Since its founding, NASA has been dedicated to the advancement of aeronautics and space science. The NASA Scientific and Technical Information (STI) Program Office plays a key part in helping NASA maintain this important role.

The NASA STI Program Office is operated by Langley Research Center, the lead center for NASA's scientific and technical information. The NASA STI Program Office provides access to the NASA STI Database, the largest collection of aeronautical and space science STI in the world. The Program Office is also NASA's institutional mechanism for disseminating the results of its research and development activities. These results are published by NASA in the NASA STI Report Series, which includes the following report types:

- TECHNICAL PUBLICATION. Reports of completed research or a major significant phase of research that present the results of NASA programs and include extensive data or theoretical analysis. Includes compilations of significant scientific and technical data and information deemed to be of continuing reference value. NASA counterpart of peer-reviewed formal professional papers, but having less stringent limitations on manuscript length and extent of graphic presentations.

- TECHNICAL MEMORANDUM. Scientific and technical findings that are preliminary or of specialized interest, e.g., quick release reports, working papers, and bibliographies that contain minimal annotation. Does not contain extensive analysis.

- CONTRACTOR REPORT. Scientific and technical findings by NASA-sponsored contractors and grantees.

- CONFERENCE PUBLICATION. Collected papers from scientific and technical conferences, symposia, seminars, or other meetings sponsored or co-sponsored by NASA.

- SPECIAL PUBLICATION. Scientific, technical, or historical information from NASA programs, projects, and missions, often concerned with subjects having substantial public interest.

TECHNICAL TRANSLATION. English-language translations of foreign scientific and technical material pertinent to NASA's mission.

Specialized services that complement the STI Program Office's diverse offerings include creating custom thesauri, building customized databases, organizing and publishing research results . . . even providing videos.

For more information about the NASA STI Program Office, see the following:

- Access the NASA STI Program Home Page at ***http://www.sti.nasa.gov***

- Email your question via the Internet to help@sti.nasa.gov

- Fax your question to the NASA STI Help Desk at (301) 621-0134

- Telephone the NASA STI Help Desk at (301) 621-0390

- Write to:
  NASA STI Help Desk
  NASA Center for AeroSpace Information
  7121 Standard Drive
  Hanover, MD 21076-1320

NASA/TP-2002-211965

A Discrete-Vortex Method for Studying the Wing Rock of Delta Wings

Thomas G. Gainer
Langley Research Center, Hampton, Virginia

National Aeronautics and
Space Administration

Langley Research Center
Hampton, Virginia 23681-2199

December 2002

Available from:

NASA Center for AeroSpace Information (CASI)
7121 Standard Drive
Hanover, MD 21076-1320
(301) 621-0390

National Technical Information Service (NTIS)
5285 Port Royal Road
Springfield, VA 22161-2171
(703) 605-6000

Contents

Summary

A discrete-vortex method has been developed to model the vortex flow over a delta wing and to investigate the wing rock problem associated with highly swept wings. The method uses two logarithmic vortices placed above the wing to represent the vortex flow field, but instead of the boundary conditions used in previous discrete-vortex models, it uses conditions based on conical flow, vortex rate of change of momentum, and other considerations to position the vortices and determine their strengths. For symmetric zero roll, the assumptions are that the velocity at the center of each vortex is directed radially outward from the wing axis (a conical flow requirement), that the force on the vortex system is equal to the rate of change of momentum of the vortex system, and that the maximum force on the vortex is equal to that possible with attached flow. For asymmetric nonzero roll, the strengths and positions of the vortices were determined by using additional assumptions about positions of the vortices relative to streamlines and lines of constant velocity potential. A strictly kinematic relationship based on the time analogy and conical-flow assumptions is derived in an appendix to this report and was used to determine the hysteretic positions of the vortices during rolling oscillations. The rolling moments calculated for the wing and vortex system were used in the single-degree-of-freedom equation of motion for the wing about its roll axis to generate wing rock time histories. The calculated results in this report are compared with available experimental data and analyzed to show the effects of angle of attack, wing geometry, and wing inertia on wing rock characteristics.

The results show that the method was able to model the basic features of wing rock once the static rolling moment characteristics were adjusted to agree with the experimental data. Static and dynamic vortex positions and wing rock amplitudes and frequencies were generally in good agreement with the available experimental data. The results verify that wing rock is caused by hysteretic deflections of the vortices and indicate that the stabilizing rolling moments that limit the amplitude of wing rock oscillations are essentially the result of one primary vortex moving outboard of the wing to where it has less influence on the wing.

Introduction

One of the more serious problems affecting fighter aircraft at high angles of attack is the condition known as wing rock—a high amplitude, high frequency rolling oscillation associated with the leading-edge vortex flow on highly swept wings. Wing rock can cause serious maneuvering and tracking problems and, because it involves a substantial loss of lift, also can present a potential safety hazard during takeoff and landing for both fighter and highly swept transport designs.

Although wing rock has been studied in a number of investigations (see, for example, refs. 1–16), it is still not completely understood. The experimental investigations (refs. 1–9) have indicated that wing rock is probably caused by the time lags in vortex position that occur when a wing with leading-edge vortex flow is given a roll velocity. As the wing rolls, the primary vortex on one side of the wing will move closer to the wing upper surface, while that on the other side moves away from the wing upper surface, producing an unstable rolling moment that drives the motion to higher amplitudes. The experiments, however, have not been able to show what causes the restoring moments that come into play at the higher roll angles and limit the amplitudes of wing rock oscillations. Also not known is how parameters such as wing size, sweep, and moment of inertia affect wing rock amplitudes and frequencies.

Computational studies of wing rock have not added much information beyond what has been learned experimentally. Navier-Stokes calculations for the wing rock problem are extremely difficult since they involve unsteady motions of both the wing and flow field. Although Navier-Stokes calculations of wing

rock were made in reference 10, they were for the forced oscillation of a delta wing at an angle of attack of 20°, an angle for which wing rock would not be expected to occur (see, for example, refs. 4, 7, and 9). Two-dimensional Euler calculations for a delta wing undergoing wing rock at supersonic speeds were made in reference 11, and fully three-dimensional Euler calculations were made in reference 12. These Euler calculations were able to simulate limit-cycle wing rock oscillations and show that they were the result of moment variations that were unstable at the lower wing roll angles and stable at the higher roll angles; however, neither was able to identify the underlying aerodynamic mechanisms that cause this type of rolling moment variation. Moreover, neither the Euler nor the Navier-Stokes calculations made to date have produced results that can be directly compared with available experimental data.

The discrete-vortex models developed in references 13 and 14 represent a much simpler method for studying wing rock. These models assume that the vortex flow field is dominated by two primary vortices that form above the wing and which can be represented mathematically by simple logarithmic functions. They neglect the secondary and tertiary vortices that form near the wing leading edges in a real flow and assume that vorticity is fed into the primary vortices along straight-line feeding sheets connecting the wing leading edges to the vortex centers, rather than the curved feeding sheets assumed in the more complex discrete-vortex models. Besides greatly simplifying the problem, this type of model provides better insight into the aerodynamic mechanisms involved in wing rock than the more complex methods. These models reduce the problem to an essentially three-body vibrations problem: once the positions and strengths of the vortices have been determined, the moments they produce on the wing can be determined and easily analyzed to provide a clearer picture of the aerodynamic mechanisms involved.

The problem with discrete-vortex methods, at least in the simplified form in which they are developed in references 13 and 14, is that they are inherently inaccurate. They are based on the Brown and Michael model described in reference 16, which does not give accurate vortex positions when applied to two-dimensional cylinders and cones (ref. 17) or delta wings (ref. 16), even for the basic case in which the vortices are symmetrically aligned. The models developed for wing rock, therefore, can at best be expected to provide qualitative but not quantitative results. The inaccuracies in these discrete-vortex methods are usually thought to result from the simplifying assumptions made in their development; however, the problem is not that these models oversimplified the flow field, rather the problem is that the proper boundary conditions were not applied in obtaining a solution. In reference 18, it was shown that a more accurate discrete-vortex method could be developed for cones by using boundary conditions based on conical vortex flow and the momentum of the vortex system, rather than the conditions used in the basic Brown and Michael model.

The purpose of the present paper is to show that by using a different set of boundary conditions than those used in previous discrete-vortex models, along with other constraints on vortex motion, it is possible to develop a more accurate method for studying wing rock. This new method not only can provide a more thorough understanding of the wing rock problem, but also can give reasonably accurate predictions of wing rock amplitudes and frequencies.

The method developed in this paper discards the two basic boundary conditions used in the Brown and Michael model (ref. 16) and the wing rock models of references 13 and 14. One is a Kutta condition, which requires the flow to leave smoothly from the wing leading edges; this condition is considered inapplicable because the present method neglects secondary and tertiary vortex flow. The second is a zero-force condition in which the force on an assumed feeding sheet is set equal to the force caused by induced effects at the vortex center. It replaces these two conditions with a series of others designed to determine the vortex positions and strengths during different stages of the wing rock process.

In the present method, the problem is solved first for symmetric zero roll; this is done by applying a conical flow condition, which sets the strengths of the vortices, and then applying a momentum condition, which equates the force on the vortex system to its rate of change of momentum. A maximum force condition that equates the force on the vortex system to the maximum force possible with attached flow is then applied as the third condition needed to solve the zero roll case.

Information about the streamlines on which the primary vortices lie in the symmetric case is then used to determine vortex positions and strengths with the wing at a nonzero roll angle. The vortices are assumed to move with these streamlines when the wing is rolled and also to retain their positions relative to certain velocity-potential lines that remain fixed with respect to the wing. These conditions, along with the conical flow and momentum conditions, provide the six conditions needed to solve the problem for asymmetric nonzero roll.

The final positions that the vortices assume when the wing undergoes a rolling velocity are determined by adding incremental hysteretic displacements to the calculated static positions. An equation that is based on the conical flow and time analogy assumptions and gives the hysteretic displacements in terms of static vortex position, wing roll rate, semiapex angle, and angle of attack is derived in this report.

Once the positions and strengths of the vortices have been determined in the present method, then methods based on Blasius integrations (refs. 19 and 20) are used to determine the static and dynamic rolling moments acting on the wing. These are then used in the single-degree-of freedom equation of motion for the wing about its roll axis to generate wing rock oscillations. To assess the accuracy of the method, the computed results are compared with available experimental data for ranges of angle of attack, free-stream velocity, wing geometry, and moments of inertia.

Symbols

A wing aspect ratio, $\frac{b^2}{S}$

a local semispan of wing, ft

b wing span, ft

$C_{F_{\text{attached}}}$ attached-flow force coefficient, $\frac{\text{Attached-flow force}}{qS}$, lb

C_k nondimensional vortex strength, $\frac{\Gamma_k}{2\pi a U_\infty \sin\alpha}$

C_l rolling moment coefficient, $\frac{\text{Rolling moment}}{qSb}$

$C_{l_{\text{attached}}}$ attached-flow lift coefficient, $\frac{\text{Attached-flow lift}}{qS}$

$C_{l_{\text{friction}}}$ rolling moment coefficient due to friction in roll-oscillation apparatus used in wind tunnel test

C_{l_h} rolling moment coefficient due to hysteretic effects, $\frac{l_h}{qSb}$

C_{l_p} attached-flow roll damping coefficient, $\frac{\partial C_l}{\partial\left(\frac{\dot{\phi}b}{2U_\infty}\right)}$

C_{l_s} static rolling moment coefficient, $\frac{l_s}{qSb}$

$C_l\big|_{x_k,y_k}$ static rolling moment coefficient calculated with vortex at static position x_k,y_k at given wing roll angle

$C_l\big|_{x_k+\Delta x_k,y_k}$ static rolling moment coefficient calculated with vortex at hysteretic position $x_k + \Delta x_k$,y_k at given wing roll angle

C_{l_ϕ} static spring rolling moment derivative, $\frac{\partial C_l}{d\phi}$

C_N wing normal force coefficient, $\frac{\text{Normal force}}{qS}$

C_o path of integration around closed curve in λ-plane; positive direction is that for which an observer, traveling along path, would keep enclosed area to left

C_X X-axis force coefficient, $\frac{F_X}{qS}$

C_Y Y-axis force coefficient, $\frac{F_Y}{qS}$

c wing root chord, ft

calc. calculated

d_1, d_2 centroids for vortex pairs

exp. experiment

F steady pressure force on wing, lb

F_{FS} force on feeding sheet assumed in Brown and Michael model of reference 16, lb

$F_{\max}$ maximum force in y-direction on either wing or primary vortices (see fig. 6(d)), lb

F_V force due to nonzero velocity at primary vortex center, lb

F_X steady pressure force on wing in x-direction, lb

$F_{X_{\text{unsteady}}}$ unsteady force on wing cross section in x-direction, lb

F_Y steady pressure force on wing in y-direction, lb

$F_{Y_{\text{unsteady}}}$ unsteady force on wing cross section in y-direction, lb

f oscillation frequency, cycles/sec

g influence coefficient, which, when multiplied by vortex circulation for symmetric vortex alignment, gives X-axis velocity induced at given primary vortex center by other vortices in system

h influence coefficient, which, when multiplied by vortex circulation for symmetric vortex alignment, gives Y-axis velocity induced at given primary vortex center by other vortices in system

I_l wing moment of inertia about longitudinal (roll) axis, slug-ft^2

i unit vector along imaginary axis

k constant used to account for difference between experimental rolling moments and calculated, attached-flow rolling moments

L length of wing root chord, ft

l distance along wing root chord, positive from nose rearward, ft

l_h rolling moment caused by hysteretic effects, ft-lb

l_p rolling moment caused by wing rolling velocity, ft-lb

l_s static wing rolling moment, ft-lb

MV linear momentum, lb-sec

p static pressure, lb/ft^2

q free-stream dynamic pressure, $\frac{1}{2}\rho U_\infty^2$, lb/ft^2

r_{c_k} scalar distance to primary vortex center in σ-plane, $\sqrt{x_{c_k}^2 + y_{c_k}^2}$, ft

r_o radius of cylinder in σ-plane, ft

S wing area, ft^2

t time, sec

U X-axis component of velocity that results from free-stream flow around wing at given cross section, nondimensionalized with respect to $U_\infty \sin \alpha$

U_∞ free-stream velocity, ft/sec

u	X-axis component of velocity at center of primary vortex, nondimensionalized with respect to $U_\infty \sin \alpha$
V	Y-axis component of velocity that results from free-stream flow around wing at given cross section, nondimensionalized with respect to $U_\infty \sin \alpha$
V_{max}	maximum velocity along either cylinder or $\Psi = 0$ streamline in figure 6, ft/sec
v	Y-axis component of velocity at center of primary vortex, nondimensionalized with respect to $U_\infty \sin \alpha$
W	complex potential of flow field, $\Phi + i\Psi$, ft^2/sec
$\overline{W}$	complex conjugate of W
X	coordinate axis normal to wing cross section (see fig. 1)
x	X-axis coordinate (see fig. 1)
x_c	coordinate along real axis in circle plane (see fig. 2(a))
$\bar{x}_{c_k}$	x_c distance to centroid of vortex pair consisting of vortex k and its image (see fig. 9(b))
$\bar{x}_1$	state variable, ϕ
$\bar{x}_2$	state variable, $\frac{d\phi}{dt}$
Y	coordinate axis that lies in and is parallel to plane of wing cross section (fig. 1)
y	Y-axis coordinate (fig. 1)
y_c	coordinate along imaginary axis in circle plane, ft^2/sec (see fig. 2(a))
α	wing angle of attack, deg
β	wing sideslip angle, deg
Γ_k	circulation of vortex k, positive clockwise in first ($+x$, $+y$) quadrant of X-Y plane, ft^2/sec
γ	rolling moment reduction factor, defined by equation (42)
Δx	hysteretic deflection of vortex in x-direction, ft
Δx_h	hysteretic deflection at wing trailing edge of vortex in x-direction, ft
δ	wing semiapex angle, deg
ζ	complex coordinate of primary vortex center in ζ-plane, $\xi + i\eta$, ft
η	coordinate along imaginary axis in ζ-plane, ft

θ	angle between real axis and line extending from axis origin through primary vortex center in σ-plane, deg
Λ	wing sweep, deg
λ	complex coordinate of primary vortex center in physical plane, $x + iy$, ft
λ_s	complex coordinate of separation point at wing leading edge in Brown and Michael model of reference 16, ft
$\overline{\lambda}$	complex conjugate of λ, ft
ξ	coordinate along real axis in ζ-plane, ft
ρ	fluid density, lb-sec^2/ft^4
σ	complex coordinate of primary vortex center in circle plane, $x_c + iy_c$, ft
$\overline{\sigma}$	complex conjugate of σ
Φ	velocity potential, equal to real part of complex potential, ft^2/sec
$\Phi_{\phi=0°}$	velocity potential with wing at zero roll angle, ft^2/sec
$\Phi_{k_{\phi=0°}}$	velocity potential for vortex k with wing at zero roll angle, ft^2/sec
ϕ	wing roll angle, deg
ϕ_{max}	maximum amplitude of wing rock oscillation, deg
Ψ	stream function, equal to imaginary part of complex potential, ft^2/sec
$\Psi_{k_{\phi=0°}}$	stream function defining streamline on which vortex k lies with wing at zero roll angle, ft^2/sec

Subscripts:

k	primary vortex index: 1 when referring to conditions at center of vortex 1; 2 when referring to conditions at center of vortex 2 (fig. 2)
te	wing trailing edge

Mathematical Development

Basic Assumptions

The present method makes four basic assumptions about the flow field. First, the flow is assumed incompressible and inviscid. Second, all of the vorticity generated by flow separation at the leading edge of a delta wing at an angle of attack is assumed to be concentrated in two primary vortices that form above the wing and for which the viscous core region is small enough to be neglected. Third, the flow is

assumed to be conical. This third assumption allows the problem to be treated as a two-dimensional problem in the cross-flow plane of the wing (the axis system for the wing and cross-flow plane is shown in fig. 1) and plays an important role in establishing some of the boundary conditions needed in the solution. The fourth assumption is that the two-dimensional time analogy applies. According to this analogy, changes that take place with distance, in going from cross section to cross section along the axis of a three-dimensional delta wing, are equivalent to those that would take place with time for a plate whose span is increasing with time in a two-dimensional flow field. (For an example of the use of the time analogy, see ref. 21.) This analogy allows time in the unsteady two-dimensional flow to be related to distance in the three-dimensional flow as

$$dt = \frac{dl}{U_\infty \cos\alpha} \tag{1}$$

In addition to these basic assumptions, other assumptions have been made throughout this report in connection with the development of boundary conditions and the determination of wing moments. These assumptions are indicated and discussed as they arise in the model development that follows.

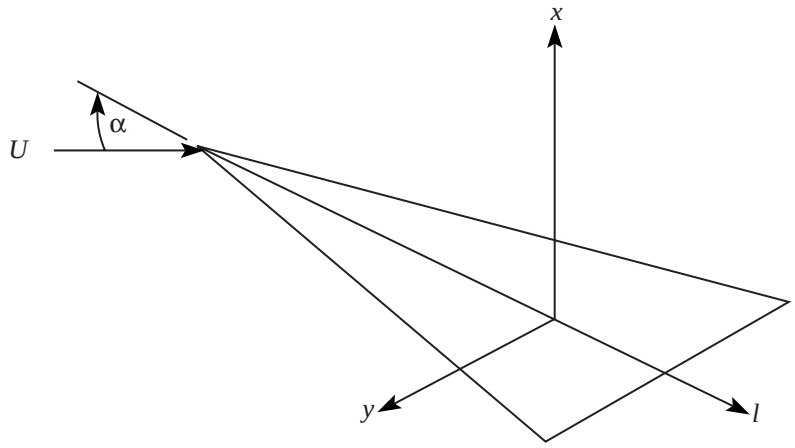

Figure 1. Wing axis system.

Basic Flow Model

General Description

Under the assumptions of an incompressible inviscid fluid, the governing equation for the flow is Laplace's equation. The problem is to find a solution in the form of a complex potential that satisfies Laplace's equation, subject to the appropriate boundary conditions. In the present method, the flow in the crossplane is first modeled in a complex σ-plane (fig. 2(a)), where the complex potential can be constructed from known elementary potential functions and a tangent flow boundary condition can be applied to the body. The flow in the σ-plane is then transformed into flow about the wing in the physical λ-plane (fig. 2(b)) where the boundary conditions on the vortices are applied. In the σ-plane, the flow model consists of two logarithmic vortices, of strengths Γ_1 and Γ_2, placed behind a two-dimensional circular cylinder (the cross-flow velocity in fig. 2 is from left to right). Image vortices, with strengths equal and opposite to those of the primary vortices, are placed inside the cylinder to satisfy the tangent-flow boundary condition at the surface.

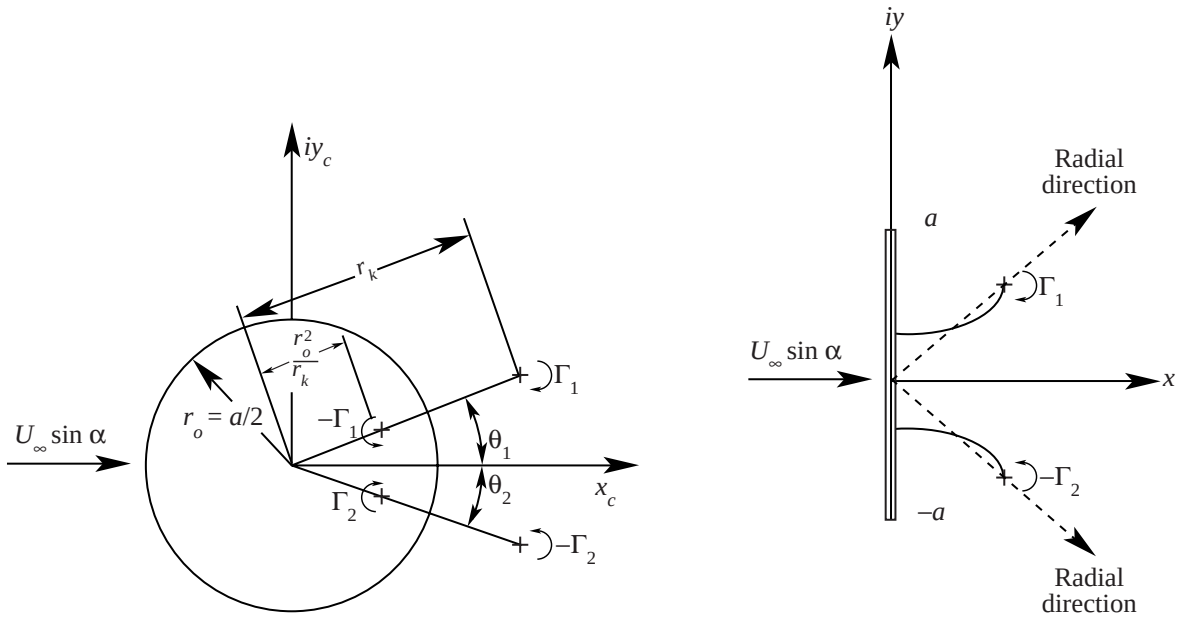

(a) σ-plane. (b) λ-plane.

Figure 2. Vortex system in σ- and λ-planes.

Complex Potential for Wing-Vortex System

For the most general case in which the vortices are asymmetrically aligned and the wing is rolled through an angle ϕ, the complex potential for the flow about the wing-vortex system in the σ-plane is

$$W(\sigma,\phi) = \Phi + i\Psi$$

$$= aU_\infty \sin\alpha \left\{ \frac{1}{2}\left[\frac{\sigma}{r_o}\left(\cos\phi + i\sin\phi\right) + \frac{1}{\dfrac{\sigma}{r_o}\left(\cos\phi + i\sin\phi\right)} \right] \right.$$

$$\left. + iC_1 \ln\left[\left(\frac{\sigma}{r_o} - \frac{\sigma_1}{r_o} \right) - \left(\frac{\sigma}{r_o} - \frac{r_o^2}{\overline{\sigma}_1} \right) \right] + iC_2 \ln\left[\left(\frac{\sigma}{r_o} - \frac{\sigma_2}{r_o} \right) - \left(\frac{\sigma}{r_o} - \frac{r_o^2}{\overline{\sigma}_2} \right) \right] \right\} \tag{2}$$

The first term in the first set of brackets on the right-hand side of equation (2) is the complex potential for a free-stream flow inclined at angle ϕ with respect to the real X_c-axis. The second term in these brackets is the complex potential for a source-sink doublet that is also aligned at angle ϕ with the real axis. The remaining terms on the right-hand side represent the contributions of the primary vortices and their images. The complex potential given by equation (2) has branch points at the centers of each primary vortex and its image and is, therefore, multivalued. It can be made single-valued—allowing a unique solution to be obtained for a given set of boundary conditions—by drawing branch cuts between the primary vortices and their images.

Coordinate and Velocity Transformations

The flow in the physical λ-plane is for a flat plate, which at zero roll is aligned perpendicularly to the free stream. The equation for transforming coordinates from the σ- to the λ-plane is

$$\frac{\lambda}{a} = \frac{1}{2}\left(\frac{\sigma}{r_o} - \frac{1}{\sigma/r_o}\right) \tag{3}$$

Transformations for going back and forth between any of the three complex planes used in the present analysis are given in appendix A.

Flow velocities in the physical plane are obtained by taking the derivative of the complex potential with respect to λ (the coordinate in the physical plane). This derivative can be written as

$$U - iV = \frac{1}{U_\infty \sin\alpha}\frac{dW}{d\lambda} = \frac{1}{U_\infty \sin\alpha}\frac{dW}{d\sigma}\frac{d\sigma}{d\lambda} = \left\{\frac{1}{2}\left[\left(\cos\phi + i\sin\phi\right) - \frac{1}{\frac{\sigma^2}{r_o^2}\left(\cos\phi + i\sin\phi\right)}\right]\right.$$

$$\left. + i\,C_1\left[\left(\frac{1}{\frac{\sigma}{r_o} - \frac{\sigma_1}{r_o}}\right) - \left(\frac{1}{\frac{\sigma}{r_o} - \frac{r_o^2}{\overline{\sigma}_1}}\right)\right] + i\,C_2\left[\left(\frac{1}{\frac{\sigma}{r_o} - \frac{\sigma_2}{r_o}}\right) - \left(\frac{1}{\frac{\sigma}{r_o} - \frac{r_o^2}{\overline{\sigma}_2}}\right)\right]\right\}\left(1 + \frac{\frac{\lambda}{a}}{\sqrt{\frac{\lambda^2}{a^2}+1}}\right) \tag{4}$$

Note that when equation (4) is used to obtain the velocity at a given vortex center, the velocities induced by that vortex on itself are neglected. For example, when the velocity at $\sigma = \sigma_1$ (the center of vortex 1) is to be determined, the term

$$\frac{1}{\frac{\sigma}{r_o} - \frac{\sigma_1}{r_o}} \tag{5}$$

which otherwise would be infinite, is set equal to zero.

Solution Procedure

The equation for the complex potential (eq. (2)) contains six unknowns: x_1, y_1, x_2, y_2 (the coordinates of the centers of the two primary vortices), C_1, and C_2 (the nondimensional strengths of the vortices). These positions and strengths can be determined by applying the appropriate boundary conditions; once they have been determined, the rolling moments caused by the vortices can be computed and used in the equation of motion for the wing-vortex system to generate wing rock oscillations. In the present method, the static vortex positions and strengths are determined first for symmetric zero roll by using motion and force restraints on the vortices, along with the equation relating the force on the vortex system to its rate of change of momentum. Information about the streamlines on which the vortices are located for the symmetric roll angle is then used to obtain vortex positions and strengths for the asymmetric nonzero roll angles. Flowcharts outlining the procedures for determining the vortex positions and strengths for zero and nonzero roll angles are presented in figures 3(a) and (b), respectively. These can be

used as the basis for generating computer codes for performing the calculations required in the present method. The boundary conditions needed to apply these procedures are stated and discussed in the following sections.

Determination of Static Vortex Positions and Strengths at Zero Roll Angle

With the wing at zero roll angle, the vortices are symmetrically aligned about the *X*-axes, so that

$$\left.\begin{aligned} x_2 &= x_1 \\ y_2 &= -y_1 \\ C_2 &= -C_1 \end{aligned}\right\} \tag{6}$$

Therefore, only the coordinates and circulation of one of the primary vortices must be determined. In the discrete-vortex methods of references 13 and 14, these three unknowns were determined by imposing a zero-force condition (which provided two of the needed equations) and a Kutta condition (which provided the third). In the present investigation, these unknowns were determined by applying three symmetric boundary conditions (S-1, S-2, and S-3) involving vortex motions and forces.

Symmetric Boundary Conditions for Wing at Zero Roll Angle

S-1. The velocity at the primary vortex centers is in the radial direction. This condition allows nondimensional vortex strength to be determined according to the equation:

$$C_1 = -C_2 = -\frac{V_1 - U_1(y_1/x_1)}{h_1 - g_1(y_1/x_1)} \tag{7}$$

S-2. The force on the vortex system in the *x*-direction (normal to the wing) is equal to the rate of change of momentum of the vortex system in the *x*-direction, a condition expressed by the equation:

$$\mathrm{Re}\left[i \oint_{C_o} \left(\frac{1}{U_\infty \sin\alpha} \frac{dW}{d\lambda} \right)^2 d\left(\frac{\lambda}{a}\right) \right] = 4\pi C_1 \left(\frac{r_{c_1}}{r_o} - \frac{1}{r_{c_1}/r_o} \right) \sin\,\theta_1 \frac{\tan\delta}{\tan\alpha} \tag{8}$$

where the integration in equation (8) is carried out around a path C_o that includes only the two primary vortices.

S-3. The maximum lateral force for the flow is equal to the maximum lateral force that would be exerted at the wingtip in attached flow, a condition expressed by the equation:

$$\left| \frac{i}{2}\ \mathrm{Im}\left[\oint_{C_o} \left(\frac{1}{U_\infty \sin\alpha} \frac{dW}{d\lambda} \right)^2 d\left(\frac{\lambda}{a}\right) \right] \right| = \pi \tag{9}$$

The term on the left-hand side of equation (9) is the absolute value of the computed force coefficient; the path of integration is taken around only one of the primary vortices and not around any other singularity in the flow field.

These three boundary conditions are applied according to the procedure outlined in figure 3(a), and are discussed in detail in the next sections.

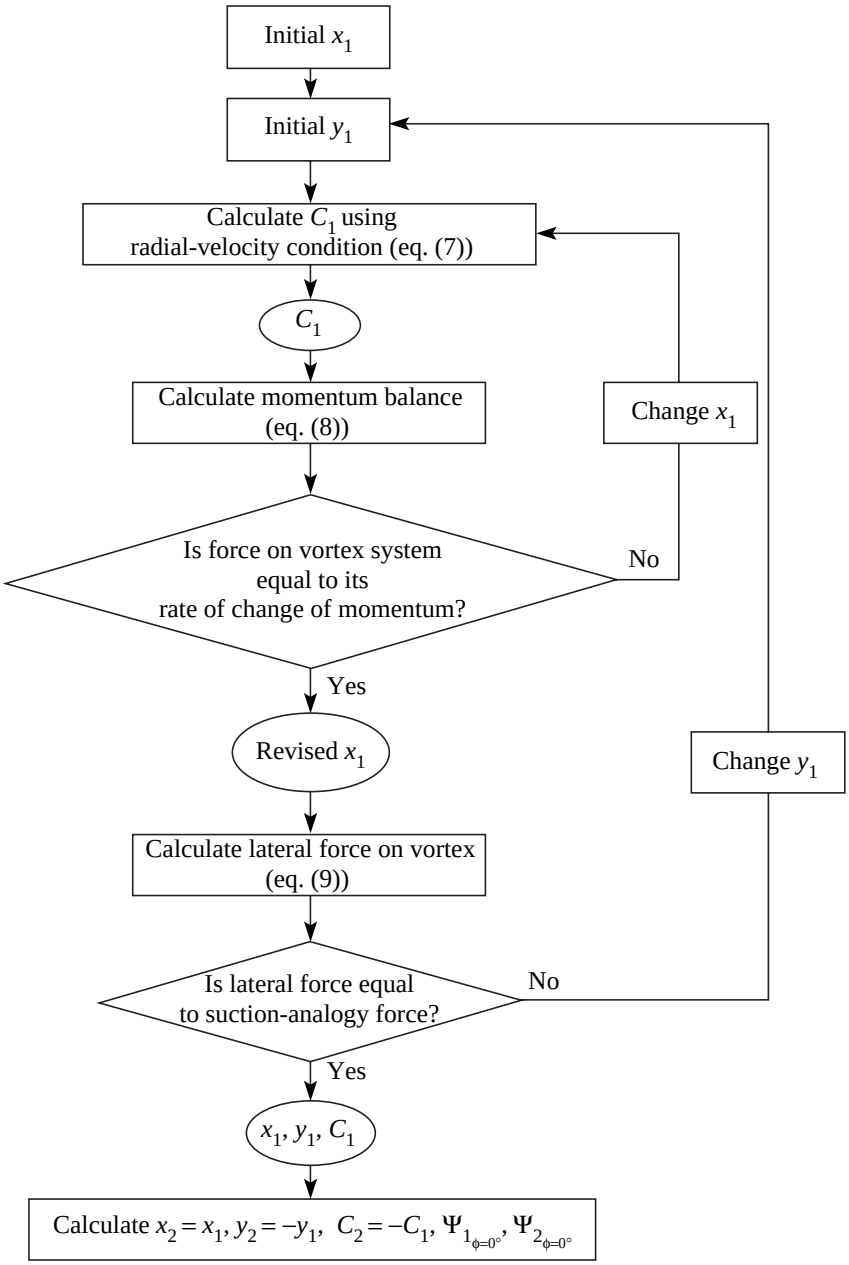

(a) Zero roll angle.

Figure 3. Flowcharts of procedure for determining static vortex positions and strengths.

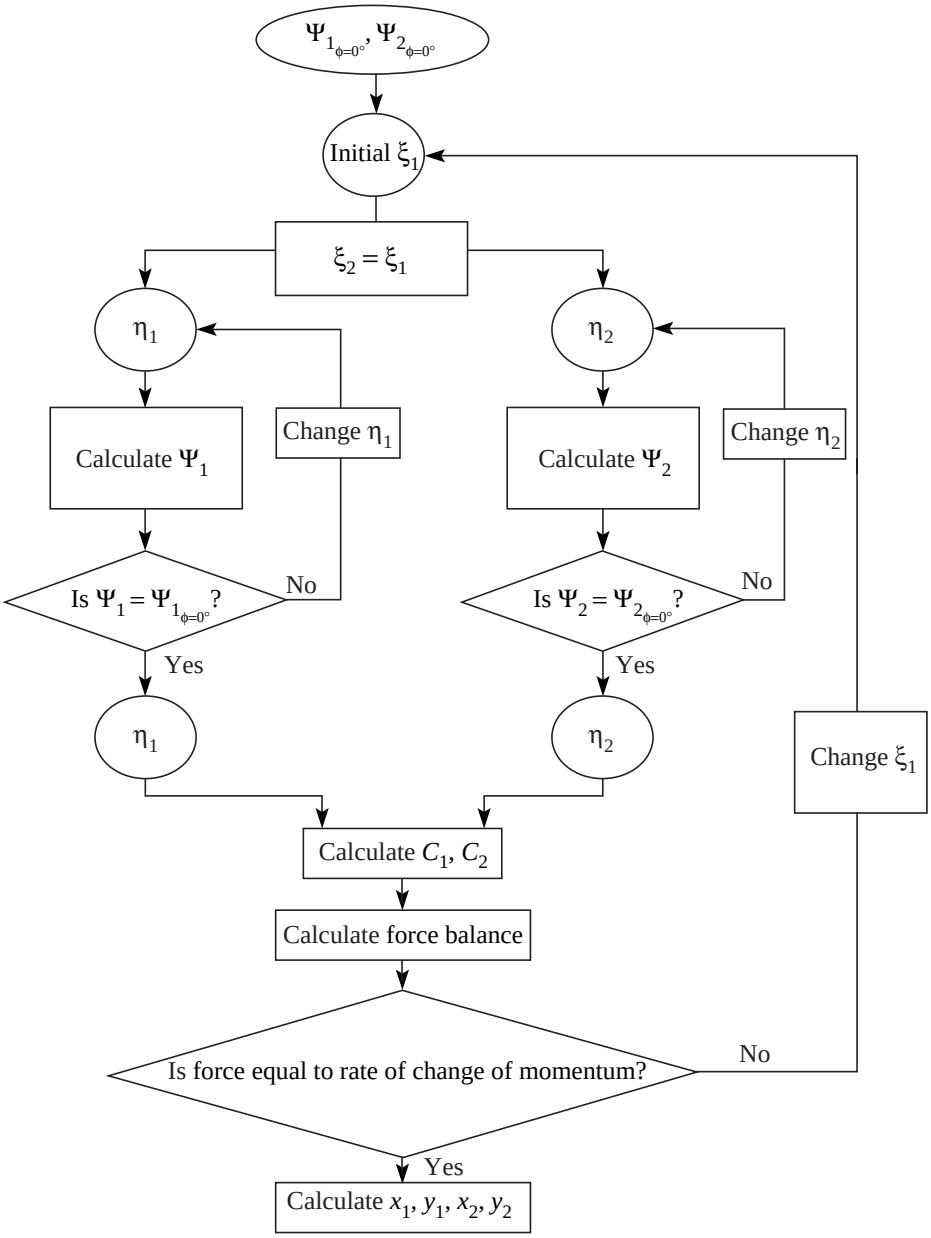

(b) Nonzero roll angle.

Figure 3. Concluded.

Discussion of Symmetric Boundary Conditions

Radial-Velocity Condition (S-1). The radial-velocity condition is one of the conditions imposed for cones in reference 18 and determines the vortex circulation for a given vortex location. It is based on the fact that the conical flow assumption for a delta wing requires the vortex centers to move radially away from the centerline of the three-dimensional wing as the vortices progress from one cross section of the wing to the next. Since the primary vortices are assumed to be free vortices, each moving in the direction of the local flow velocity at its center, this condition is satisfied if the local induced velocity at the center of each primary vortex is directed radially outward, along a line that extends from the center of the plate through the vortex center (see fig. 2(b)).

To determine the vortex circulation using this condition, the x- and y-components of the velocity (see eq. (4)) at the center of one of the primary vortices are first written in the form of a free-stream component plus an influence coefficient times the nondimensional circulation of the vortices as follows:

$$v_1 = V_1 + h_1 C_1 \tag{10}$$

$$u_1 = U_1 + g_1 C_1 \tag{11}$$

Then if the velocity is radial, the slope v_1/u_1 of the velocity vector must equal the slope y_1/x_1 of the line running from the origin through the vortex center; that is:

$$\frac{v_1}{u_1} = \frac{V_1 + h_1 C_1}{U_1 + g_1 C_1} = \frac{y_1}{x_1} \tag{12}$$

Collecting terms gives

$$\left(h_1 - g_1 \frac{y_1}{x_1} \right) C_1 = -\left(V_1 - U_1 \frac{y_1}{x_1} \right) \tag{13}$$

Solving for C_1 gives equation (7).

Applying the radial-velocity condition will give the nondimensional vortex strength for any assumed value of x_1 and y_1. This operation is performed in the top part (down through the element C_1) of the flowchart in figure 3(a). Contour lines showing the positions that the vortices would take for specified values of nondimensional vortex strength are shown in figure 4.

***X*-Axis Momentum Condition (S-2).** Equation (8) is the equation of motion for the vortex system. It replaces the zero-force condition of the Brown and Michael (ref. 16) and Bryson (ref. 17) models in which it was assumed that the force on the straight-line feeding sheet connecting each primary vortex to a separation point on the body is balanced by the force caused by induced effects at the vortex center. In the Brown and Michael and related models, these feeding sheets serve as the branch cuts needed to make the complex potential for the vortex system single-valued, and, as such, are subjected to a force (see ref. 17). Across such a branch cut, the velocity potential Φ changes by the amount Γ, the vortex circulation, so that when Γ changes with time, the pressure difference across the sheet is

$$dp = \rho \frac{d\Phi}{dt} = \rho \frac{d\Gamma_k}{dt} \tag{14}$$

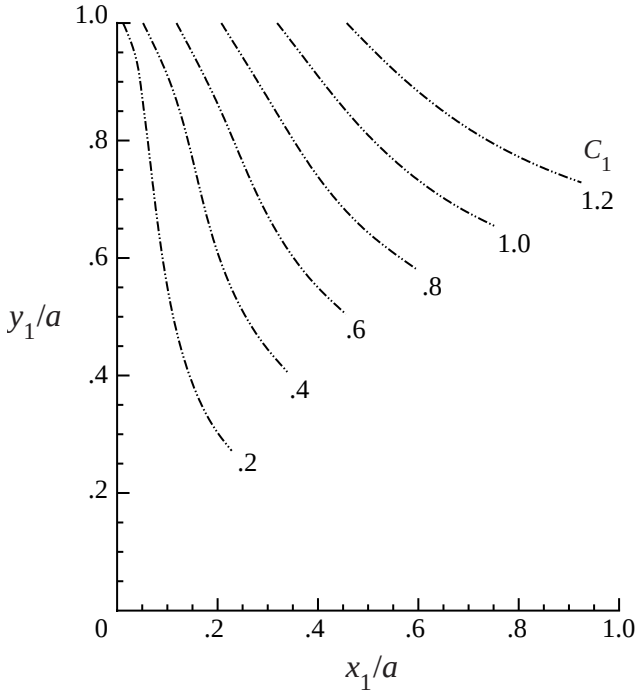

Figure 4. Lines of constant circulation in *X*-*Y* plane.

When integrated over the length of the feeding sheet, this pressure difference results in a pressure force of

$$F_{FS} = -i\rho \frac{d\Gamma_k}{dt}\left(\lambda_k - \lambda_s\right) \tag{15}$$

In the Brown and Michael model, this pressure force is balanced by a force resulting from a nonzero velocity at the vortex center, a force given by the Kutta-Joukowski theorem as

$$F_v = i\rho\Gamma_k\left(V_k - \frac{d\lambda_k}{dt}\right) \tag{16}$$

Setting the sum of forces F_{FS} and F_V equal to zero gives the zero-force conditon used in the basic Brown and Michael model as

$$-i\rho \frac{d\Gamma_k}{dt}\left(\lambda_k - \lambda_s\right) + i\rho\Gamma_k\left(V_k - \frac{d\lambda_k}{dt}\right) = 0 \tag{17}$$

Although the Brown and Michael zero-force condition has been used extensively in discrete-vortex models, it is not a valid condition. As indicated in appendix B, the force on the feeding sheet is an unsteady force caused by changes in vortex strength and, as such, should not be balanced by a steady force at the vortex center.

Instead of using the Brown and Michael condition, the present method specifies a force balance by equating the *X*-axis force on the vortex system to the rate of change of momentum in the *x*-direction of the vortex system. (In the *y*-direction, the net force and the rate of change of momentum of the vortex system are both zero for the zero roll case; therefore a *Y*-axis momentum equation would not provide any useable

information.) In the x-direction, the force on the vortices obtained by Blasius integration (see eq. (B1) of appendix B) can be expressed in nondimensional form as

$$\mathrm{Re}\left[\frac{i}{2}\oint_{C_o}\left(\frac{1}{U_\infty \sin\alpha}\frac{dW}{d\lambda}\right)^2 d\left(\frac{\lambda}{a}\right)\right]\sin^2\alpha \tag{18}$$

where the integration is carried out around a closed path C_o, taken in the counterclockwise direction, that encircles the two primary vortices but not any other singularities. The force on the wing, which can be obtained by integrating around a path that includes the wing but not the vortices, will be equal and opposite to this force on the vortices.

The rate of change of momentum of the vortex system is determined in the σ-plane (see fig. 2(a)), where the primary vortices appear as pure logarithmic vortices whose complex potential has the form

$$W(\sigma) = \frac{\Gamma_k}{2\pi}\ln(\sigma - \sigma_k) \tag{19}$$

For a pair of vortices with this mathematical form, the momentum is equal to $\rho\Gamma$ times the distance between the two vortices. That is, in the σ-plane, the momentum in the direction of the real axis for a vortex pair consisting of the upper primary vortex and its image is equal to

$$MV = i\rho\Gamma_k\left(r_k - \frac{r_o^2}{r_k}\right)\sin\theta_k \tag{20}$$

In the direction of the real axis, the total momentum for the two pairs forming the vortex system is twice the momentum calculated in equation (20).

The rate of change of momentum of the vortex system can be written in terms of conditions at vortex 1, for which the circulation is positive, as

$$\frac{d(MV)}{dt} = 2\rho\Gamma_1\frac{d}{dt}\left(r_1 - \frac{r_o^2}{r_1}\right)\sin\theta_1 + 2\rho\frac{d\Gamma_1}{dt}\left(r_1 - \frac{r_o^2}{r_1}\right)\sin\theta_1 \tag{21}$$

As discussed in appendix B, the unsteady force caused by changes in vortex circulation (the second term on the right-hand side of eq. (21)) is exactly equal to the rate of change of momentum caused by changes in vortex circulation, regardless of where the vortex center is located. No new information can be obtained, therefore, by equating force caused by changes in circulation to the rate of change of momentum caused by changes in circulation. In the present analysis, therefore, neither the unsteady force caused by changes in vortex circulation nor the change in momentum resulting from changes in circulation is considered when determining vortex position.

Equation (21), without the term for rate of change of circulation, can also be written as

$$\frac{d(MV)}{dt} = 2\rho\Gamma_1\frac{d}{dr_o}\left(r_1 - \frac{r_o^2}{r_1}\right)\sin\theta_1\frac{dr_o}{da}\frac{da}{dl}\frac{dl}{dt} \tag{22}$$

By making the substitutions $r_o = a/2, da/dl = \tan\delta,$ and $dl/dt = U_\infty \cos\alpha,$ equation (22) can be written as

$$\frac{d(MV)}{dt} = \rho\Gamma_1 \frac{d}{dr_o}\left(r_1 - \frac{r_o^2}{r_1}\right)\sin\ \theta_1 \tan\delta\ U_\infty \cos\alpha \tag{23}$$

In evaluating the derivative with respect to r_o in equation (23), it should be noted that r_1 can be written as $r_1 = r_o(r_1/r_o)$, and that the quantity (r_1/r_o) is constant for each station of the delta wing in conical flow; hence, $dr_1/dr_o = r_1/r_o$. Thus, equation (23) can be written as

$$\frac{d(MV)}{dt} = \rho\Gamma_1\left(\frac{r_1}{r_o} - \frac{1}{r_1/r_o}\right)\sin\ \theta_1 \tan\delta\, U_\infty \cos\alpha \tag{24}$$

In nondimensional form this becomes

$$\frac{1}{\rho U_\infty^2 a}\frac{d(MV)}{dt} = 2\pi\left(\frac{r_1}{r_o} - \frac{1}{r_1/r_o}\right)C_1 \sin\ \theta_1 \frac{\tan\delta}{\tan\alpha}\sin^2\alpha \tag{25}$$

Equating this nondimensional change in momentum to the force coefficient given by equation (18) yields the momentum equation for the symmetric vortex system, given by equation (8).

For a given value of tan α/tan δ, equation (8) will be satisfied for certain values of x_1 and y_1, the vortex coordinates in the physical plane. As shown in the flowchart of figure 3(a), once initial values of x_1 and y_1 have been specified, C_1 can be determined from the radial-velocity boundary condition (S-1), and x_1 can be iterated to get the final values of x_1 and y_1 that will satisfy equation (8). Contours of constant tan α/tan δ, obtained by applying the X-axis momentum condition, are shown along with the constant C_k contours, obtained by applying the radial-velocity condition, in figure 5.

Maximum Lateral Force Condition (S-3). Conditions S-1 and S-2 would provide the information needed to determine vortex positions and strength—if the circulation produced by the flow separation at the wing leading edge were known. For cones in reference 18, this circulation was calculated as being proportional to the square of the edge velocity at the separation points on the cone, and although the locations of the separation points on the cone surface could not be determined using the method of reference 18, they could be approximated with available experimental data. The velocities at these separation points, as well as at all points on the cone surface, are finite, and the circulation being made available for vortex formation could be calculated.

For delta wings, on the other hand, although the flow is known to separate at the sharp leading edges of the wing, the velocity at the separation points, at least in the present model, is infinite. Therefore, separation point velocities cannot be used to calculate the vortex circulation. Condition S-3 is a way of working around this problem. Instead of determining vortex positions and strengths by calculating the circulation made available for vortex formation, they are determined by putting a limit on the maximum force that can be produced on the wing by the flow field around it. This condition assumes this force cannot exceed the leading-edge suction force that the wing would develop with completely attached flow.

Condition S-3 is strictly an assumption, presented without proof, but is analogous to the maximum-velocity condition imposed for a two-dimensional circular cylinder with trailing vortex flow in reference 22. Figure 6 illustrates this analogy by presenting attached- and separated-flow velocity

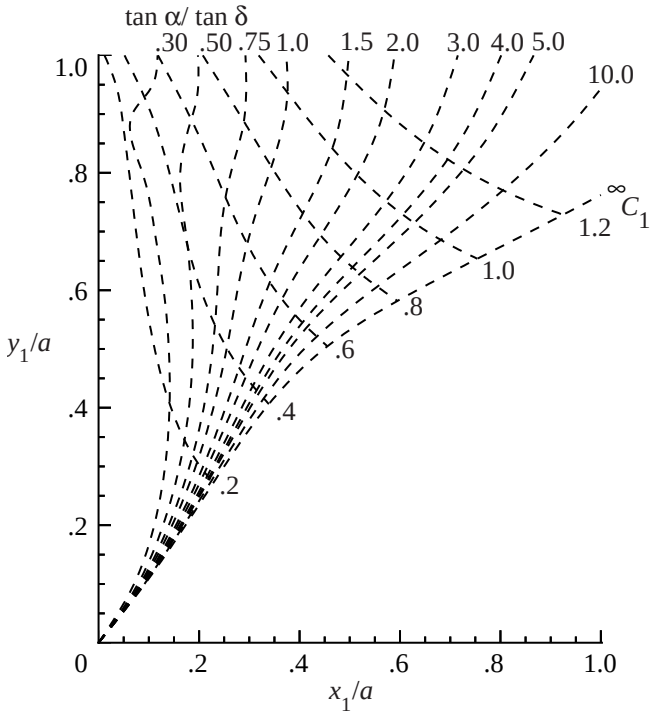

Figure 5. Lines of constant circulation and of constant tan α/tan δ.

distributions for the circular cylinder of reference 22 (figs. 6(a) and (b)) with typical attached- and separated-flow force distributions computed for the delta wing cross section by Blasius integrations (figs. 6(c) and (d)).

To obtain solutions in reference 22, the assumption is that when the flow behind the cylinder separates and forms into vortices, the maximum flow velocity possible with vortex flow should be the same as that for the cylinder with attached flow. As shown in figure 6(a), with attached flow, the flow velocity reaches a maximum value of $2U_\infty$ at the points $x = 0$, $y/r_o = \pm 1$ on the surface of the cylinder; with separated flow (fig. 6(b)), it reaches a maximum at a point that lies above and slightly behind the vortex center on the $\Psi = 0$ streamline that surrounds each vortex. In reference 22 the assumption is that this maximum velocity, regardless of where it occurs in the vortex flow field, must still be equal to $2U_\infty$ as shown in figure 6(b). For this velocity to be higher than $2U_\infty$ would mean that the vortices were adding energy to the outer flow instead of deriving their energy from it.

Condition S-3 is a similar condition but places a limit on the forces acting at the delta wing cross section, rather than on the velocities. The maximum vortex force for a delta wing with attached flow is that given by the Polhamus leading-edge suction analogy (ref. 23). This force can be determined by Blasius integrations around half the wing cross section, and for a flat-plate cross section it has a value at each leading edge (in coefficient form) of $(\pi/2)\sin^2\alpha$, as shown in figure 6(c). (These forces, according to the Polhamus leading-edge suction analogy, turn 90° to become the normal force on the wing.) This force arises from the fact that although there are infinite velocities and pressures at the leading edges of the wing with attached flow, they act over an essentially zero area to produce a finite lateral force.

With separated flow (fig. 6(d)), there is still an infinite velocity but a finite force at the leading edge because a Kutta condition is not being satisfied in the present model; however, these calculated forces are

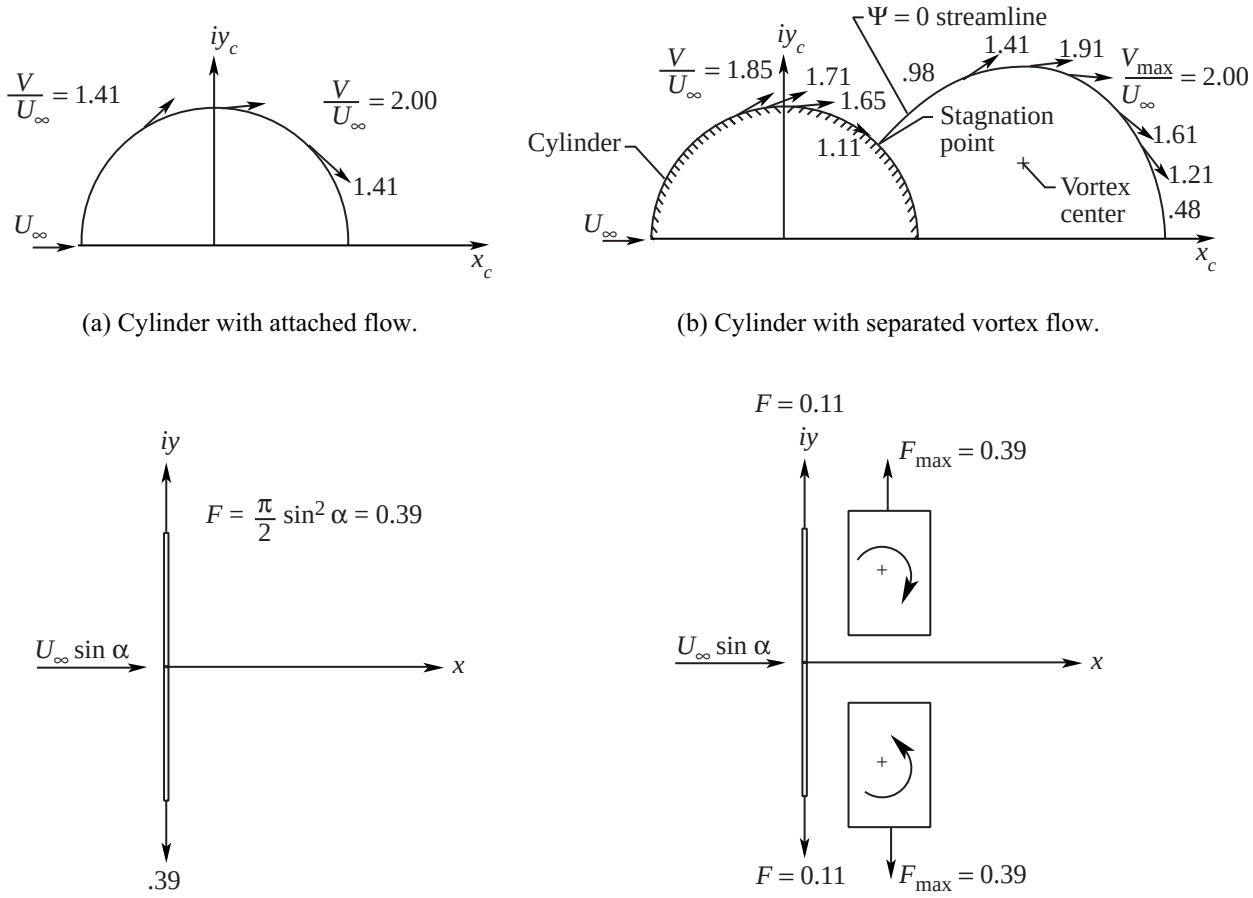

(a) Cylinder with attached flow.

(b) Cylinder with separated vortex flow.

(c) Delta wing cross section with attached flow; $\alpha = 30°$.

(d) Delta wing cross section with separated vortex flow; $\alpha = 30°$.

Figure 6. Maximum-force condition assumed in present model.

no longer the maximum forces, which occur instead at the vortex locations. For $\alpha = 30°$ shown in figure 6(d), for example, the lateral force coefficient at each leading edge of the cross section is equal to only 0.11, whereas the maximum lateral force coefficient occurs at each primary vortex center and is assumed to have a value of 0.39 (the value of $(\pi/2) \sin^2 \alpha$ at $\alpha = 30°$). Setting the total of the lateral force for the two primary vortices equal to the leading-edge force for attached flow gives the condition expressed by equation (9).

The steps in applying this boundary condition are included in the bottom part of the flowchart in figure 3(a). The vortex center locations for the symmetric case are found by iterating along a curve for a given $\tan \alpha / \tan \delta$, such as one of those shown in figure 5, until an x_1, y_1 location is found for which equation (9) can be satisfied. The resulting curve, labeled "Vortex center locations" in figure 7, represents the locus of vortex centers for which all three of the previously described boundary conditions are satisfied simultaneously.

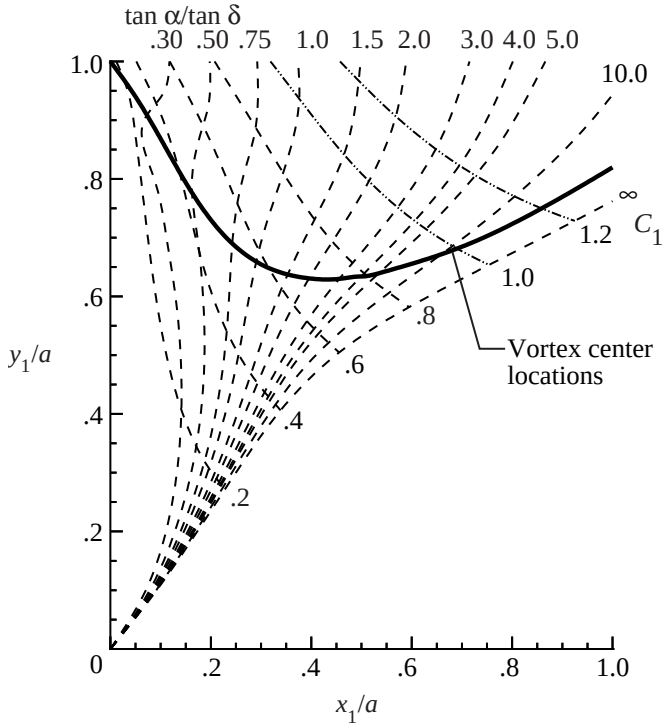

Figure 7. Calculated line of vortex center locations for symmetric vortex flow.

Determination of Static Vortex Positions and Strengths at Nonzero Roll Angle

When the wing is rolled, the primary vortices become asymmetrically aligned and have different circulation strengths (see fig. 8); consequently, all six unknowns in the equation for the complex potential (eq. (2)) must be solved for instead of only three. In the present method these unknowns were determined by applying the six asymmetric boundary conditions (AS-1–AS-6) stated and discussed in the following sections. The first three conditions involve assumptions about how the primary vortices position themselves in response to changes taking place in the underlying potential-flow field when the wing is rolled; the remaining three consist of radial-velocity and momentum conditions similar to those applied in the symmetric case.

Asymmetric Boundary Conditions for Wing at Nonzero Roll Angle

AS-1. Vortex 1 remains on the same attached-flow streamline, deflecting laterally with the streamline, as the wing is rolled. That is,

$$\Psi_1 = \Psi_{1_{\phi=0^\circ}} \tag{26}$$

AS-2. Vortex 2 remains on the same attached-flow streamline, deflecting laterally with the streamline, as the wing is rolled. That is,

$$\Psi_2 = \Psi_{2_{\phi=0^\circ}} \tag{27}$$

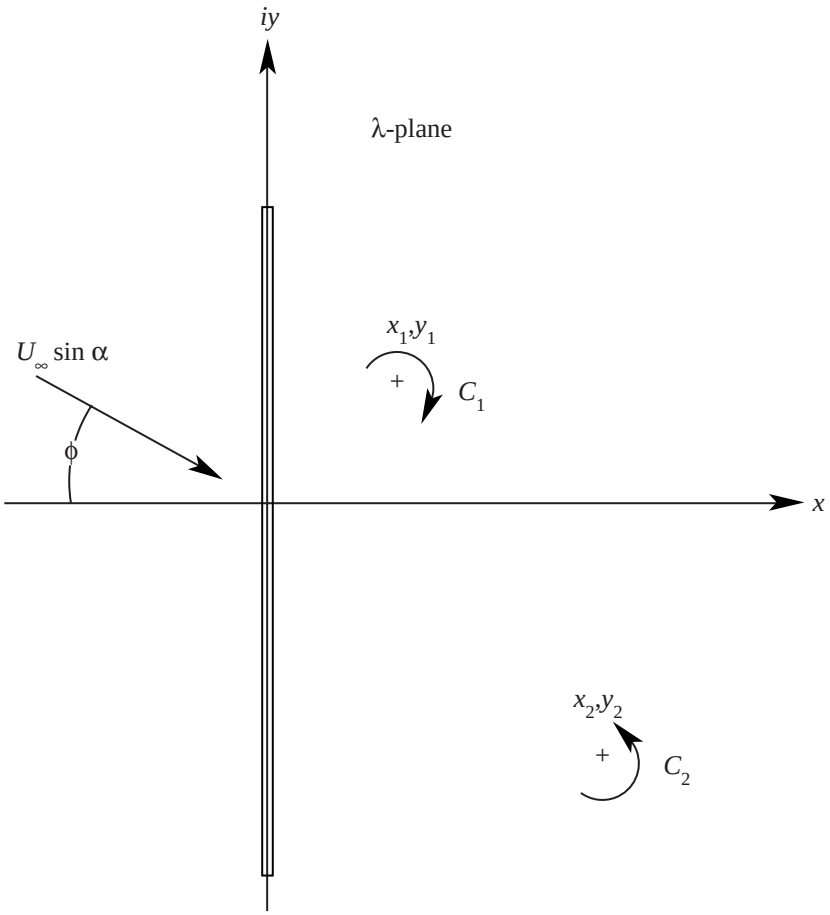

Figure 8. Asymmetric vortex arrangement with wing at nonzero roll angle.

AS-3. At any given roll angle, the two primary vortices both lie on one of the velocity-potential lines defined for the body without vortex flow at a zero roll angle. In the σ-plane where the cross-flow velocity is $U_\infty \sin \alpha$, these lines are defined by (ref. 18)

$$\Phi_{\phi=0^\circ} = -U_\infty \sin\alpha \, x_c \left(1 + \frac{r_o^2}{r_c^2}\right) \tag{28}$$

In the ζ-plane, this condition is met if the two primary vortices lie along the same ξ = Constant line; that is, if

$$\xi_1 = \xi_2 \tag{29}$$

AS-4. The velocity at the center of vortex 1 is in the radial direction.

AS-5. The velocity at the center of vortex 2 is in the radial direction.

AS-6. The force on the vortex system, in the direction normal to the wing cross section, is equal to the rate of change of momentum of the vortex system, in the direction normal to the wing. This condition is expressed by the equation:

$$\mathrm{Re}\left[i \oint_{C_o} \left(\frac{1}{U_\infty \sin\alpha} \frac{dW}{d\lambda} \right)^2 d\left(\frac{\lambda}{a} \right) \right] = 2\pi i \left[C_1 \left(\frac{r_{c_1}}{r_o} - \frac{1}{r_{c_1}/r_o} \right) \sin\theta_1 + C_2 \left(\frac{r_{c_2}}{r_o} - \frac{1}{r_{c_2}/r_o} \right) \sin\theta_2 \right] \frac{\tan\delta}{\tan\alpha} \tag{30}$$

Discussion of Asymmetric Boundary Conditions

Attached-Flow Streamline Conditions (AS-1 and AS-2). These two conditions are based on the assumption that the changes in vortex position when the wing is rolled reflect changes in the underlying potential-flow field when the wing is rolled. Streamlines of this underlying flow field are shown in figure 9 for the ζ- and σ-planes (appendix A), the two complex planes for which the vortices can be represented mathematically as pure logarithmic vortices.

The surrounding flow field in these planes can be considered to consist of the two primary vortices imposed on a basic attached flow—the flow that would exist if there were no separation and no vortex formation. In the σ-plane, the flow streamlines are defined, in the general case where the free stream is inclined at an angle ϕ with respect to the X_c-axis, by the equation:

$$\Psi = -U_\infty \sin\alpha \left(x_c \sin\phi + y_c \cos\phi \right) \left[1 - \frac{a^2}{\left(x_c \cos\phi - y_c \sin\phi \right)^2 + \left(x_c \sin\phi + y_c \cos\phi \right)^2} \right] \tag{31}$$

Figures 9(a) and (b) show representative attached-flow streamlines for the zero roll case; rolling the wing in the present model amounted to rotating the free-stream velocity and these streamlines through an angle ϕ with respect to the body-fixed axes, as shown in figures 9(c) and (d). At a zero roll, the primary vortices are located along the $\Psi_{1_{\phi=0^\circ}}$ = Constant and $\Psi_{2_{\phi=0^\circ}}$ = Constant streamlines, which are shown as dashed lines in figure 9. Conditions AS-1 and AS-2 assume that these primary vortices will stay on these streamlines and rotate with them as the wing roll angle changes. For example, calculations made in this report show that at $\alpha = 30°$, vortex 1 lies on the streamline $\Psi_{1_{\phi=0^\circ}} = 0.31$, and vortex 2 lies on the streamline $\Psi_{2_{\phi=0^\circ}} = -0.31$. Thus, at $\alpha = 30°$, the two primary vortices will continue to lie on these respective streamlines regardless of the roll angle.

Constant Velocity-Potential Condition (AS-3). This condition is a result of the flow field being irrotational. When the wing roll angle changes and the primary vortices move with the streamlines as the streamlines rotate through the angle ϕ (as required by conditions AS-1 and AS-2), they must do so in such a way that the vortex system as a whole does not rotate with respect to the body. That this requirement can be expressed in terms of lines of constant velocity potential can be seen by examining the definition of these lines in ζ- and σ-planes used in the present analysis.

In the ζ-plane, the velocity potential for $\phi = 0°$ is given by

$$\Phi_{\phi=0^\circ} = U_\infty a \sin\alpha \frac{\xi}{a} \tag{32}$$

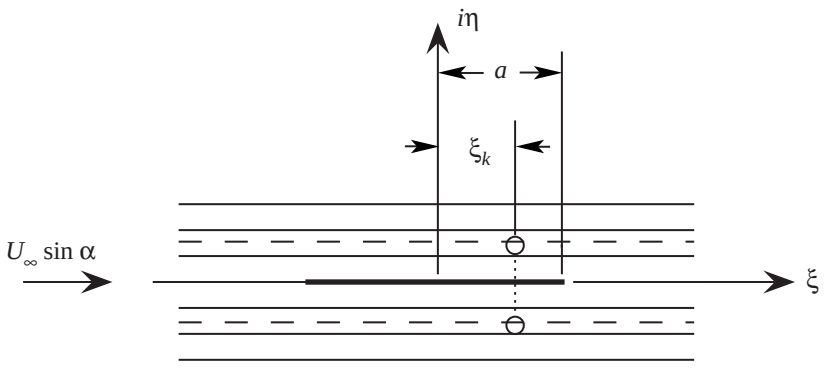

(a) ζ-plane; zero roll angle.

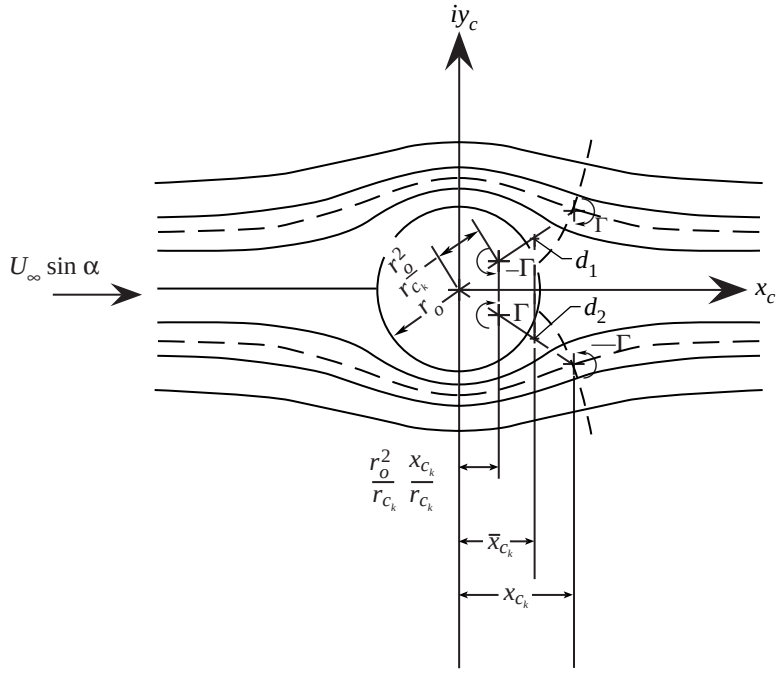

(b) σ-plane; zero roll angle.

Figure 9. Streamline and vortex arrangement for flow in ζ- and σ-planes at zero and nonzero roll angles.

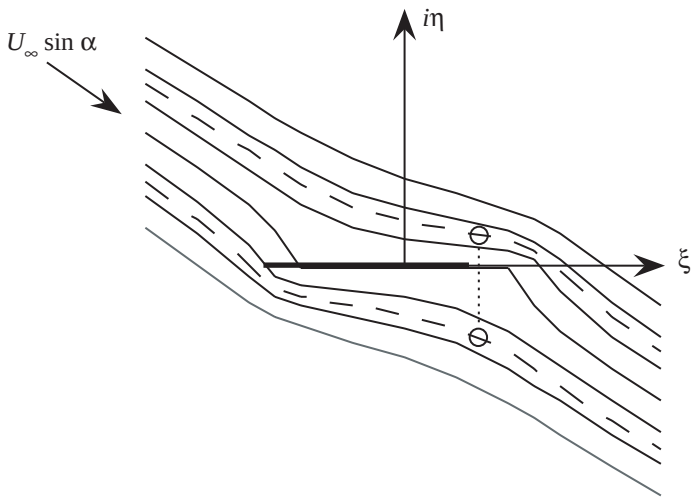

(c) ζ-plane; nonzero roll angle.

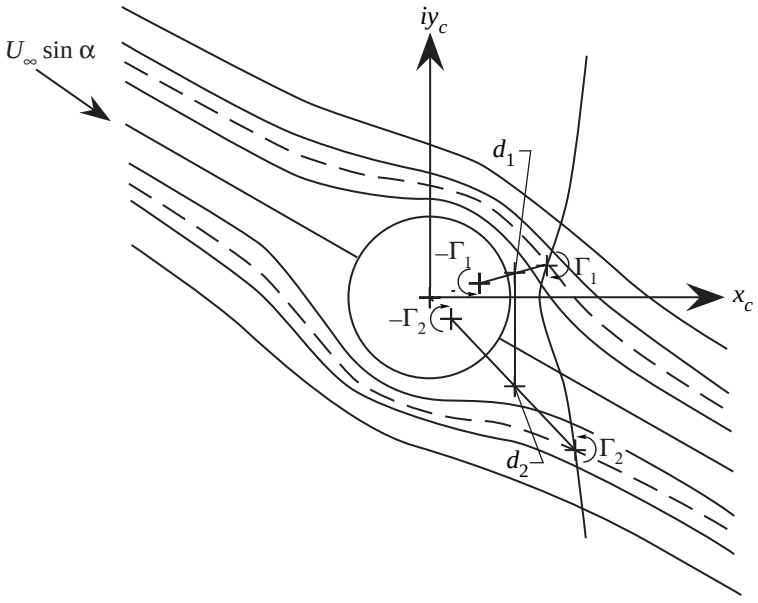

(d) σ-plane; nonzero roll angle.

Figure 9. Concluded.

and in the σ-plane, it is given by

$$\Phi_{\phi=0^\circ} = U_\infty \sin\alpha\, x_c \left(1 + \frac{r_o^2}{r_c^2}\right) \tag{33}$$

Therefore, if in the ζ-plane the center of one of the primary vortices is located on the velocity-potential line $\Phi_{k_{\phi=0^\circ}}$, then according to equations (32) and (33) the nondimensional distance ξ_k/a to this vortex center can be written as (see also fig. 9(b))

$$\frac{\xi_k}{a} = \frac{\Phi_{k_{\phi=0^\circ}}}{aU_\infty \sin\alpha} = \frac{x_{c_k}}{2r_o}\left(1 + \frac{r_o^2}{r_{c_k}^2}\right) = \frac{1}{r_o}\left[\frac{1}{2}\left(x_{c_k} + \frac{r_o^2}{r_{c_k}}\frac{x_{c_k}}{r_{c_k}}\right)\right] = \frac{\bar{x}_{c_k}}{r_o} \tag{34}$$

Hence, while in the ζ-plane, ξ_k/a represents the nondimensional distance to a line of constant non-dimensionalized velocity potential, that is, the velocity potential divided by $aU_\infty \sin\alpha$ (see fig. 9(a)), in the σ-plane it represents the distance to the centroid of the vortex pair formed by a primary vortex and its image (see fig. 9(b)). (Note that because the two vortices are of equal and opposite strength, this centroid lies midway between the primary vortex and its image.) The centroids for the two vortex pairs are designated d_1 and d_2, respectively, in figure 9.

Consequently, if the two primary vortices always lie on a common $\Phi_{k_{\phi=0^\circ}}$ line regardless of the wing roll angle—that is, if

$$\Phi_{1_{\phi=0^\circ}} = \Phi_{2_{\phi=0^\circ}} \tag{35}$$

then in the ζ-plane,

$$\frac{\xi_1}{a} = \frac{\xi_2}{a} \tag{36}$$

and there will be no rotation of the two primary vortices (compare fig. 9(a) with fig. 9(b)). In the σ-plane, there will be no rotation of the line between d_1 and d_2 that connects the centroids of the two vortex pairs. That is, the relationship

$$\frac{\bar{x}_{c_1}}{r_o} = \frac{\bar{x}_{c_2}}{r_o} \tag{37}$$

will apply, so that the line between d_1 and d_2 will always remain parallel to the iY_c-axis (which corresponds to the plane of the wing in the λ-plane) as the wing roll angle changes (compare fig. 9(b) with fig. 9(d)). Applying condition AS-3 will ensure there is no rotation of the complete vortex system in either the ζ- or σ-planes, where the vortices are represented as pure logarithmic vortices. This condition should also ensure irrotationality in the λ-plane, where because of the conformal transformation involved, the vortices can no longer be considered pure logarithmic vortices.

Radial-Velocity Conditions (AS-4 and AS-5). AS-4 and AS-5 are the same conditions as condition S-1 for the symmetric case, but are applied separately at the centers of the two asymmetrically aligned primary vortices. Applying these conditions gives two equations similar to equation (13) for the symmetric case, but each equation contains the circulation strengths of the two vortices. These two equations can then be solved simultaneously to determine the two strengths. The procedure for solving these equations is described in reference 18.

Momentum Condition (AS-6). Boundary condition AS-6 is the same as condition S-2 for the symmetric case, except that it is applied here to asymmetrically aligned vortices. Equation (30) represents the more general form of equation of motion for the vortex system, containing the coordinates and circulation strengths of two vortices instead of just one vortex.

Application of Nonzero Roll Boundary Conditions

The basic mechanism by which the two primary vortices move with respect to the wing when the wing is rolled is that they move with the underlying potential flow streamlines as these streamlines change directions with respect to the wing (conditions AS-1 and AS-2); furthermore, they must both always remain along one of the velocity-potential lines that is fixed with respect to the wing (condition AS-3). The procedure for determining the static vortex positions and strengths at any given roll angle that result from this type of movement is that outlined in the flowchart of figure 3(b).

The procedure assumes that for a given wing at a given angle of attack and roll angle, the streamlines for $\phi = 0°$ have been obtained by applying the symmetric boundary conditions. It begins in the ζ-plane (see fig. 9(a)) where the ξ = Constant lines, which correspond to constant $\phi = 0°$ velocity-potential lines and do not change with roll angle, are straight lines running perpendicular to the real axis. The streamlines, which do change with roll angle, are defined by

$$\Psi = aU_\infty \sin\alpha \left[\frac{\eta}{a} \cos\phi + \mathrm{Im}\left(i\sqrt{\left(\frac{\xi}{a} + i\frac{\eta}{a}\right)^2 - 1} \right) \sin\phi \right] \tag{38}$$

A ξ = Constant line, along which the two primary vortices are assumed to lie, is chosen in the ζ-plane, and by iterating on η at this value of ξ using equation (38), a value of Ψ can be found that matches the Ψ value for the symmetric case. This process is completed for both primary vortices and establishes tentative ξ and η coordinates for the primary vortex centers. The vortex circulations can be determined by transferring these coordinates to the λ-plane and applying the radial-velocity conditions AS-4 and AS-5. The momentum condition AS-6 (eq. (30)) is then applied, and if the force on the vortices is not equal to the rate of change of momentum of the vortex system, then another value of ξ is selected and the process is repeated. By iterating on ξ in this way, values of ξ_1,η_1 and ξ_2,η_2 can be found for which conditions AS-3 through AS-6 are satisfied, and from these values the vortex center coordinates x_1,y_1 and x_2,y_2 can be determined in the real λ-plane.

The vortex positions in all three planes considered in the present analysis that result from applying this procedure are shown for wing roll angles of 0°, 22.5°, and 45° in figure 10. The x- and y-coordinates of the vortex centers determined by the previously described method are given in table 1 for wing roll angles from –52.5° to +52.5° and angles of attack from 10° to 40°.

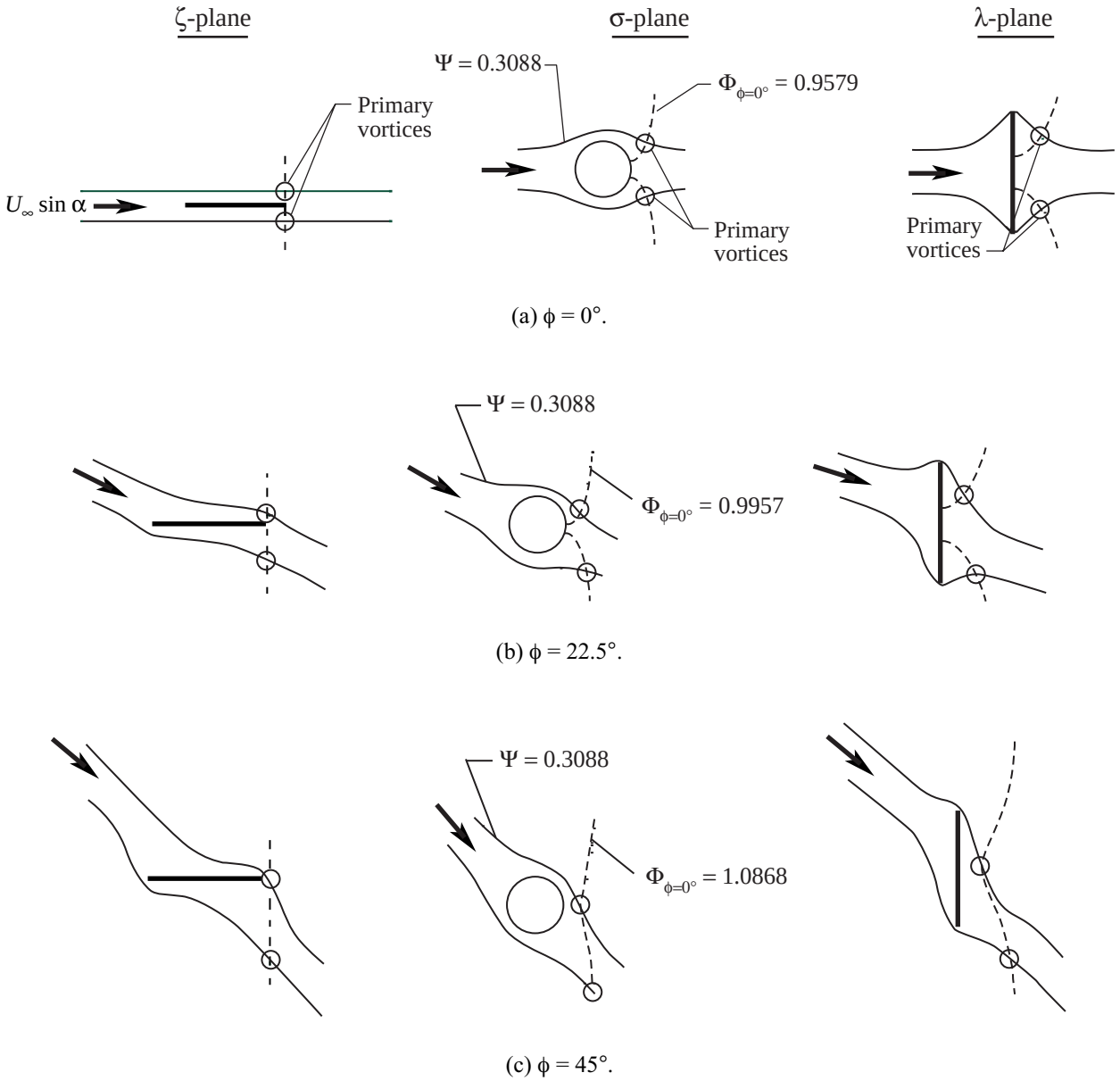

Figure 10. Vortex positions with roll angle shown in three complex planes used in present analysis.

Determination of Dynamic Vortex Positions and Strengths

The experimental data indicate that a hysteretic effect on vortex position probably causes wing rock (see, e.g., refs. 1–4). When the wing is given a rolling velocity, the primary vortices move away from their static positions at a given roll angle; for a positive rolling velocity, the vortex on the side of the down-going wing will move away from the wing and above its static position, while the vortex on the side of the up-going wing will move toward the wing and below its static position. These displacements cause incremental rolling moments, which, at the lower roll angles at least, are destabilizing. In the present method, the hysteretic deflections are modeled as displacements of the primary vortices from their

static positions; the displacements are determined from the strictly kinematic relationship derived in appendix C. Equation (C8) of appendix C gives the displacement in the *x*-direction as

$$\frac{\Delta x_k}{a} = \frac{y_k}{a}\left(\frac{\dot{\phi} b}{2U_\infty \sin\alpha}\right)\left(\frac{\tan\alpha}{2\tan\delta}\right) \tag{39}$$

The hysteretic displacement in the *y*-direction was assumed to be zero, an assumption that is consistent with the experimental data of references 1 and 4.

As derived in appendix C, the hysteretic deflection is equal to the product of the nondimensional lateral coordinate of the vortex center, the nondimensional roll rate of the wing, and a nondimensional time that is constant for the wing and can be expressed in terms of the quantity tan α/tan δ. Equation (C8) assumes each primary vortex is approaching the wing at a velocity of $y_k \dot{\phi}$ while the wing remains stationary. Using equation (C8) to compute hysteretic effects eliminates the need to employ a source-sink distribution on the cylinder surface in the σ-plane (the procedure used in refs. 13 and 14 to simulate unsteady flow conditions) and greatly simplifies the computational procedure.

The strengths of the primary vortices in their hysteretic positions were computed by applying the radial-velocity conditions at each vortex center as described previously.

Determination of Wing Rolling Moments

Calculating the wing rolling moments was a problem in developing the present method because the model, which uses just the two primary vortices to represent the vortex flow field, neglects the secondary and tertiary vortices that, in a real (viscous) flow, form near the wing leading edges. In a real flow, these secondary and tertiary vortices help smooth out the flow at the leading edges so that a Kutta condition can be met. Without these vortices, calculated velocities and pressures at the leading edges are infinite, so that Blasius integrations around the wing to obtain wing rolling moments do not give the correct values. To overcome this problem, methods that did not rely on integrations around the wing had to be used to compute the wing rolling moments.

Static Rolling Moments

The static rolling moments in this report were computed by using equation (D2) given in appendix D, but with the equation modified by multiplying the right-hand side by a constant *k*. This modified equation gives the static rolling moment coefficient for a given wing angle of attack and roll angle as

$$C_l = -k\frac{\pi}{3}\sin^2\alpha\ \sin\phi\ \cos\phi \tag{40}$$

In this equation, *k* is a constant used to account for the difference between the calculated attached-flow rolling moments and the experimental moments and is thought to be necessary to account for wing thickness effects (as is discussed further in the sections on wing rock results).

Moments Caused by Hysteretic Deflections of Vortices

The wing rolling moment increments resulting from hysteresis in the present method were calculated by the method outlined in appendix D, which involved Blasius integrations around the two primary vortices instead of around the wing. The formula used to compute hysteretic moments was

$$C_{l_h} = k\gamma\, \Delta C_{l_h} \tag{41}$$

In this equation, k is the same constant used in calculating static rolling moments, as described previously, and accounts for the difference between calculated and experimental rolling moments. The parameter γ in equation (41) is a reduction factor used to reduce the rolling moments obtained by integrating around the vortices to the level of those developed by the wing, as described in appendix D. This parameter is a function of $\tan\alpha/\tan\delta$ (fig. D6) and could be approximated by

$$\gamma = 0.00024962 + 0.1019(\tan\alpha/\tan\delta) - 0.019932(\tan\alpha/\tan\delta)^2 + 0.001942(\tan\alpha/\tan\delta)^3 \tag{42}$$

The incremental coefficient ΔC_{l_h} in equation (41) is the incremental moment caused by hysteresis in the vortex position and was obtained by using the general Blasius equation for moments (ref. 19), which, in coefficient form, can be written for the wing rolling moment as

$$C_l = \frac{-1}{6}\mathrm{Re}\left[\oint_{C_o} \frac{\lambda}{a}\left(\frac{1}{U_\infty \sin\alpha}\frac{dW}{d\lambda}\right)^2 d\left(\frac{\lambda}{a}\right)\right]\sin^2\alpha \tag{43}$$

The incremental moments were obtained by performing two Blasius integrations: one with the primary vortices in their static positions x_k,y_k at a given wing roll angle, and the second with them in their displaced positions $x_k + \Delta x_k,y_k$ at a given roll angle and roll rate. The incremental moment due to hysteresis was then the difference between these two values:

$$\Delta C_{l_h} = C_l\Big|_{x_k+\Delta x_k,y_k} - C_l\Big|_{x_k,y_k} \tag{44}$$

Attached-Flow Roll Damping

Just as a basic attached-flow lift must be added to the vortex lift to get the total lift on a delta wing with vortex flow, there is similarly a basic attached-flow roll damping associated with a wing undergoing a roll velocity. The theorectial value for the attached-flow roll damping coefficient, as derived by Ribner in reference 24, is

$$C_{l_p} = -\frac{\pi A}{32} \tag{45}$$

In the wing rock calculations in the present paper, this attached-flow damping was added to that caused by hysteretic effects on vortex position to get the total damping due to roll.

Wing Rock Calculations

To simulate wing rock oscillations, the vortex positions, strengths, and wing rolling moments, obtained as described previously, were used in the single-degree-of-freedom equation of motion for the delta wing about its roll axis:

$$I_z\ddot{\phi} + l_p\dot{\phi} + l_{\text{friction}} + l_h + l_s = 0 \tag{46}$$

This equation can be written in nondimensional form as

$$\frac{I_z\ddot{\phi}}{qSb} + C_{l_p}\frac{\dot{\phi}b}{2U_\infty} + C_{l_{\text{friction}}} + C_{l_h} + C_{l_s} = 0 \tag{47}$$

In this equation, C_{l_p} is the attached-flow roll damping coefficient, the damping for the wing without vortex flow given by equation (45). The symbol $C_{l_{\text{friction}}}$ is the rolling moment coefficient due to friction in the roll-oscillation apparatus used in a particular wind tunnel test, and C_{l_h} is the increment in rolling moment coefficient caused by hysteretic displacements of the vortices, described in the section "Moments Caused by Hysteretic Deflections of Vortices." The symbol C_{l_s} is the static rolling moment, given by the suction analogy as

$$C_{l_s} = -k\frac{\pi}{3}\sin^2\alpha\,\sin\phi\cos\phi \tag{48}$$

To solve this equation, it was put into state variable form by setting

$$\left.\begin{aligned}\bar{x}_1 &= \phi\\ \bar{x}_2 &= \dot{\phi}\end{aligned}\right\} \tag{49}$$

This form allowed the second-order differential equation to be expressed as two first-order equations:

$$\left.\begin{aligned}\dot{\bar{x}}_1 &= \bar{x}_2\\ \dot{\bar{x}}_2 &= -\left(C_{l_p}\frac{\bar{x}_2 b}{2U_\infty} + C_{l_{\text{friction}}} + C_{l_h} + C_{l_s}\right)\frac{qSb}{I_z}\end{aligned}\right\} \tag{50}$$

In the present method, these equations were subject to the constraints:

$$\left.\begin{aligned}\frac{x_k + \Delta x_k}{a} &= \frac{x_k}{a} + \frac{y_k}{a}\left(\frac{\bar{x}_2 b}{2U_\infty\sin\alpha}\right)\left(\frac{\tan\alpha}{2\tan\delta}\right)\\ \frac{y_k}{a} &= \frac{y_k}{a}\end{aligned}\right\} \tag{51}$$

which are the equations specifying the hysteretic positions of the vortices.

These equations were solved using a Runge-Kutta scheme, which went through the following steps in generating oscillation time histories:

1. The procedure was started at $t = 0$, $\dot{\phi} = 0$, and with an initial value of ϕ (1° in most of the calculations made in this report)

2. $\ddot{\phi}$ was computed from equation (47)

3. $\ddot{\phi}$ was integrated over an incremental time Δt to get $\dot{\phi}$, and then $\dot{\phi}$ was integrated over Δt to get ϕ

4. The quantities x_k, y_k, C_k, C_{l_s}, and $C_l|_{x_k,y_k}$ were determined at the new value of ϕ

5. The new value of $\dot{\phi}$ was used to compute the product of $C_{l_p} \frac{\dot{\phi} b}{2U_\infty}$ and the hysteretic deflection Δx_k

6. Values of C_k were determined with the vortex centers at $x_k + \Delta x_k, y_k$, and those values were used to compute $C_l|_{x_k+\Delta x_k,y_k}$ and C_{l_h}

7. The time was then set to $t + \Delta t$, and the sequence repeated until a complete time history was obtained

The static vortex positions x_k and y_k were fed into the equations in the form of cubic-spline curve fits to the data of tables 1(a)–(h). These curve fits gave x_k and y_k as functions of ϕ and were provided for each of the angles of attack covered by the tables. The vortex circulation strengths for each primary vortex were calculated at each time step by assuming a radial velocity at each vortex center (conditions AS-4 and AS-5). The calculations were made for ranges of angle of attack, free-stream velocity, wing sweep, and moment of inertia that covered those of the available experimental data.

Results and Discussion

Static Vortex Positions and Strengths for Zero Roll Angle

As shown in figure 11, static vortex positions at zero roll angle are generally in good agreement with experimental data and Navier-Stokes calculations (from refs. 2, 11, and 25–29): except at the lower values of tan α/tan δ, the experimental vortex centers line up along the line of vortex centers determined by the present method. The experimental data are for wings with different sweeps tested over different ranges of angle of attack. Figure 12 shows that the agreement with experimental data for the present method is much better than with either the Brown and Michael (ref. 16) or the Legendre (ref. 30) methods, which place the vortex centers much farther outboard than the present method.

Figure 13 shows the calculated and experimental (from refs. 2, 25, 26, and 27) y- and x-locations as functions of tan α/tan δ. At the lower values of tan α/tan δ, the vortex center locations determined by the present method are farther outboard and away from the wing than the experimental values. These differences between calculation and experiment could probably be attributed to the fact that the present method neglects the secondary and tertiary vortices which, in the real flow, would fill the space between the wing and the primary vortices. At the higher values of tan α/tan δ, where the primary vortices become dominant, the agreement between calculation and experiment is quite good. The experimental data indicate that wing rock would be expected to occur at values of tan α/tan $\delta \geq 2.0$.

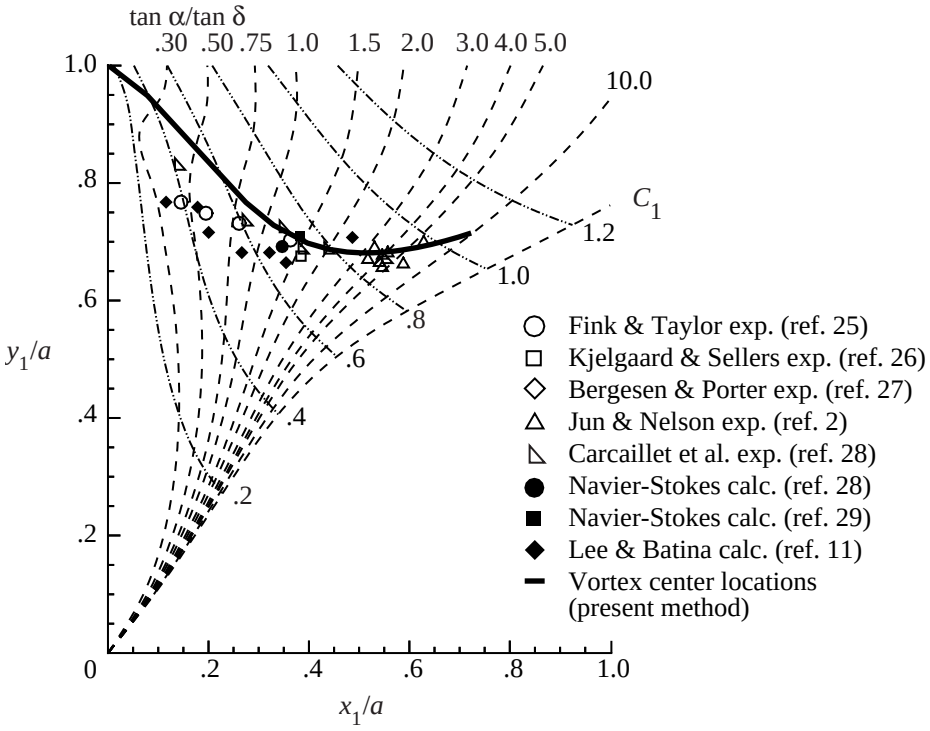

Figure 11. Experimental and calculated vortex center locations.

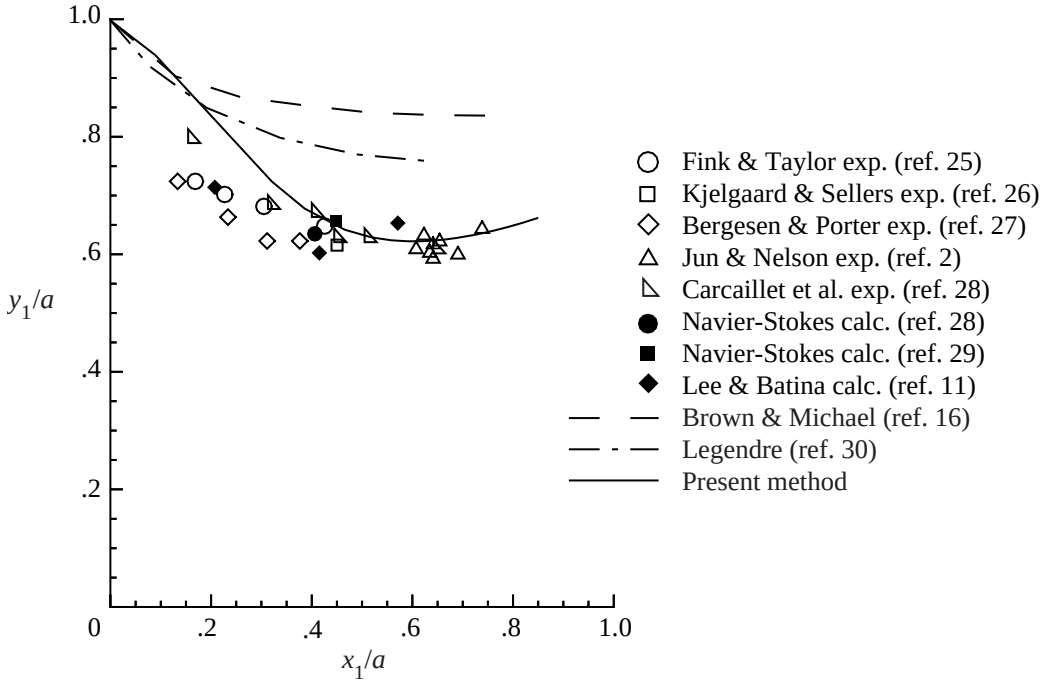

Figure 12. Present method, Brown and Michael, and Legendre methods.

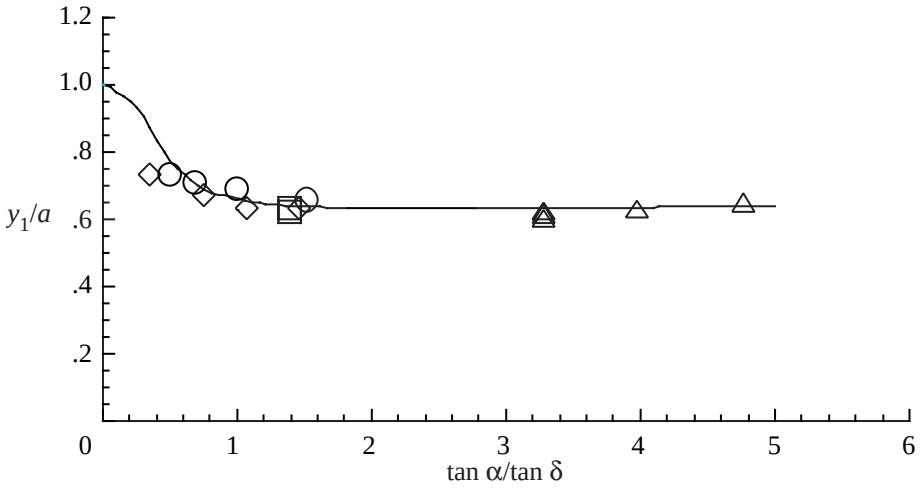

(a) y_1/a.

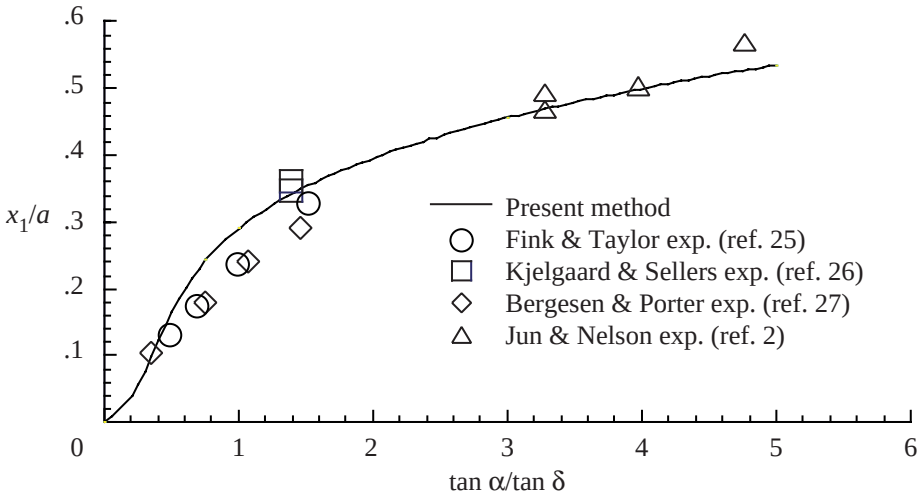

(b) x_1/a.

Figure 13. Calculated and experimental x- and y-locations as functions of tan α/tan δ.

The present calculations showed that the circulation for delta wings could be defined by the single curve of C_k versus tan α/tan δ shown in figure 14 (values of C_k from this curve are presented in table 2). Although the vortex circulation Γ varies directly with distance along a delta wing, for an assumed conical flow the value of C_k (defined as $C_k = \Gamma/2\pi a U_\infty \sin\alpha$) will be the same at each cross section, and therefore is a constant for the wing. The curve in figure 14 allows the value of C_k to be determined for any given wing at any given angle of attack.

Figure 14 presents the calculated values of C_k with experimental values obtained from reference 31 and shows that values from reference 31 are higher over most of the tan α/tan δ range. However, the experimental values in figure 14 were obtained by using a cross-wire anemometer, which is an intrusive technique. These values represent the maximum measured in the tests and may contain the effects of secondary and tertiary vortices.

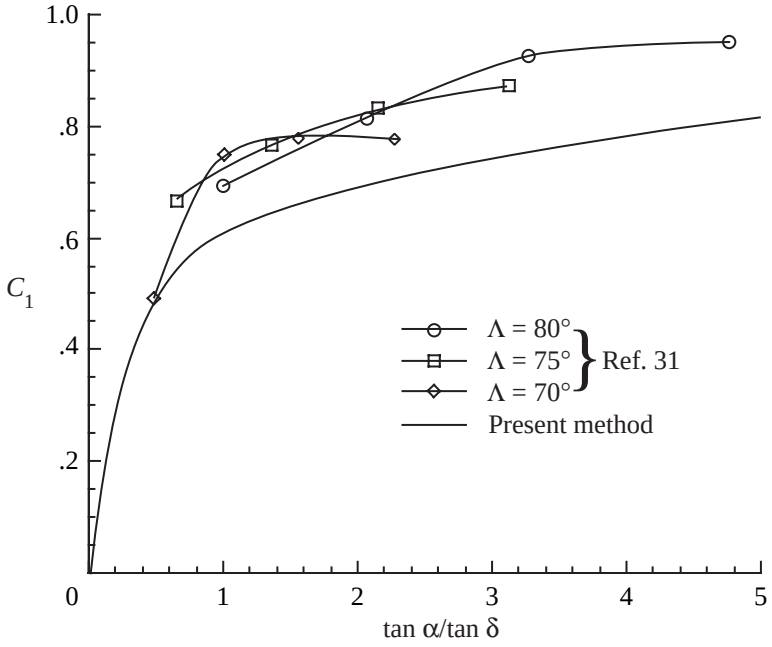

Figure 14. Calculated and experimental variations of nondimensional vortex strength with tan α/tan δ; ϕ = 0°.

As shown in figure 15, the agreement was much better with the data of reference 32, in which circulation was measured using a novel nonintrusive ultrasound technique. The technique of reference 32 involves sending ultrasonic pulses in clockwise and counterclockwise directions around a fixed path perpendicular to the delta-wing root chord and then determining the circulation from the transit-time difference between the two pulses. In figure 15, calculated variations are presented for comparison with the data of reference 32 in the form of plots of the nondimensional ratio $\Gamma_k/U_\infty c$ against angle of attack, for different chordwise stations and two wing sweeps: 60° (figs. 15(a)–(d)) and 70° (figs. 15(e)–(h)). The calculated values in these figures were determined from the calculated curve of C_k versus tan α/tan δ presented in figure 14 by using the relationship

$$\frac{\Gamma_k}{U_\infty c} = 2\pi C_k \frac{l}{c} \tan\delta \sin\alpha \tag{52}$$

The hatched lines in figures 15(a)–(h) denote the approximate angle of attack at which a vortex burst occurred at each chordwise station in the experiments. The data show that at each wing station and for both wings, the computed values are in very good agreement with experimental values up to and sometimes beyond the point of vortex breakdown.

Static Vortex Positions and Strengths for Nonzero Roll Angle

Figure 16 shows that, at angle of attack of 30°, calculated vortex center locations for different wing roll angles were also in good agreement with the experimental data. Figure 16 presents computed center locations along with the wind tunnel results obtained by Jun and Nelson in reference 2, for a wing swept 80° at roll angles up to 45°. Figure 16(a) shows the center locations relative to the axis system fixed relative to the wing; figure 16(b) shows center locations relative to a stationary axis system that rotates with the wing. These results are for a wing that is rolled through a positive angle ϕ, for which the vortex on

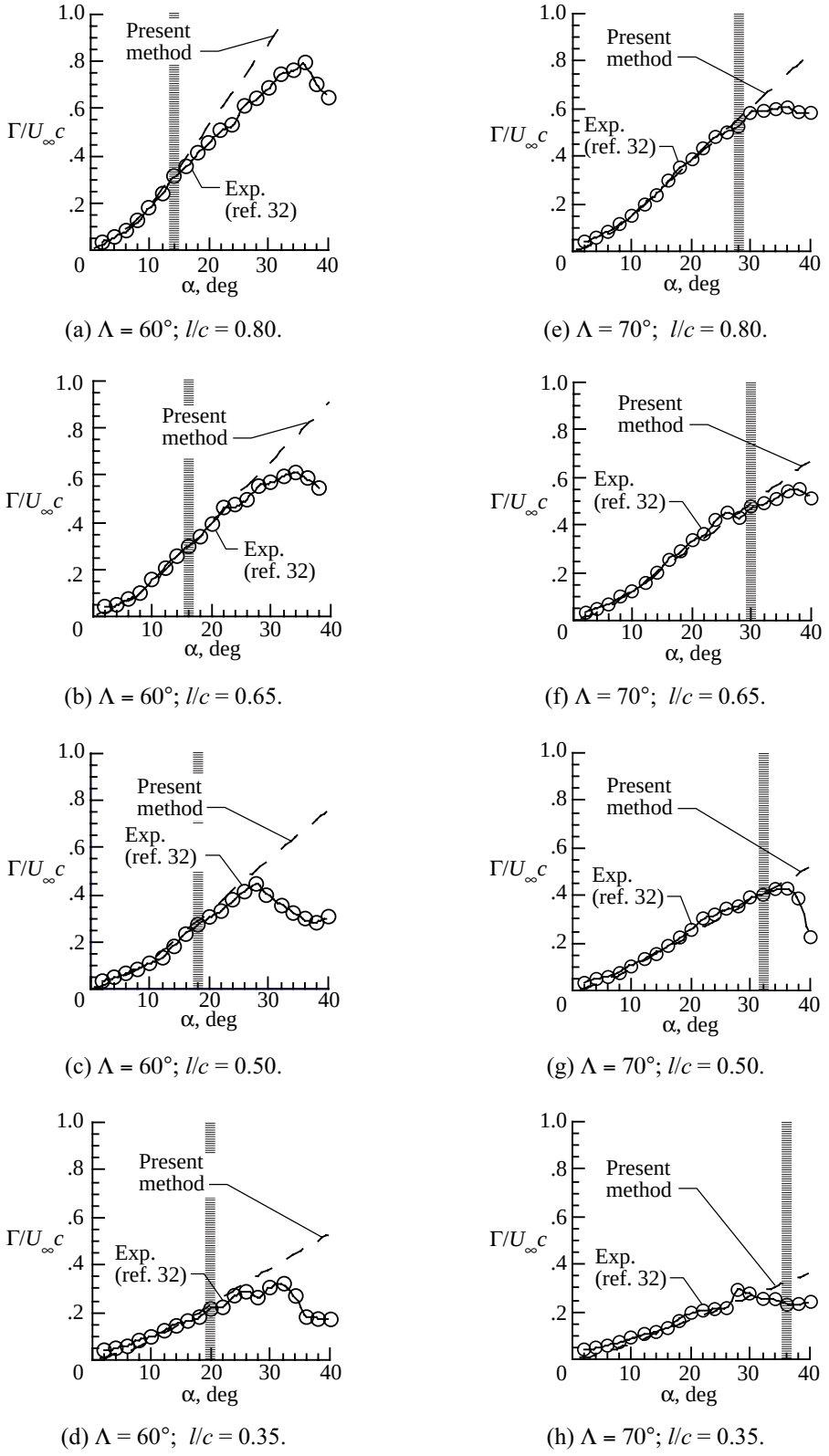

(a) Λ = 60°; l/c = 0.80.

(e) Λ = 70°; l/c = 0.80.

(b) Λ = 60°; l/c = 0.65.

(f) Λ = 70°; l/c = 0.65.

(c) Λ = 60°; l/c = 0.50.

(g) Λ = 70°; l/c = 0.50.

(d) Λ = 60°; l/c = 0.35.

(h) Λ = 70°; l/c = 0.35.

Figure 15. Calculated values of $\Gamma/U_\infty c$ and experimental values obtained by using nonintrusive ultrasound technique in reference 32. Hatched lines at each chordwise station indicate approximate angle of attack for vortex breakdown at that station; ϕ = 0°.

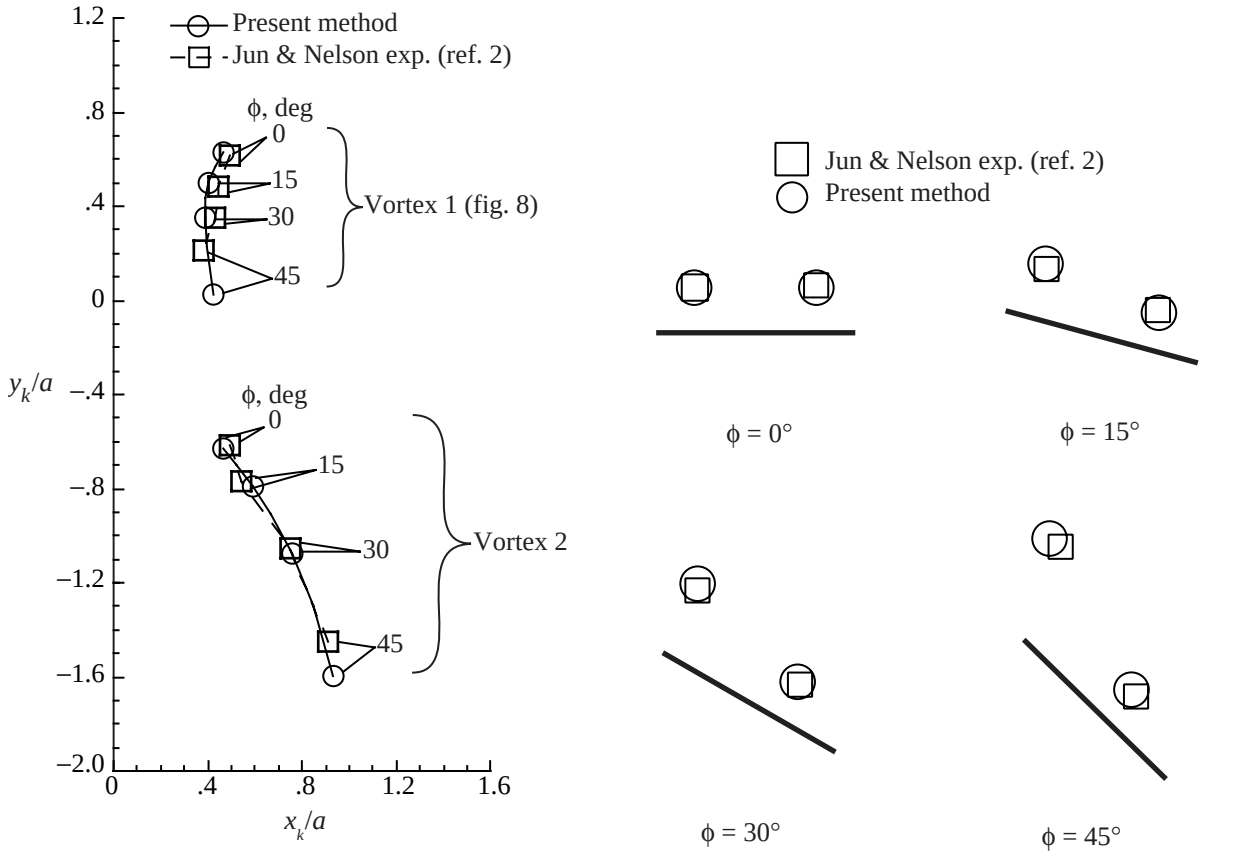

(a) Vortex center locations in wing-fixed axes system.

(b) Wing and vortex center movement relative to fixed axes.

Figure 16. Experimental and calculated vortex center locations for different wing roll angles at $\alpha = 30°$.

the right wing panel is located inboard and close to the wing, while that on the left panel is located farther outboard and away from the wing. Figure 16 shows the agreement to be very good at roll angles of about 30° or below. Above about 30°, the calculated results put the right vortex farther inboard and the left vortex farther outboard than the experimental results indicate.

The agreement is not as good at the higher angles of attack. The effect of angle of attack on the computed positions is shown in figure 17, which shows that the center locations move away from the wing as the angle of attack increases, but the increase in distance from the wing becomes small at the higher values of α. The wind tunnel results, on the other hand, show vortex centers that are farther from the wing at $\alpha = 45°$ than the calculated results indicate they should have been. This difference could possibly be caused by a bending away from the wing due to the influence of the flow aft of the wing. At $\alpha = 40°$, the wind tunnel results show vortex breakdown, indicating that some of this bending has occurred.

The calculated effect of positive roll angle on nondimensional vortex strength is shown in figure 18. Except for the lowest angle of attack, the circulation is higher for vortex 1, the vortex closer to the wing. This vortex tends to maintain about the same circulation throughout the range of ϕ, whereas vortex 2, which moves out and away from the wing at positive roll angles, loses circulation with increasing values of ϕ. This type of variation is consistent with the increase in the static restoring moment on the wing that occurs when ϕ increases and no hysteretic effects are present.

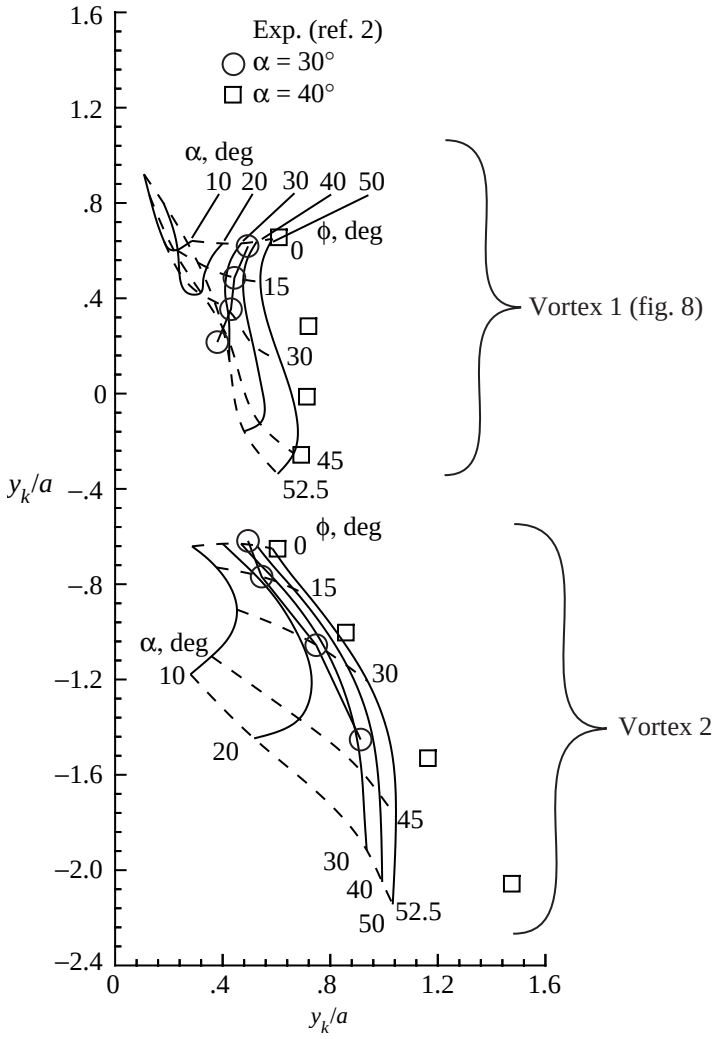

Figure 17. Static vortex center locations for various wing roll angles and angles of attack.

Wing Rock Time Histories

Comparison of Calculated and Experimental Time Histories

The results of the wing rock calculations show that, while in general the present method was able to model the basic wing rock motion for delta wings, the motions were highly dependent on the static rolling moment characteristics of the wing. As will be discussed, when the variation of static C_l versus ϕ obtained by using the leading-edge suction analogy was used, the rates of buildup were more rapid and the maximum oscillation amplitude and frequencies were higher than in the experiment; however, when this variation of static C_l versus ϕ was adjusted to bring it into closer agreement with the wind tunnel variation, the oscillations were brought into close agreement with the experiment.

Figure 19 presents calculated and experimental wing rock oscillations for a delta wing swept 80° at an angle of attack of 30°. The experimental data are those obtained in reference 4 in free-to-roll tests of a wing that was mounted on an air-bearing support system that had essentially zero friction. This wing has a

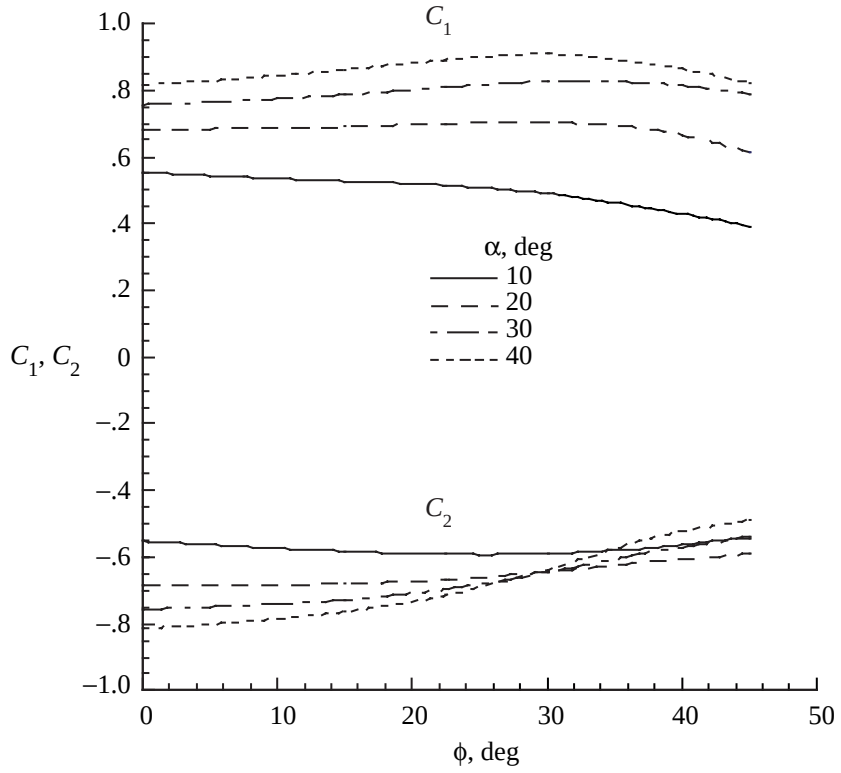

Figure 18. Effect of wing roll angle on nondimensional vortex strength (radial velocity assumed at each primary vortex center).

root-chord length of 1.3976 ft, a span of 0.4921 ft, an area of 0.3439 ft^2, and a roll axis moment of inertia of 6.39×10^{-4} slug-ft^2. Figure 19 shows both the roll angle time histories and the variations of the static rolling moment coefficient with roll angle. The variation of C_l versus ϕ for the experimental data was determined from the roll angle time history as described in reference 4.

Figure 19 shows a close tie-in between the roll angle time histories and the static C_l versus ϕ curves. Both the experimental and the calculated time histories show that frequency generally decreased as amplitude of the oscillation increased; this inverse relationship is a consequence of the fact that the oscillation frequency depends primarily on the slope of the C_l versus ϕ curve, and this slope decreases with increasing roll angle.

The calculated time history (fig. 19(b)) shows a more rapid buildup to a higher maximum amplitude than for the experimental time history (fig. 19(a)) (the calculated time history reaches ϕ_{max} of about 52.2° instead of about 49.4° for the experiment) and has a higher frequency at the maximum amplitude (1.43 Hz compared with about 1.17 Hz for the experiment). These differences could be attributed to the substantial differences in the C_l at a given ϕ between calculation and experiment. When the calculated C_l versus ϕ curve was generated, it was assumed that the static wing rolling moments were those given by equation (40), and that the wing had a flat-plate cross section for which $k = 1.0$. This assumption gave much higher calculated static rolling moments at a given ϕ than those shown for the experiment in figure 19(a). Since the hysteretic moments were assumed to be proportional to the static moments, the hysteretic loops of the calculated rolling moment variations in figure 19(b) were substantially wider that those for the experiment in figure 19(a). The higher rolling moment increments produced by these hysteretic loops

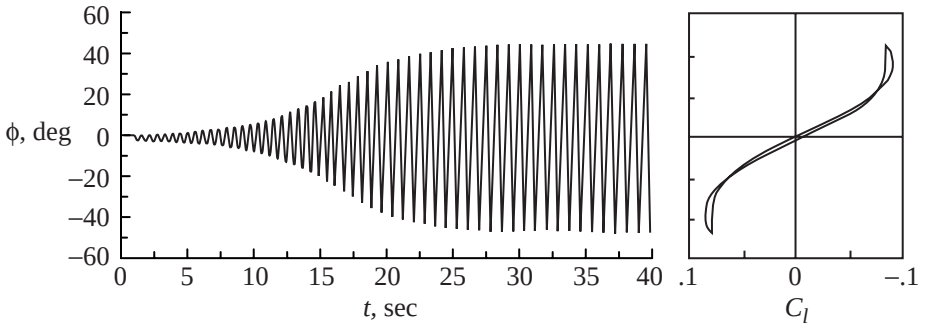

(a) Reference 4 experiment.

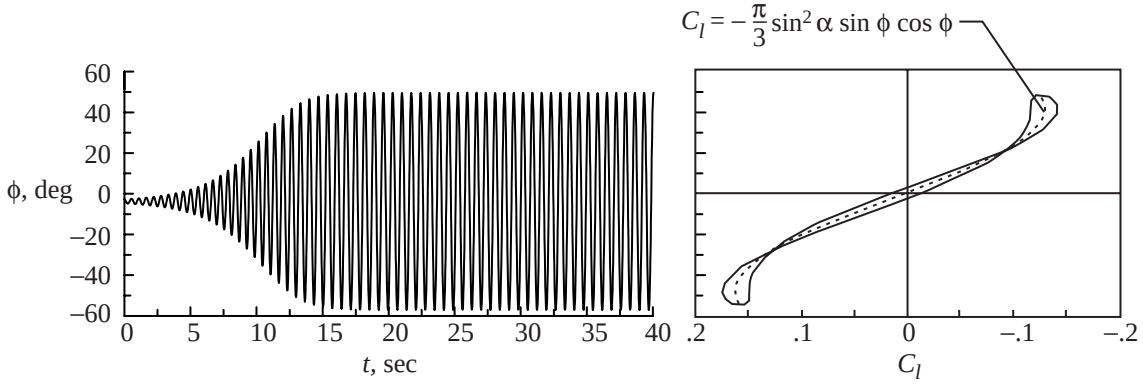

(b) Calculated with assumed static rolling moment reduction factor $k = 1.0$.

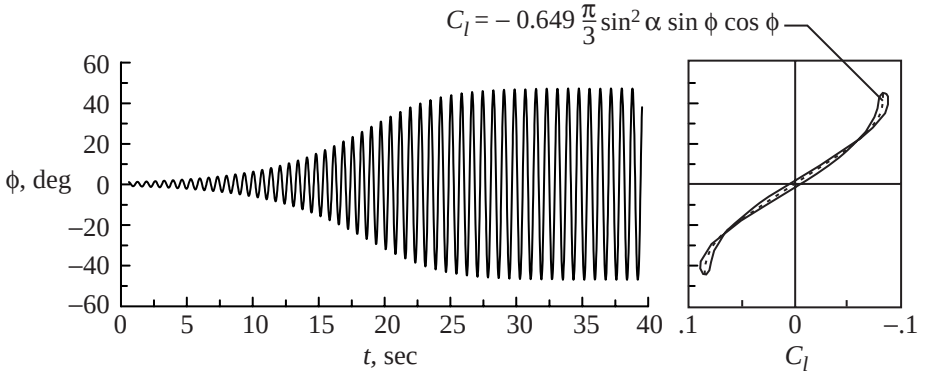

(c) Calculated with assumed static rolling moment reduction factor $k = 0.649$.

Figure 19. Measured and predicted roll angle time histories and C_l variation with ϕ at $\alpha = 30°$, $\phi = 1°$, and $\Lambda = 80°$.

were the reason for the faster rate of buildup and higher maximum amplitude of the calculation compared with the experiment. The higher oscillation frequencies for the calculation compared with the experiment could be attributed to the slopes of the C_l versus ϕ curve being higher than those for the experiment at all roll angles.

Like figure 19(b), figure 19(c) shows a calculated oscillation time history but with an assumed value of $k = 0.649$. Figure 19(c) shows that with this new value of k, the calculated time history is brought into

close agreement with the experimental data of reference 4 (shown in fig. 19(a)): the calculated rate of buildup approximately matches that of the experiment, the calculated maximum oscillation amplitude is about 47.5° versus 49.4° for the experiment, and the calculated frequency at maximum amplitude is about 1.19 Hz versus 1.17 Hz for the experiment. This closer agreement would then indicate that if the static rolling moment characteristics of a wing (or possibly a wing-body configuration) could be determined fairly accurately, the wing rock motions could be approximated fairly accurately.

The lower value of C_l at a given ϕ for the experiment could possibly be due to a wing thickness effect. The calculations assume a thin flat-plate wing; the experimental wing had a thickness of 0.25 in., giving it a thickness-to-span ratio at the wing trailing edge of 4.23 percent. This thickness-to-span ratio increases as the distance from the wing apex to a given wing cross section decreases and theoretically becomes infinite at the apex. The type of beveling at the wing leading edge could also account for differences in calculated versus experimental results. Reference 9 shows significant effects of different types of beveling on wing rock amplitudes. For example, the wing tested in reference 1 had a sharp upper surface with beveling on the bottom surface; according to reference 9 this type of beveling would lower the severity of the wing rock.

Figure 20 provides another set of wing rock time history data for comparison: data from reference 7, for a wing swept 80° at an angle of attack of 25°. The wing tested in reference 7 had a root chord of 1.0827 ft, a span of 0.3806 ft, an area of 0.3054 ft^2, and a roll axis moment of inertia of 1.566×10^{-4} slug-ft^2, and was tested at a free-stream velocity of 49.22 ft/sec. The oscillation shown was initiated at a wing roll angle of 10°. The static rolling moment variation with ϕ for this wing was not provided in reference 7, nor is it known how much friction was present in the mounting apparatus used in the tests. This wing had a thickness-to-span ratio at the trailing edge of 1.72 percent and had its sharp edge at the lower surface with beveling on the upper surface. By setting $k = 0.87$ and by assuming a value for the structural present in the tunnel roll apparatus for the tests, the calculated time history could be brought into close agreement with the experiment for the wing of reference 7. A value of $C_{l_{\text{friction}}} = 0.03$ was assumed, which is about half the value of C_{l_p} for the wing with attached flow.

Comparison of Calculated and Experimental Hysteretic Deflections

When the approximation to the experimental static rolling moments was used, the calculated hysteretic deflections were in good agreement with experimental data of reference 2. Calculated hysteretic deflection envelopes that assume $k = 0.649$ are presented for comparison with experimental results in figure 21, which shows the x versus y position of the vortices during a steady state oscillation at maximum amplitude. Figure 21 shows the calculated envelopes are slightly longer and narrower than the experimental envelopes, but overall the agreement is good. The y (lateral) and x (normal) hysteretic deflections are presented as functions of ϕ in figures 22(a) and 22(b), respectively. In figure 22, the experimental envelopes are not quite symmetrical; nevertheless, overall there is good agreement between calculation and experiment.

Causes of Wing Rock and Its Limited Amplitude

The calculated results of the present method verify that—as has been indicated by the experimental results of references 1 through 4—hysteretic deflections of the leading-edge vortices cause wing rock. The results show that the hysteretic deflections at the higher angles of attack and the lower roll angles produce the unstable rolling moments that drive the wing oscillation to higher amplitude. Moreover, the

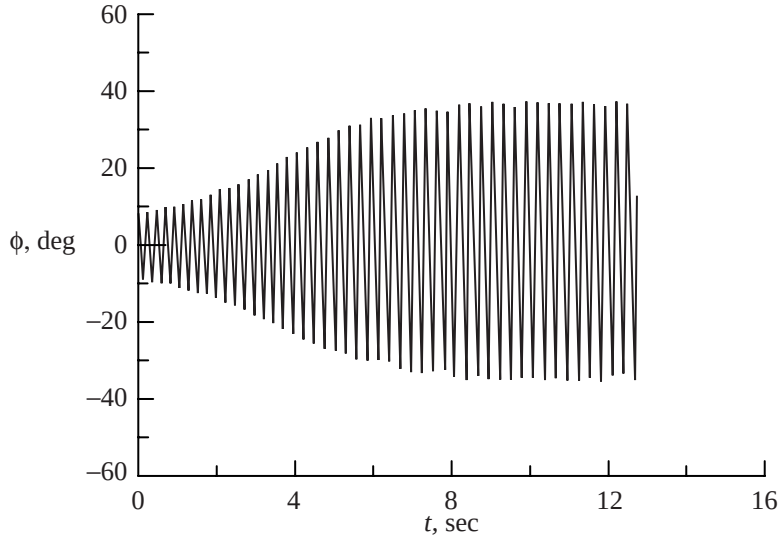

(a) Reference 7 experiment.

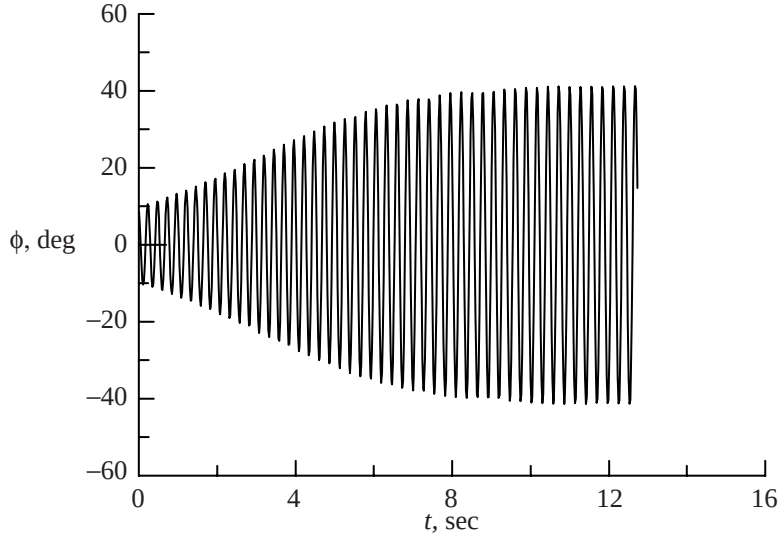

(b) Calculated with assumed $k = 0.87$, $C_{l_{\text{friction}}} = 0.03$.

Figure 20. Calculated amplitude time history and experimental data of reference 7 at $\alpha = 25°$.

calculated results indicate the source of the restoring moments that limit the amplitudes of the oscillation. When the wing is rolled, the asymmetric vortex arrangement consists of one vortex that is located farther outboard and away from the wing than the other vortex, which is inboard and close to the wing. The restoring moments can be attributed to the movement of the outboard vortex to points farther away from the wing and an increase in the strength of the inboard vortex.

The rolling moments caused by wing rolling velocity are shown for angles of attack of 10°, 20°, and 30° in figures 23(a), (b), and (c), respectively. Each figure shows total roll damping as a function of non-dimensional roll rate for wing roll angles of 0°, 15°, 30°, and 45°. The total roll damping shown is the sum of the attached-flow roll damping (equal to the attached-flow roll damping coefficient times the non-dimensional roll rate) and ΔC_{l_h}, the incremental hysteretic damping.

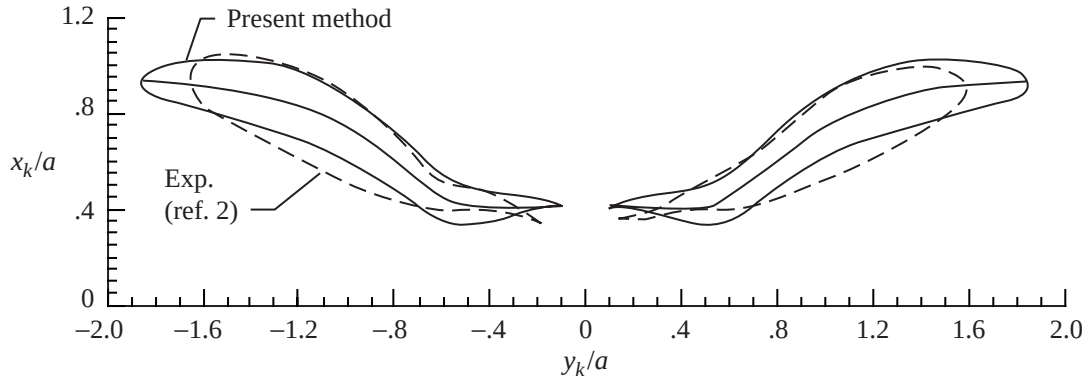

Figure 21. Calculated and experimental normal hysteretic displacement of primary vortices as function of lateral displacement at $\alpha = 30°$.

Figure 23(a) shows that at $\alpha = 10°$, the roll damping curves for each wing roll angle fell along a single straight line; this colinearity was the result of hysteretic vortex deflections at this angle of attack being very small, so that the hysteretic roll damping moments were essentially zero. The slope of these curves was approximately equal to C_{l_p}—the roll damping coefficient for the wing with attached flow—with a negative slope (negative C_{l_p}) indicating stable damping (that is, a positive roll rate would produce a negative moment that opposes the wing motion). Because the roll damping at $\alpha = 10°$ was stable, wing rock did not occur at this angle of attack.

At $\alpha = 20°$ (fig. 23(b)), hysteretic vortex deflections were larger, and these larger deflections decreased the stability to very low levels at $\phi = 0°$ and 15°; however, the damping moments remained either neutrally or slightly stable so that, although the wing was on the verge of wing rock at this angle of attack, wing rock still did not occur.

At $\alpha = 30°$ (fig. 23(c)), the rolling moments show a high degree of instability at roll angles of 0° and 15°. Wing rock did occur at this angle of attack.

At all three angles of attack, the roll damping moment variation was stable at a roll angle of 30°, where it was approximately equal to the attached-flow roll damping coefficient; at $\alpha = 20°$ and 30°, it became more stable when the roll angle was increased to 45°. The sketches in figures 23(b) and (c) show that at least part of this stable damping at the higher roll angles could be related to the movement of the vortex on the upward-deflected wing panel to points outboard and farther away from the wingtip. At values of ϕ less than 30° both vortices lie inboard of the wingtip, but at $\phi = 30°$ the vortex on the upward-deflected panel is located slightly outboard of the wingtip and continues to move farther outboard and away from the tip as the roll angle increases. Much of the stable damping could be attributed to this vortex moving outboard of the wingtip to where it had much less of an effect on the wing.

At the same time, the calculated circulations, such as those presented in figure 24, show that the inboard vortex in these sketches would have a higher circulation (C_2 in fig. 24 would be more negative) when the wing roll angle is positive and increasing. Although the inboard vortex is farther from the wing than it would be in its static position, it produces a positive rolling moment that acts to restore the roll angle to zero. These two effects combined—the lessening effect of the outboard vortex and the higher circulation of the inboard vortex—produce the positive restoring moments that limit the amplitudes of wing rock oscillations.

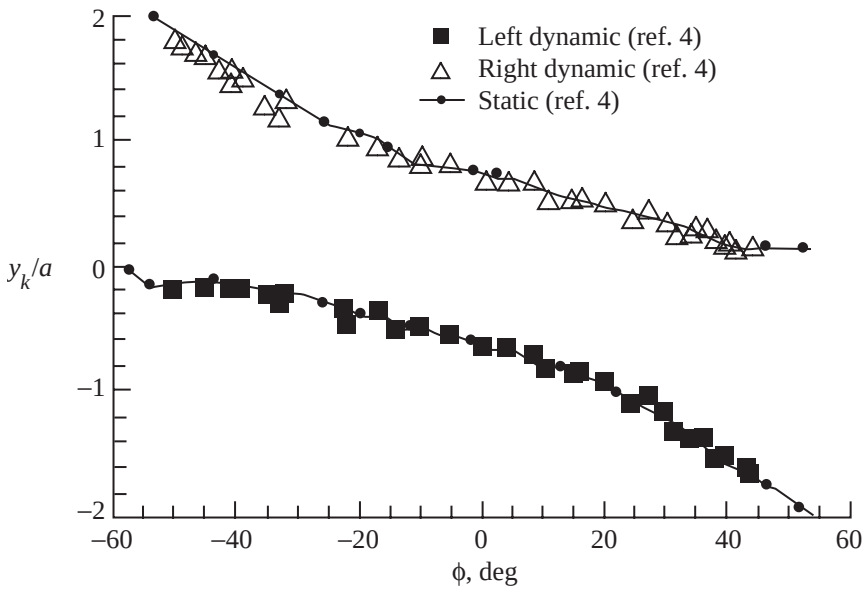

(a) Spanwise position.

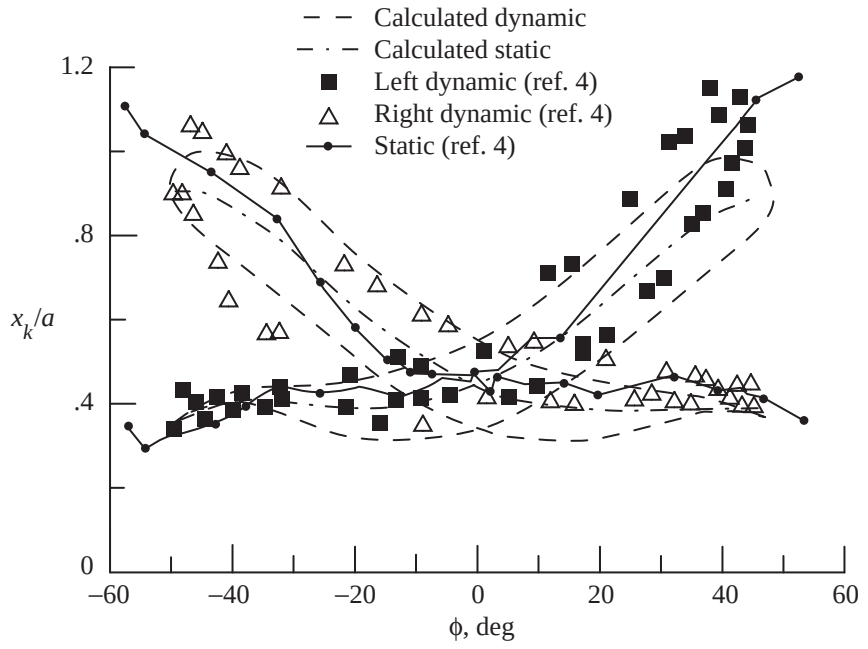

(b) Normal position.

Figure 22. Calculated and experimental vortex center positions during wing rock oscillation as function of wing roll angle at $\alpha = 30°$.

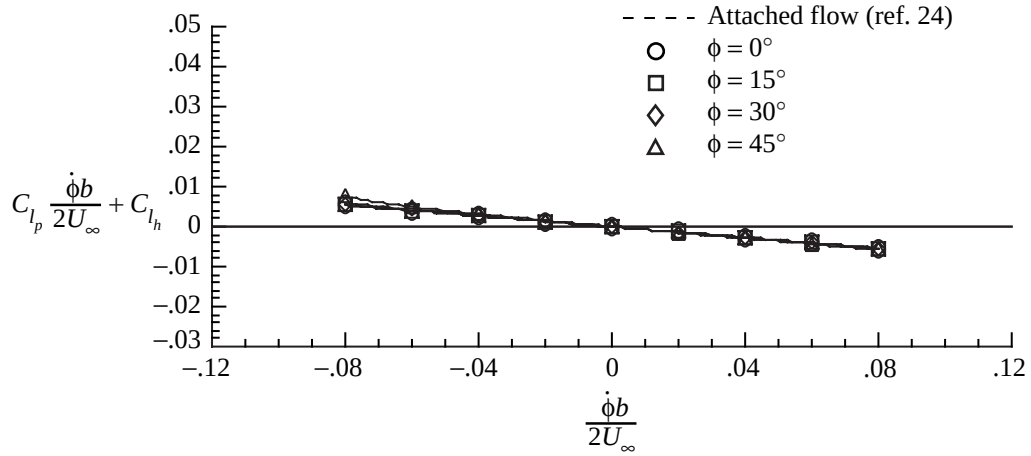

(a) α = 10°.

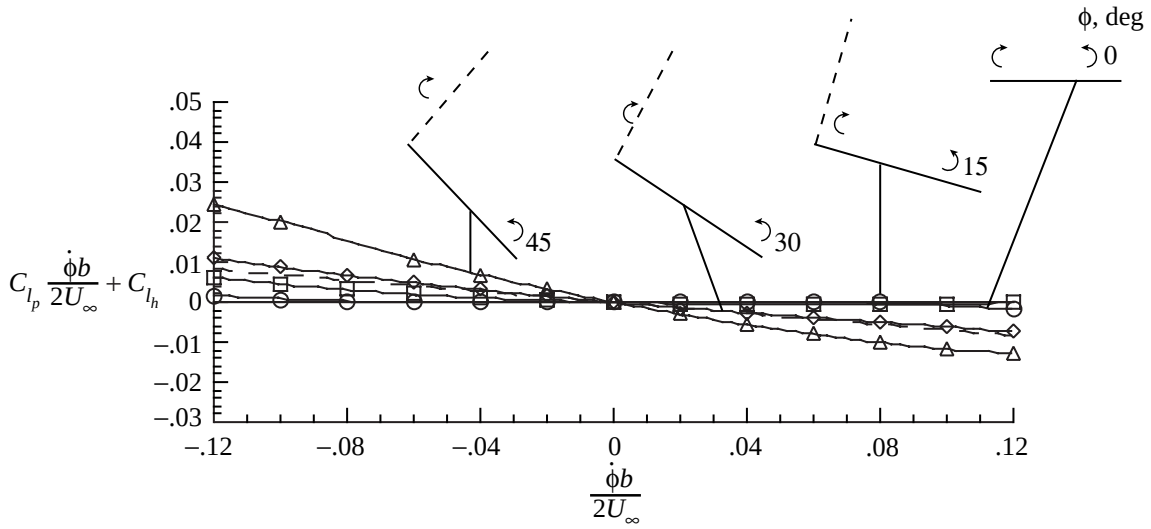

(b) α = 20°.

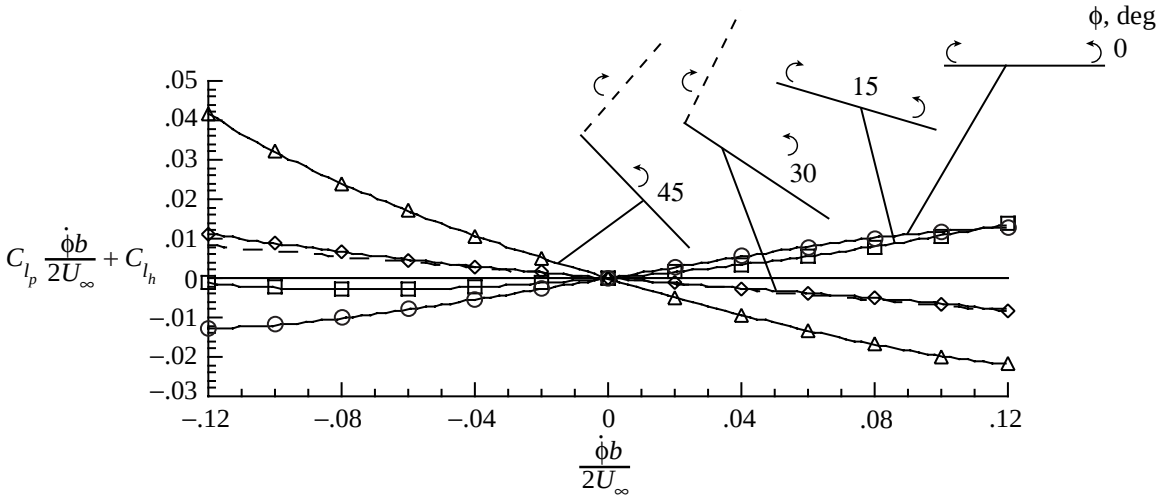

(c) α = 30°.

Figure 23. Total roll damping as function of nondimensional wing roll rate.

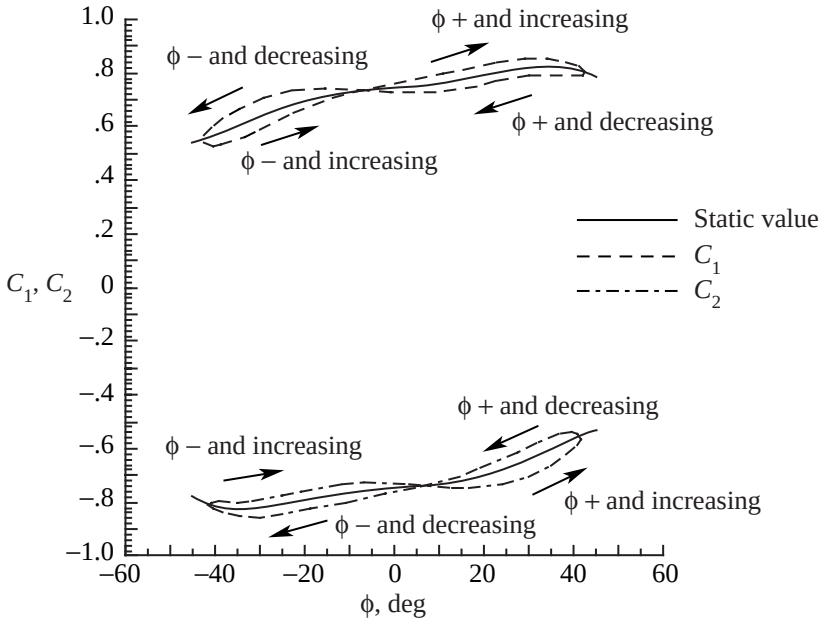

Figure 24. Variation of nondimensional vortex strengths of primary vortices with wing roll angle for wing rock oscillation at $\alpha = 30°$.

Effect of System Parameters on Oscillation Amplitude and Frequency

The calculated results showed that for wings with a given sweep and cross section shape, the wing rock oscillations could be defined in terms of two parameters that were functions of wing angle of attack only. These parameters were the maximum amplitude of the oscillation ϕ_{max} and the reduced frequency $f\sqrt{I_l/qSb}$. These parameters were affected by changes in wing sweep and changes in k, the wing cross section shape parameter (see eq. (40)); also, in wind tunnel tests they were affected by the amount of friction in the mounting apparatus. But for wings with the same sweep, cross section, and test conditions, the variation with angle of attack would be the same, regardless of the free-stream velocity, the wing size, or the wing moment of inertia.

Calculated variations of ϕ_{max} with α are presented for comparison with experimental variations for a delta wing with 80° and 75° sweep in figures 25(a) and (b), respectively. Figure 25(a) shows wing rock oscillations for experimental data that represent wings with different thickness and different types of leading-edge beveling. The experimental data of reference 9 show wing rock starting at an angle of attack of about 17°, compared with about 22° for the experimental data of reference 4. An abrupt drop-off in ϕ_{max} at about $\alpha = 30°$ can be seen in the data of reference 4, which, according to reference 1, is due to vortex breakdown. Two calculated variations are also shown: one for the wing of reference 4, for which it was assumed that $k = 0.649$ and that no structural damping was present, and the other for the wing of reference 7, for which it was assumed that $k = 0.87$ and that there was structural damping in the amount $C_{l_{friction}} = 0.03$ present in the tunnel roll apparatus. Overall, the calculated results agree with the experimental data. The calculated results with $k = 0.649$ generally fall between the experimental data of references 4 and 9, which had similar types of leading-edge beveling; the calculated results with $k = 0.87$ and $C_{l_{friction}} = 0.03$ for the wing of reference 7 are in good agreement with the experimental data of reference 7.

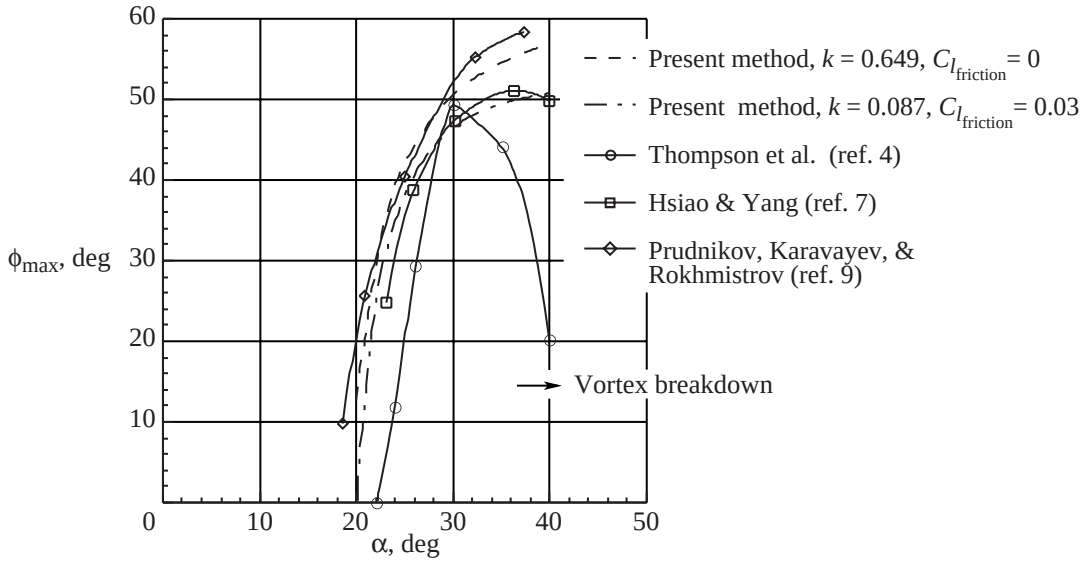

(a) Λ = 80°.

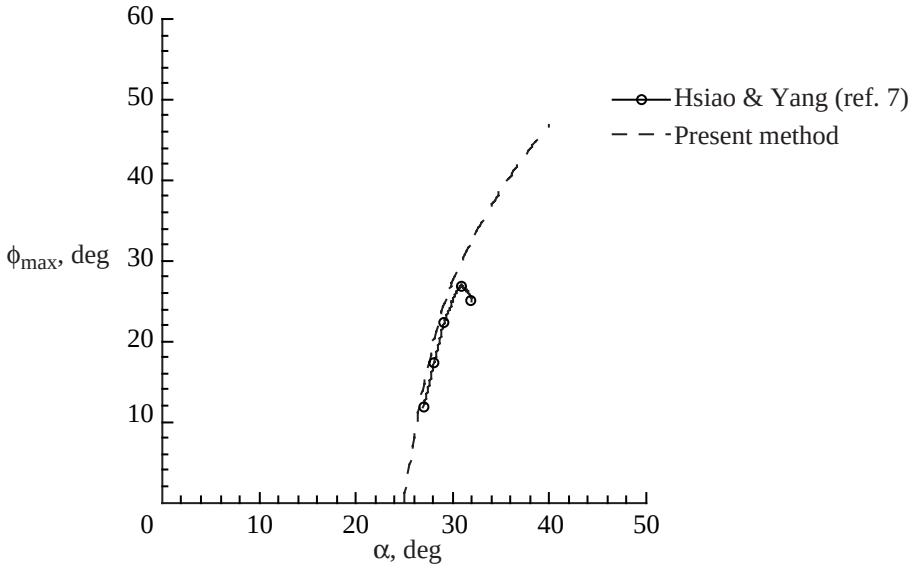

(b) Λ = 75°.

Figure 25. Calculated and experimental variations in maximum amplitude of wing rock oscillations with angle of attack.

By comparing both calculated and experimental data from figure 25(a) ($\Lambda = 80°$) with that of figure 25(b) ($\Lambda = 75°$), one can see that reducing the wing sweep reduced the maximum amplitude of a wing rock oscillation at a given angle of attack. This reduction in ϕ_{max} is the result of the fact that, although wings with different sweeps have the same static C_l at a given angle of attack and roll angle (since they were computed by using eq. (40)), the wing with the lower sweep has a lower value of tan α/tan δ at a given angle of attack. With a lower value of tan α/tan δ, the vortex circulations and hysteretic displacements are lower at a given roll angle; hence, the driving moments are smaller and the wing rock oscillation does not reach as high a maximum amplitude.

The effects of angle of attack on wing rock reduced frequencies are shown in figures 26 and 27, where the calculated results from the present method are presented along with experimental results from reference 7. The data from reference 7 are the only set available for demonstrating the effects of free-stream velocity, wing sweep, and wing inertia on wing rock characteristics. In reference 7 reduced frequency is presented in the form fb/U_∞, which makes it independent of free-stream velocity.

Figure 26 presents calculated and measured values of fb/U_∞ for two wing sweeps and different wing moments of inertia. Calculated values of fb/U_∞ increased with angle of attack for both wing sweeps. For the wing swept 80°, the experimental values of the reduced frequency remained approximately constant with angle of attack below $\alpha = 40°$ for the low wing inertias. At angles of attack above 40°, the experimental values tended to increase and come into closer agreement with the calculated values as the wing inertia increased. For the wing swept 75°, the experimental values of reduced frequency increased with α and were in good agreement with the calculated values for both wing inertias shown.

As shown in figure 27, the calculated curves for different wing inertias from figure 26 could be reduced to just two curves—for wing sweeps of 80° and 75°—by expressing reduced frequency in the form $f\sqrt{I_l/qSb}$. The reason for this is that, for a spring-and-mass system such as that defined by the equation of motion for the wing rock model (eq. (47)), the oscillation frequency is primarily determined by the spring-constant term, that is

$$f \approx \sqrt{\frac{C_{l_\phi} qSb}{I_l}} \tag{53}$$

Since, for wings with the same cross section shape, the C_l versus ϕ variation depends only on angle of attack (see eq. (40)), the reduced frequency $f\sqrt{I_l/qSb}$ should depend only on angle of attack and be independent of wing size and inertia and free-stream dynamic pressure.

The experimental values of $f\sqrt{I_l/qSb}$ plotted in figure 27 show that the data for the two lower inertias for the wing swept 80° did not collapse into a single curve, and the values were lower than the calculated values; however, as with the velocity-reduced frequency fb/U_∞ (shown in fig. 26), the data did tend to collapse and the reduced frequencies came into closer agreement with the present calculations as the inertia was increased. For the higher wing inertias for the wing swept 80°, and for all inertias for the wing swept 75°, the calculated reduced frequencies of the form $f\sqrt{I_l/qSb}$ were in generally good agreement with the experimental values.

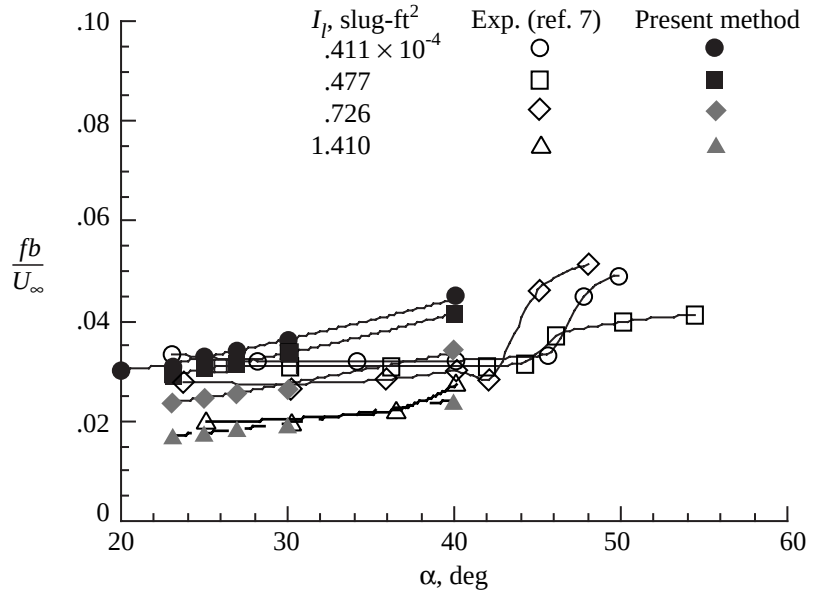

(a) Λ = 80°.

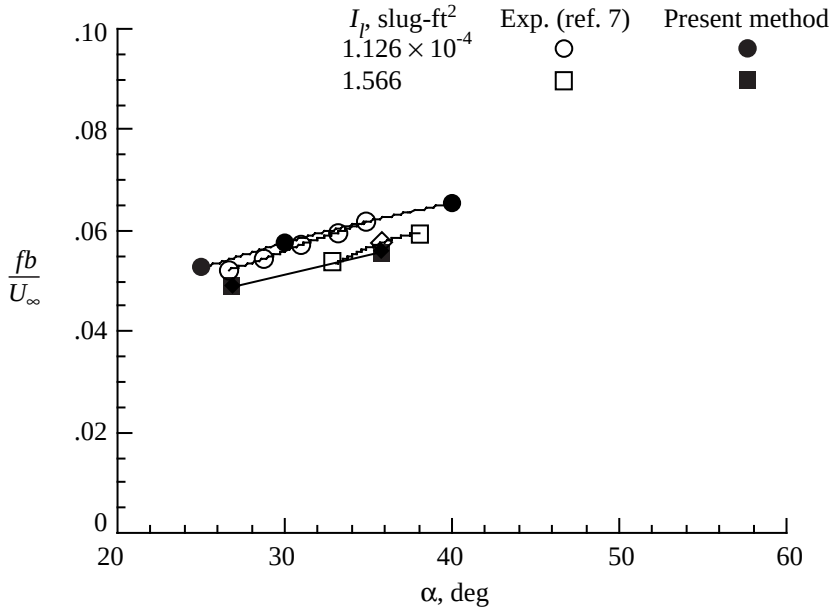

(b) Λ = 75°.

Figure 26. Calculated and experimental variations with angle of attack of reduced frequency fb/U_∞.

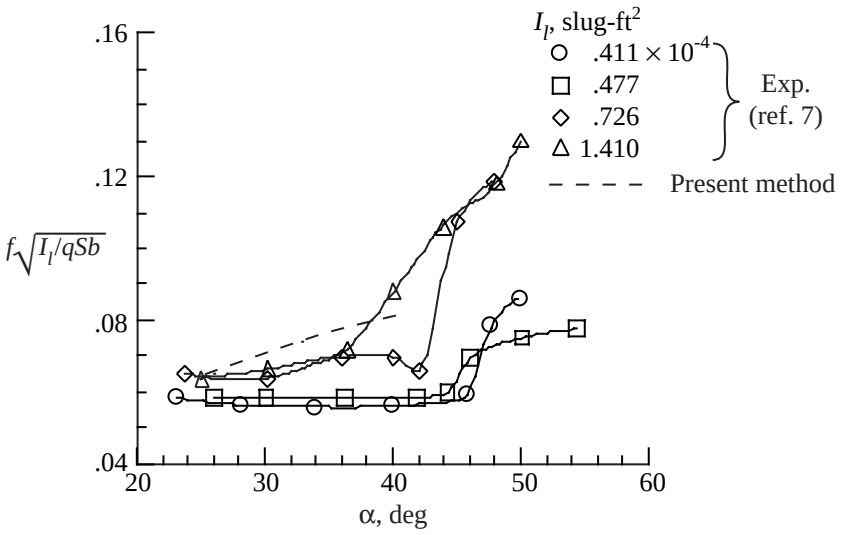

(a) Λ = 80°.

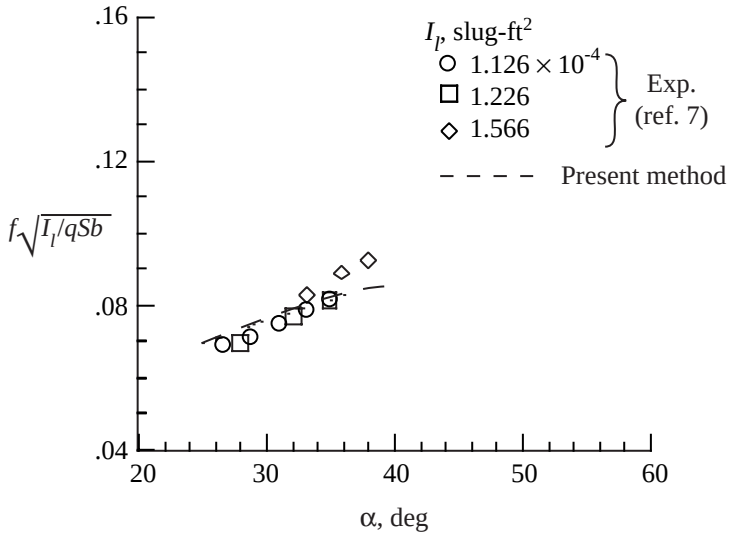

(b) Λ = 75°.

Figure 27. Calculated and experimental variations with angle of attack of reduced frequency $f\sqrt{I_l/qSb}$.

Conclusions

A discrete-vortex method has been developed to model the vortex flow over a delta wing and investigate the wing rock problem associated with these wings. The results indicate the following conclusions:

1. Static vortex positions at zero roll angle were in good agreement with experimental results. The present method gave much better agreement with experimental data than either the Brown and Michael or Legendre methods, which placed the vortex centers much farther outboard than the present method.

2. For angles of attack below those for which vortex breakdown occurred, calculated vortex circulations were in excellent agreement with those measured by Johari and Moreira in "Direct Measurement of Delta-Wing Vortex Circulation" (*AIAA Journal*, December 1998, pp. 2195–2203) using a nonintrusive ultrasound technique.

3. Static vortex center locations at nonzero roll angles were also in good agreement with experimental data. At angles of attack α of 35° and 45°, the wind tunnel results showed vortex centers that were farther from the wing than those of the calculated results. This difference may have been caused by the bending away from the wing due to the influence of the flow aft of the wing. At both $\alpha = 35°$ and 40°, the wind tunnel results showed vortex breakdown, indicating some of this bending had occurred.

4. The present method was able to model the basic features of wing rock. The rates of buildup of the oscillations were generally more rapid and the maximum oscillation amplitude and frequencies were higher than the experiment when the variation of the static rolling moment C_l versus roll angle ϕ obtained from the leading-edge suction analogy was used. The oscillations were brought into very close agreement, however, when an approximation to the variation of the static C_l versus ϕ obtained from the wind tunnel results was used.

5. When the approximate variation of static C_l versus ϕ obtained from wind tunnel results was used in the calculations, the calculated hysteretic deflections were overall in good agreement with the experiment, indicating that a strictly kinematic relationship—derived by using the time analogy and conical-flow assumptions—could be used to calculate these deflections.

6. The present method was able to verify the cause of wing rock and indicated the reason for the limited amplitude. At roll angles of about 30°, a lag in vortex position produced a destabilizing rolling moment increment; above about 30°, it produced a stabilizing increment. This shift from destabilizing to stabilizing rolling moments was the result of one vortex moving outboard of the wingtip and decreasing in strength at wing roll angles above about 30°.

7. The calculated results showed that for wings with a given sweep and cross section shape, the maximum amplitude and the reduced frequency $f\sqrt{I_l/qSb}$ would be functions of wing angle of attack only. Calculated variations with angle of attack of the maximum amplitude of the wing rock oscillations generally agreed with the experimental data. Both the experimental and calculated results showed that reducing the wing sweep reduced the maximum amplitude of the wing rock oscillation for a given angle of attack.

8. For wings swept 80°, experimental values of $f\sqrt{I_l/qSb}$ were generally lower than the calculated values for the lower wing inertias, but came into closer agreement with the calculations as the inertia was increased. For the higher wing inertias, calculated and experimental reduced frequencies were in good agreement for wings swept both 80° and 75°.

Appendix A

Transformations for Complex Planes Used in Present Analysis

The transformations equations presented in this appendix allow transformation back and forth between any of the three complex planes, shown in figure A1, that were used in developing the present method.

In the ζ-plane (fig. A1(a)), the flow at zero roll angle is parallel to the flat plate representing a delta wing cross section. This plane is used in the Brown and Michael analysis of reference 16, wherein it serves as the primary complex modeling plane in which the problem was set up before transforming to the physical plane. It could not be used in this capacity in developing the present method, however, because it did not give the correct velocities at the vortex centers in the physical plane, as required by the radial-velocity boundary conditions of the present model. To determine the velocity at a given vortex center, the effects of that vortex on itself must be neglected. But in the ζ-plane one vortex also serves as the image of the other, so that two singularities have to be dealt with at a given center. Setting the velocities at both singularities to zero gives incorrect values for velocity at the vortex center in the physical plane.

In the present method the ζ-plane is used primarily to define the vortex locations when the wing is at a nonzero roll angle. In this plane, lines of constant velocity potential at a zero roll angle correspond to ξ = Constant lines and so are easily defined. The procedure used to iterate on ξ in order to determine vortex positions for nonzero roll angles is described in the section "Application of Nonzero Roll Boundary Conditions."

The σ-plane (fig. A1(b)) is the basic modeling plane used to generate flow fields in the ζ- and λ-planes. In this plane, the vortex flow is represented by pairs of simple logarithmic vortices (see eq. (2)) for which the momentum is known. The images placed inside the cylinder ensure tangent flow at the surface of the body in all three planes. Since the images are separate from the primary vortices, the velocities calculated at the primary vortex centers (using eq. (4)) will have the correct values, so that the radial-flow velocity condition can be applied.

The λ-plane (fig. A1(c)) is the physical plane in which the actual flow about the wing cross section is represented, and is the one in which all boundary conditions must be satisfied.

Points in one of these complex planes can be transformed into points in any of the others by using one of the following transformations:

$$\left.\begin{aligned} \zeta &= \sqrt{\lambda^2+1} & \lambda &= \sqrt{\zeta^2-1} \\ \zeta &= \sigma + \frac{a^2}{4\sigma} & \sigma &= \frac{\zeta \pm \sqrt{\zeta^2-a^2}}{2} \\ \lambda &= \sigma - \frac{a^2}{4\sigma} & \sigma &= \frac{\lambda \pm \sqrt{\lambda^2+a^2}}{2} \end{aligned}\right\} \tag{A1}$$

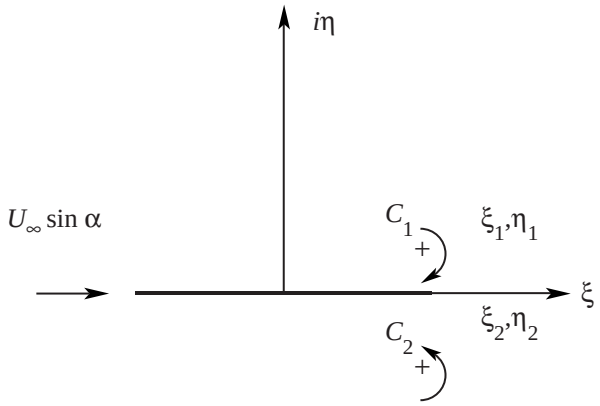

(a) ζ-plane.

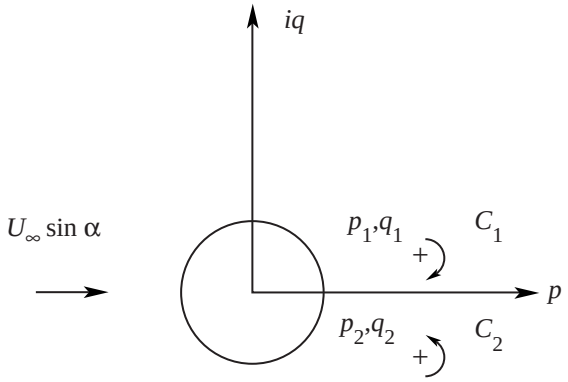

(b) σ-plane.

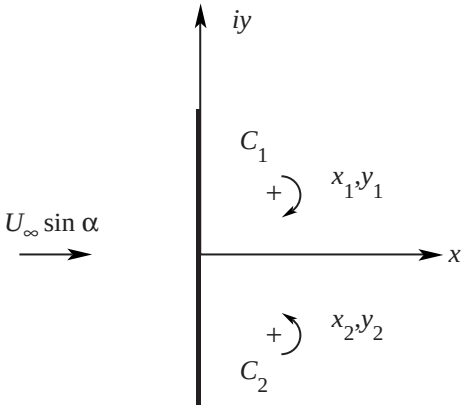

(c) λ-plane.

Figure A1. Complex planes used in present analysis.

In nondimensional form, these become

$$\left.\begin{array}{ll} \dfrac{\zeta}{a}=\sqrt{\dfrac{\lambda^2}{a^2}+1} & \dfrac{\lambda}{a}=\sqrt{\dfrac{\zeta^2}{a^2}-1} \\ \dfrac{\zeta}{a}=\dfrac{1}{2}\left(\dfrac{\sigma}{r_o}+\dfrac{1}{\sigma/r_o}\right) & \dfrac{\sigma}{r_o}=\dfrac{\zeta}{a}\pm\sqrt{\dfrac{\zeta^2}{a^2}-1} \\ \dfrac{\lambda}{a}=\dfrac{1}{2}\left(\dfrac{\sigma}{r_o}-\dfrac{1}{\sigma/r_o}\right) & \dfrac{\sigma}{r_o}=\dfrac{\lambda}{a}\pm\sqrt{\dfrac{\lambda^2}{a^2}+1} \end{array}\right\} \qquad \text{(A2)}$$

Appendix B

Description of Forces Acting on Delta Wing

The description of delta wing forces in this appendix is intended to clear up some of the confusion existing in the literature about the nature of these forces, particularly about the force on the feeding sheet considered in previous discrete-vortex models such as those of references 13, 14, 16, and 17.

According to the present model, three forces act on the delta wing: one steady and two unsteady. These forces can be computed by performing Blasius integrations (see refs. 19 and 20) around a closed path that encloses only the wing in the physical λ-plane. Steady forces are computed using the formula:

$$F_X - iF_Y = i\frac{\rho}{2}\oint_{C_o}\left(\frac{dW}{d\lambda}\right)^2 d\lambda \tag{B1}$$

Unsteady forces are computed by using the time-dependent formula:

$$F_{X_{\text{unsteady}}} - iF_{Y_{\text{unsteady}}} = -i\rho\frac{\partial}{\partial t}\oint_{C_o}\overline{W}d\overline{\lambda} \tag{B2}$$

In these equations, W is the complex potential for the flow (see eq. (2)), and can be written in terms of coordinates in the λ-plane as

$$W\left(a,\Gamma,\frac{\lambda_k}{a}\right) = aU_\infty \sin\alpha\left(\sqrt{\frac{\lambda^2}{a^2}+1}\cos\phi + i\frac{\lambda}{a}\sin\phi\right) + i\frac{\Gamma_k}{2\pi}\left[\ln\left(\sqrt{\frac{\lambda^2}{a^2}+1}-\sqrt{\frac{\lambda_k^2}{a^2}+1}\right)-\ln\left(\sqrt{\frac{\lambda^2}{a^2}+1}-\sqrt{\frac{\overline{\lambda}_k^2}{a^2}+1}\right)\right] \tag{B3}$$

The unsteady forces arise from the fact that this complex potential is a function of time because the wing semispan a and the vortex circulation Γ_k vary with time. That is, both quantities vary with distance along the three-dimensional delta wing and, therefore, according to the time analogy, vary with time in an equivalent two-dimensional time-dependent plane. The vortex center coordinate λ_k also varies with distance or time, but appears in the complex potential only in its nondimensional form λ_k/a, which is independent of time. That is, for a given wing at a given angle of attack and roll angle, λ_k/a is the same for each primary vortex at each wing cross section and is therefore independent of both distance along the wing and of time.

The three forces that can be obtained using the steady and unsteady Blasius formulas are discussed in the following sections.

Static Pressure Force

The static pressure force is obtained by considering all quantities in equation (B3) to be constant and independent of time, and therefore it is considered a steady force that can be determined by using equation (B1). In deriving this force, the primary vortices are assumed to have fixed positions and to have

fixed circulations; this force then represents the static pressure force that the vortex system exerts on the wing as a result of its inducing high velocities and therefore high pressures on the wing. This force can be written in coefficient form as

$$C_X - iC_Y = \frac{i}{2}\oint_{C_o}\left(\frac{1}{U_\infty \sin\alpha}\frac{dW}{d\lambda}\right)^2 d\left(\frac{\lambda}{a}\right)\sin^2\alpha \tag{B4}$$

The opposite of this force is the force that the wing exerts on the vortex system, and it is this static pressure force on the vortex system that causes the primary vortices to change their positions and hence their momentum, as expressed by the boundary conditions S-2 and AS-6.

Attached-Flow Force

The attached-flow force is obtained by holding Γ_k and λ_k constant when taking the time derivative in equation (B3) while allowing the local wing semispan a to vary with time. This is the basic force that the wing would develop if the flow were attached and there were no vortex formation. Although the attached-flow force is usually considered to be a steady force, there would be no such force in potential flow if the wing cross section were not expanding. In the context of the present model, it is the force that results strictly from the fact that the wing cross section expands with distance along the delta wing or with time in an equivalent two-dimensional flow.

The integral involved in obtaining the attached-flow force can be written in terms of the wing semi-apex angle and angle of attack using the time analogy. The derivative with respect to time in equation (B2) can be written as

$$\frac{\partial}{\partial t} = \frac{d}{da}\frac{da}{dl}\frac{dl}{dt} = \frac{a}{l}U_\infty \cos\alpha \frac{d}{da} = \tan\delta\, U_\infty \cos\alpha \frac{d}{da} \tag{B5}$$

With the time derivative written this way, the attached-flow force, in coefficient form, becomes

$$C_{F_{\text{attached}}} = 2i\oint_{C_o}\left(\overline{\sqrt{\frac{\lambda^2}{a^2}+1}\cos\phi + i\frac{\lambda}{a}\sin\phi}\right) d\left(\frac{\overline{\lambda}}{a}\right)\frac{\tan\delta}{\tan\alpha}\sin^2\alpha \tag{B6}$$

where the integration is to be carried out around any path enclosing the wing.

It can be shown that the lift coefficient computed for the wing by using equation (B6) is

$$C_{L_{\text{attached}}} = \frac{C_{F_{\text{attached}}}}{\cos\alpha} = \frac{\pi A}{2}\sin\alpha \tag{B7}$$

which, when the small-angle approximation for $\sin\alpha$ is made, becomes the formula derived by Jones for slender delta wings in reference 33.

Force Caused by Changes in Vortex Circulation

This force is obtained by holding the wing semispan a constant and allowing Γ to vary in equation (B2). It is the force that arises from the increases in Γ that take place as the primary vortices grow

with time in the two-dimensional time-dependent plane, or with distance along the three-dimensional delta wing. This force is the same as that on the straight-line feeding sheet that serves as a branch cut in the Brown and Michael (ref. 16) and similar models. That is, these previous models assume a force on the branch cut of

$$F_{FS} = -i\rho \frac{d\Gamma_k}{dt}\left(\lambda_k - \lambda_s\right) \tag{B8}$$

This force then is equal to the unsteady pressure $\rho\,\partial\Gamma/dt$ times the length of the branch cut.

It should be noted, however, that the branch cut for which this force is calculated cannot be taken arbitrarily; more specifically, it cannot be taken to lie between the primary vortex and a separation point at the wingtip as assumed in the Brown and Michael model. The logarithmic functions in equation (B3) have branch points z_o and at the image point r_o^2/σ_o, thus the branch cut needed to make them single-valued should lie between these two points. In the σ-plane, this cut is along the straight radial line between the primary vortex and its image; in the λ-plane, it becomes a curved line extending from the wing to the vortex center, as shown in figure 2(b). To calculate the force using equation (B3), the integration must be carried out around a cut that connects the vortex and image branch points. An integration carried out around a path enclosing only the feeding sheet of the Brown and Michael model will give zero force, rather than the force given by equation (B8).

Although the force given by equation (B8) is to be interpreted mathematically as a pressure acting over a certain length in the flow, it can be given no such physical interpretation in the real flow. It is strictly the unsteady pressure force that results from changes in the strength of the vortex system. There is no physically visible feeding sheet in the real flow along which unsteady pressures act.

As discussed in the main text in the section "Discussion of the Symmetric Boundary Conditions: *X*-Axis Momentum Condition," this force is neglected in considering the force-momentum balance on the vortex system because the unsteady force caused by changes in vortex circulation strength is exactly equal to the rate of change of momentum caused by changes in vortex circulation, regardless of the location of the vortex center. No new information is obtained by equating this unsteady force to the rate of change of momentum caused by changes in circulation; therefore, this force does not play a roll in determining vortex position and strength.

Total Delta Wing Force

Because secondary and tertiary vortices are not included in the present model, adding the steady and unsteady forces described previously will not give the correct value for the total force on the wing. The total normal force for a delta wing, however, can be closely approximated by using the Polhamus leading-edge-suction analogy (ref. 23), which gives a normal force coefficient due to the vortices (for the general case with the wing at a nonzero roll angle) of

$$C_N = \pi \sin^2\alpha \cos^2\phi \tag{B9}$$

Appendix C

Derivation of Equation for Vortex Hysteretic Deflections Caused by Wing Rolling Motion

The vortices in the wake of a delta wing do not respond instantaneously to wing motion and therefore are subject to hysteretic deflections as the wing rotates about its longitudinal axis. The available experimental data show very little, if any, hysteretic deflection in the lateral direction (the data of ref. 4, for example, show y-positions of the vortices to be approximately the same as the static positions at any time during a rolling oscillation). The deflections in the x-direction (normal to the wing), however, can be substantial. The model in the present method makes use of the two-dimensional time analogy and also assumes that the primary vortices deflect in a conical manner as the wing rotates, as shown in figure C1. In figure C1, the line of vortex centers is assumed to deflect as a straight line, with the deflection Δx at any station being proportional to the distance from the wing apex, as required if the flow is to remain conical.

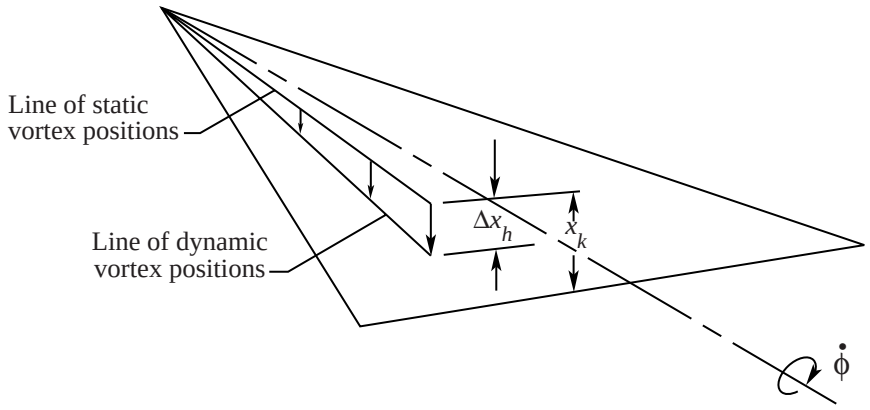

Figure C1. Hysteretic deflection of vortex.

According to the two-dimensional time analogy, the flow over a delta wing is analogous to that for a two-dimensional plate whose span and the flow around it are changing with time. In the two-dimensional flow field, the vortices are increasing in strength and moving radially outward from the center line of the plate with time. If the plate is rotating, each vortex will also be moving either toward it or away from it at a velocity of $y_k\dot{\phi}$ and will deflect toward or away from the plate through a distance of

$$\Delta x_k = \int_0^t y_k \dot{\phi}\, dt \tag{C1}$$

Multiplying and dividing the right-hand side of equation (C1) by $aU_\infty \sin\alpha$ gives

$$\Delta x_k = \frac{y_k}{a}\frac{\dot{\phi}}{U_\infty \sin\alpha} U_\infty \sin\alpha \int_0^t a\, dt \tag{C2}$$

If the flow is conical, the ratio y_k/a in equation (C2) will be a constant, since the vortex positions are changing in proportion to changes in the semispan; the variable a by itself, of course, will vary linearly

with time. According to the time analogy, time is related to chordwise distance along the three-dimensional wing by

$$dt = \frac{dl}{U_\infty \cos\alpha} \tag{C3}$$

For the delta wing, local semispan is related to chordwise distance by

$$a = l \tan\delta \tag{C4}$$

Making these substitutions into equation (C2) and carrying out the integration over the length of the root chord of the three-dimensional wing gives the hysteretic deflection at the wing trailing edge:

$$(\Delta x_k)_{te} = \frac{y_k}{a} \frac{\dot{\phi}}{U_\infty \sin\alpha} \tan\alpha \int_0^L l \tan\delta \, dl = \frac{y_k}{a} \frac{\dot{\phi}}{U_\infty \sin\alpha} \tan\alpha \frac{L^2}{2} \tan\delta \tag{C5}$$

For the delta wing, $L = b/2 \tan\delta$, so that equation (C1) can be written as

$$(\Delta x_k)_{te} = \frac{y_k}{a} \left(\frac{\dot{\phi} b}{2U_\infty \sin\alpha} \right) \left(\frac{\tan\alpha}{2\tan\delta} \right) \frac{b}{2} \tag{C6}$$

The deflection at the base, nondimensionalized in terms of the wing semispan at the base, then becomes

$$\frac{(\Delta x_k)_{te}}{b/2} = \frac{y_k}{a} \left(\frac{\dot{\phi} b}{2U_\infty \sin\alpha} \right) \left(\frac{\tan\alpha}{2\tan\delta} \right) \tag{C7}$$

Because the flow is assumed to be conical, both the hysteretic deflection Δx and the wing semispan a vary linearly with chordwise distance l. With this type of variation, the ratio of hysteretic deflection to wing semispan will be constant along the wing, so that at any cross section this ratio is equal to the ratio at the trailing edge. Equation (C7), therefore, gives the nondimensional hysteretic deflection at any cross section as

$$\frac{\Delta x_k}{a} = \frac{(\Delta x_k)_{te}}{b/2} = \frac{y_k}{a} \left(\frac{\dot{\phi} b}{2U_\infty \sin\alpha} \right) \left(\frac{\tan\alpha}{2\tan\delta} \right) \tag{C8}$$

Equation (C8) shows the hysteretic deflection to be equal to the product of (1) the nondimensional lateral coordinate of the vortex center, (2) the nondimensional rolling velocity of the wing, and (3) a nondimensional time, which is constant for the wing and can be expressed in terms of the quantity $\tan\alpha/\tan\delta$.

Appendix D

Wing Rolling Moment Calculations

As stated in the main text, calculating the wing rolling moments was a problem in developing the present method because of the simplifying assumptions made. The model neglects the secondary and tertiary vortices and does not apply a Kutta condition at the wing leading edges; therefore, the velocities and pressures at the leading edges are infinite. Under these conditions, Blasius integrations around the wing do not give the correct moments, presenting a problem in calculating both the static wing rolling moments and the rolling moments produced on the wing by hysteretic deflections of the primary vortices. For the static rolling moments, this problem was solved by assuming that these moments could be closely approximated as being those for the wing with attached flow. For the hysteretic moments, it was resolved by integrating around the primary vortices instead of the wing to obtain the moments, and then reducing these by a constant factor to obtain the wing moments. The equations for the static and hysteretic moments are discussed in the following sections.

Calculation of Static Wing Rolling Moments

These static moments were determined by integrating around the wing cross section with an assumed attached flow. This integration was done by using the Blasius formula for moments (see ref. 19 or 20), which in coefficient form can be written as

$$C_l = -\frac{1}{6}\ \mathrm{Re}\left[\oint_{C_o}\left(\frac{\lambda}{a}\right)\left(\frac{1}{U_\infty \sin\ \alpha}\frac{dW}{d\lambda}\right)^2 d\left(\frac{\lambda}{a}\right)\right]\sin^2\alpha \tag{D1}$$

The complex potential $W(\lambda)$ used in this equation was that for the free-stream flow about the wing with no vortex flow (that is, eq. (2) with C_1 and C_2 set to zero). The integration was carried out around a path that enclosed the complete wing cross section.

The moment coefficients obtained from equation (D1) can be written in closed form for a wing at roll and/or sideslip as follows:

For a rolled wing with zero sideslip,

$$C_l = -\frac{\pi}{3}\sin^2\alpha \sin\phi\cos\phi \tag{D2}$$

For a sideslipped wing with zero roll,

$$C_l = -\frac{\pi}{3}\sin\alpha \sin\beta\cos\beta \tag{D3}$$

For a wing that is both rolled and sideslipped,

$$C_l = -\frac{\pi}{3}\left[\sin\alpha(\cos^2\phi - \sin^2\phi)\sin\beta\cos\beta + (\sin\alpha^2\cos^2\beta - \sin^2\beta)\sin\phi\cos\ \phi\right] \tag{D4}$$

Values of rolling moment coefficients calculated by using these relationships are presented with experimental results in figures D1 through D3. Figures D1 and D2 show the variations with angle of attack for different roll and sideslip angles, respectively; figure D3 shows the variations with sideslip and roll angle at angles of attack of 10° and 20°. These figures show that the analytical values are in generally good agreement with experimental data for angles of attack below the stall.

Calculation of Hysteretic Rolling Moments

Because the attached-flow rolling moments used to approximate the static wing rolling moments in equations (D2)–(D4) were functions of wing angle of attack, roll angle, and sideslip angle alone—and not vortex position—they could not be used to determine the hysteretic rolling moments when the wing was oscillating. These hysteretic moments had to be determined by Blasius integrations made with the primary vortices included in the flow field.

With vortices included, it was found that the rolling moments calculated by Blasius integrations around only the wing would not limit the amplitude of the wing rock oscillations. This failure to limit the amplitude was believed to be the result of the infinite pressures acting at the wing leading edges in the present model. These infinite pressures give a distorted pressure distribution on the wing so that moments cannot be computed accurately.

To work around this problem, the rolling moments used in the calculations were those obtained by integrating around only the primary vortices. The moments obtained this way are the result of finite forces that act at the centers of the primary vortices to produce a moment about the wing moment center. It was believed, therefore, that incremental changes in the magnitudes and positions of these forces caused by hysteresis would produce incremental moments that were an accurate indication of those affecting the wing.

As indicated previously, the incremental moments due to hysteresis were obtained by using the Blasius equation (D1), and for $W(\lambda)$, using the full complex potential for the flow with vortices (eq. (2) of the text with C_1 and C_2 not equal to zero). The integrations were carried out around a path that included only the two primary vortices. To determine the hysteretic moments, two Blasius integrations were made: one with the primary vortices in their static positions x_k,y_k at a given wing roll angle; the second with them in their displaced positions $x_k + \Delta x_k,y_k$ at a given roll angle and roll rate. The incremental moment due to hysteresis was then the difference between these two values:

$$C_{l_h} = C_l\Big|_{x_k+\Delta x_k,\,y_k} - C_l\Big|_{x_k,\,y_k} \tag{D5}$$

As shown in figure D4, the rolling moments obtained by integrating around the primary vortices were substantially more negative than those obtained by integrating around the wing only and, therefore, had to be reduced to obtain the moment increment that would actually be felt by the wing. This reduction was accomplished by multiplying the computed moment increment by reduction factor γ, which was obtained from plots of wing-integration moment versus vortex-integration moment such as that shown in figure D5. The plot shown is for a wing swept 80° ($\delta = 10°$) at an angle of attack of 30° ($\tan\alpha/\tan\delta = 3.27$).

Figure D5 shows that the wing-integration moments vary approximately linearly with the vortex-integration moments at the lower roll angles; this linear relationship breaks down only for absolute values of ϕ greater than about 30°. The slope of the linear fit to the data between roll angles of –30° and +30° was therefore taken to be the value of γ that the vortex-integration moments were multiplied by to get the hysteretic wing rolling moments.

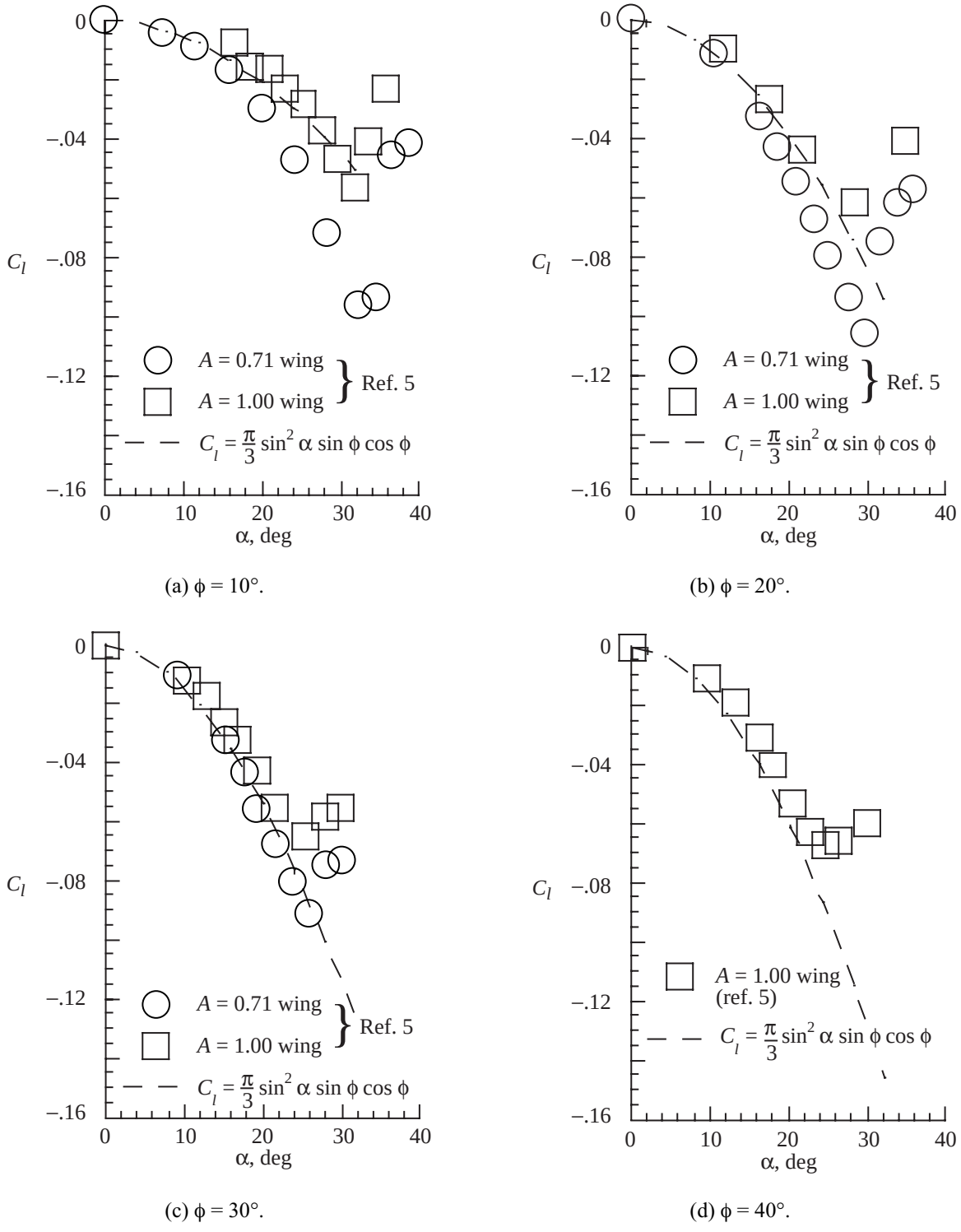

(a) $\phi = 10°$.

(b) $\phi = 20°$.

(c) $\phi = 30°$.

(d) $\phi = 40°$.

Figure D1. Variation of wing rolling moment coefficient with angle of attack for various wing roll angles.

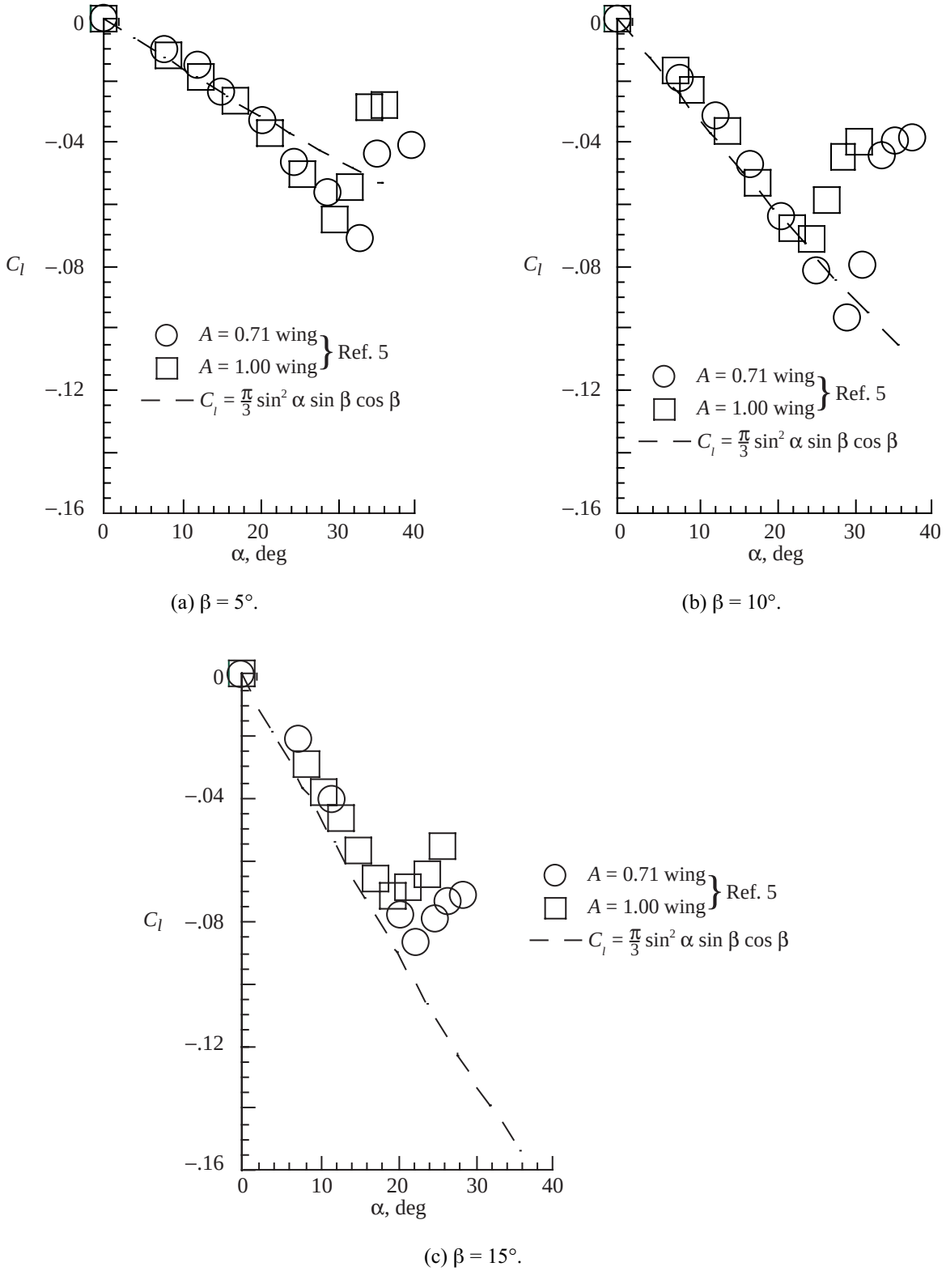

(a) β = 5°.

(b) β = 10°.

(c) β = 15°.

Figure D2. Variation of wing rolling moment coefficient with angle of attack for various wing sideslip angles.

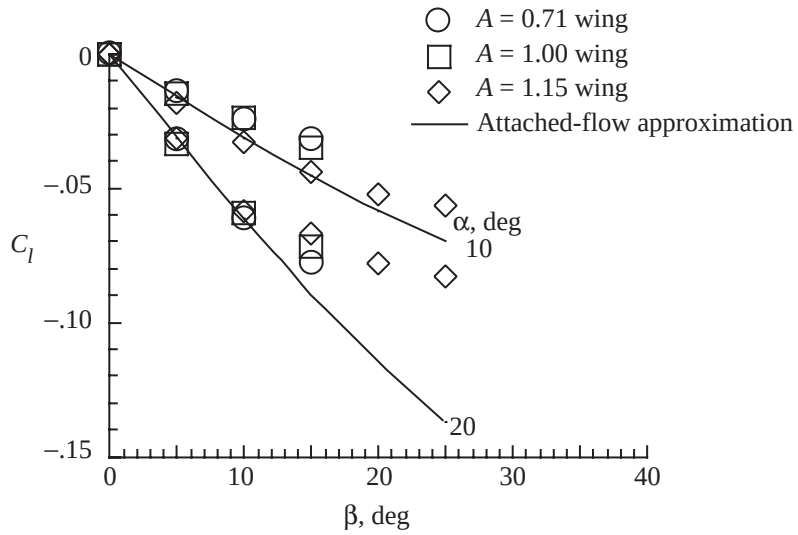

(a) C_l versus β.

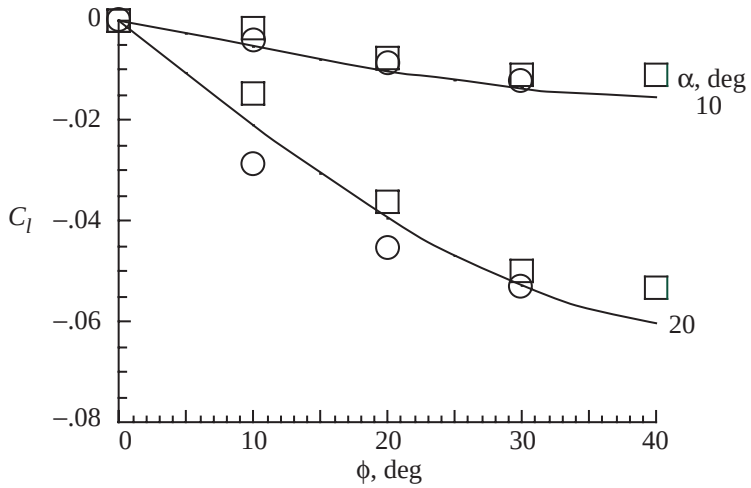

(b) C_l versus ϕ.

Figure D3. Variation of wing rolling moment coefficient with sideslip and with roll angle for angles of attack below the stall.

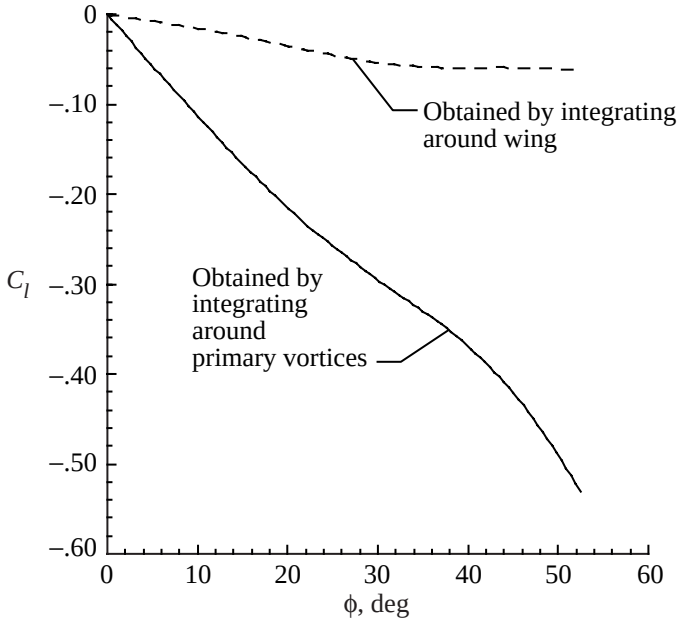

Figure D4. Variation of rolling moment coefficient with wing roll angle obtained by integrating around wing and around primary vortices at $\alpha = 30°$.

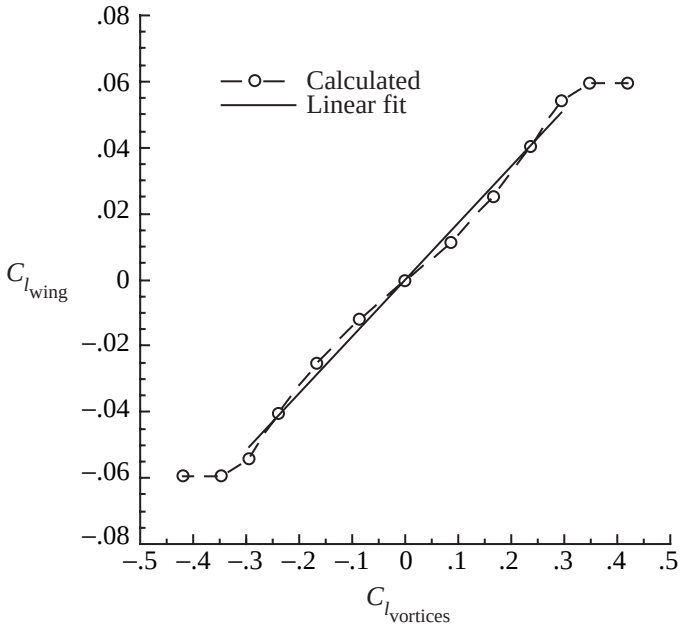

Figure D5. Rolling moment coefficient obtained by integrating around wing versus that obtained by integrating around primary vortices at $\alpha = 30°$.

Values of γ were determined over a range of tan α/tan δ, as shown in figure D6. A cubic fit to these data (eq. (41)) was used to specify the reduction factor for a given wing at a given angle of attack in the wing rock calculations.

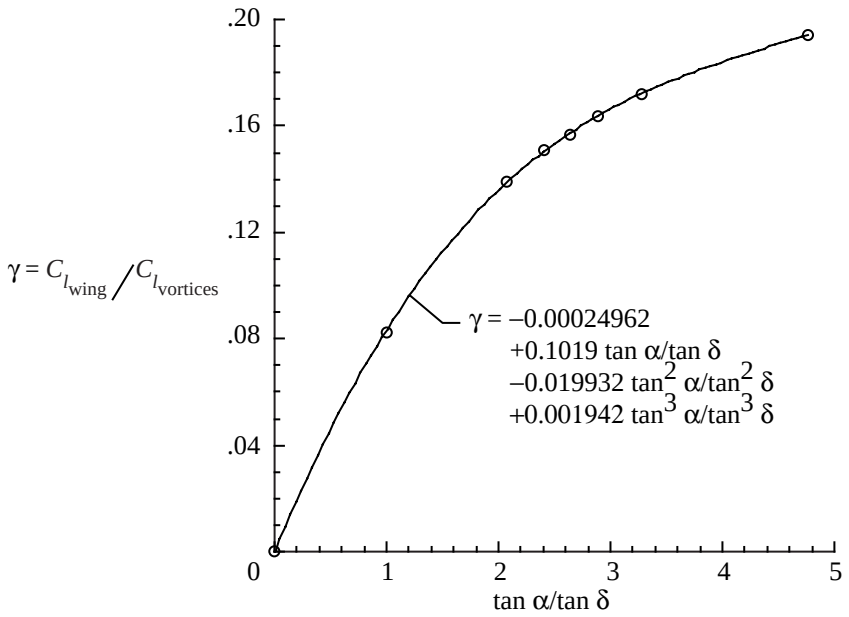

Figure D6. Variation of rolling moment reduction factor γ with tan α/tan δ.

References

1. Arena, Andrew S.; and Nelson, Robert C.: Unsteady Surface Pressure Measurements on a Slender Delta Wing Undergoing Limit Cycle Wing Rock. AIAA-91-0434, Jan. 1991.

2. Jun, Y. W.; and Nelson, R. C.: Leading Edge Vortex Dynamics on a Delta Wing Undergoing a Wing Rock Motion. AIAA-87-0332, Jan. 1987.

3. Arena, Andrew S., Jr.; and Nelson, Robert C.: Experimental Investigations on Limit Cycle Wing Rock of Slender Wings. *J. Aircr.*, vol. 31, no. 5, Sept.–Oct. 1994, pp. 1148–1155.

4. Thompson, S. A.; Arena, A. S., Jr.; Nelson, R. C.; and Batill, S. M.: Dynamic Surface Pressure Measurements on a Delta Wing Constrained to a Pitching or Rolling Motion. *High-Angle-of-Attack Technology*, Vol. 1, NASA CP-3149, Pt. 3, 1990, pp. 1003–1023.

5. Levin, D.; and Katz, J.: Dynamic Load Measurements With Delta Wings Undergoing Self-Induced Roll Oscillations. *J. Aircr*., vol. 21, no. 1, Jan. 1984, pp. 30–36.

6. Nguyen, L. T.; Yip, L.; and Chambers, J. R.: Self-Induced Wing Rock of Slender Delta Wings. AIAA-81-1883, Aug. 1981.

7. Hsiao, Fei-Bin; and Yang, Jiue-Sheng: The Study of Wing-Rock Characteristics on Slender Delta Wings at High AOA. ICASE-96-3.1.1, 1996.

8. Goman, M.; Khrabrov, A.; and Studnev, A.: Stochastic Self-Induced Roll Oscillations of Slender Delta Wing at High Angles of Attack. AIAA-92-4498, Aug. 1992.

9. Prudnikov, Y. A.; Karavayev, E. A.; and Rokhmistrov, O. V.: Wing Rock of Lifting Systems. ICASE-92-4.7.1, 1992.

10. Chaderjian, Neal M.: Navier-Stokes Prediction of Large-Amplitude Delta-Wing Roll Oscillations Characterizing Wing Rock. AIAA-92-4428, Aug. 1992.

11. Lee, E. M.; and Batina, J. T.: Conical Euler Methodology for Unsteady Vortical Flows About Rolling Delta Wings. AIAA-91-0730, Jan. 1991.

12. Kandil, Osama A.; and Salman, Ahmed A.: Three-Dimensional Simulation of Slender Delta Wing Rock and Divergence. AIAA-92-0280, Jan. 1992.

13. Arena, Andrew S.; and Nelson, Robert C.: A Discrete Vortex Model for Prediction Wing Rock of Slender Wings. AIAA-92-4497, Aug. 1992.

14. Hong, John: *An Aerodynamic Model for One and Two Degree of Freedom Wing Rock of Slender Delta Wings*. NASA CR-193130, 1993.

15. Arena, A. S., Jr.: An Experimental and Computational Investigation of Slender Wings Undergoing Wing Rock. Ph.D Thesis, Univ. Notre Dame, April 1992.

16. Brown, Clinton E.; and Michael, William H., Jr.: *On Slender Delta Wings With Leading-Edge Separation.* NACA TN 3430, 1955.

17. Bryson, A. E.: Symmetric Vortex Separation on Circular Cylinders and Cones. *J. Appl. Mech*., vol. 26, no. 4, Dec. 1959, pp. 643–648.

18. Gainer, Thomas G.: *Discrete-Vortex Model for the Symmetric-Vortex Flow on Cones*. NASA TP-2989, 1990.

19. Milne-Thomson, L. M.: *Theoretical Hydrodynamics*. Dover Publ., 1996.

20. Karamcheti, Krishnamurty: *Principles of Ideal-Fluid Aerodynamics*. John Wiley & Sons, 1966.

21. Allen, H. Julian; and Perkins, Edward W.: *Characteristics of Flow Over Inclined Bodies of Revolution*. NACA RM A50L07, 1951.

22. Gainer, Thomas G.: Analysis of Flow on Cones and Cylinders Using Discrete Vortex Methods. AIAA-91-0288, Jan. 1991.

23. Polhamus, Edward C.: *Concept of the Vortex Lift of Sharp-Edge Delta Wings Based on a Leading-Edge-Suction Analogy*. NASA TN D-3767, 1966.

24. Ribner, Herbert S.: *The Stability Derivatives of Low-Aspect-Ratio Triangular Wings at Subsonic and Supersonic Speeds*. NACA TN 1423, 1947.

25. Fink, P. T.; and Taylor, J.: Some Early Experiments on Vortex Separation. R.&M. No. 3489, British ARC, 1967.

26. Kjelgaard, Scott O.; and Sellers, William L., III: Detailed Flowfield Measurements Over a 75° Swept Delta Wing for Code Validation. Paper presented at the AGARD Symposium on Validation of Computational Fluid Dynamics (Lisbon, Portugal), May 2–5, 1988.

27. Bergesen, Andrew J.; and Porter, James D.: An Investigation of the Flow Around Slender Delta Wings With Leading Edge Separation. Rep. No. 510, Princeton Univ., May 1960.

28. Carcaillet, R.; Manie, F.; Pagan, D.; and Solignac, J. L.: Leading Edge Vortex Flow Over a 75-Degree-Swept Delta Wing—Experimental and Computational Results. ICASE-86-1.5.1, 1986.

29. Krist, Sherrie L.; Washburn, Anthony E.; and Visser, Kenneth D.: A Computational and Experimental Investigation of a Delta Wing With Vertical Tails. AIAA-93-3009, July 1993.

30. Legendre, R.: Ecoulment au Voisinage de la pointe avant d'une aile a forte fleche aux incidences moyennes. *La Recherche Aeronautique (ONERA)*, no. 30, Dec. 1952, pp. 3–8.

31. Visser, K. D.: Measurements of Circulation and Vorticity in the Leading-Edge Vortex of a Delta Wing. *AIAA J.*, vol. 31, no. 1, Jan. 1993, pp. 104–111.

32. Johari, H.; and Moreira, J.: Direct Measurement of Delta-Wing Vortex Circulation. *AIAA J.*, vol. 36, no. 12, Dec. 1998, pp. 2195–2203.

33. Jones, Robert T.: *Properties of Low-Aspect-Ratio Pointed Wings at Speeds Below and Above the Speed of Sound*. NACA TN 1032, 1946.

Table 1. Computed Vortex Positions as Function of Wing Roll Angle for Different Angles of Attack

(a) $\alpha = 10°$

ϕ, deg	x_1	y_1	x_2	y_2
−52.5	0.2804	1.1781	0.1073	−0.9208
−45.0	0.3585	1.1027	0.1274	−0.8331
−37.5	0.4289	1.0125	0.1538	−0.7258
−30.0	0.4532	0.9065	0.1819	−0.6394
−22.5	0.4262	0.8063	0.2026	−0.6036
−15.0	0.3767	0.7294	0.2284	−0.6027
−7.5	0.3272	0.6764	0.2537	−0.6170
0	0.2975	0.6843	0.2975	−0.6843
7.5	0.2537	0.6170	0.3272	−0.6764
15.0	0.2284	0.6027	0.3767	−0.7294
22.5	0.2026	0.6036	0.4262	−0.8063
30.0	0.1819	0.6394	0.4532	−0.9065
37.5	0.1538	0.7258	0.4289	−1.0125
45.0	0.1274	0.8331	0.3585	−1.1027
52.5	0.1073	0.9208	0.2804	−1.1781

(b) $\alpha = 15°$

ϕ, deg	x_1	y_1	x_2	y_2
−52.5	0.3897	1.3201	0.1487	−0.8845
−45.0	0.4981	1.2310	0.1800	−0.7591
−37.5	0.5832	1.1191	0.2220	−0.6147
−30.0	0.5844	0.9804	0.2571	−0.5449
−22.5	0.5334	0.8559	0.2805	−0.5462
−15.0	0.4682	0.7622	0.3008	−0.5745
−7.5	0.4083	0.6960	0.3259	−0.6093
0	0.3608	0.6480	0.3608	−0.6480
7.5	0.3259	0.6093	0.4083	−0.6960
15.0	0.3008	0.5745	0.4682	−0.7622
22.5	0.2805	0.5462	0.5334	−0.8559
30.0	0.2571	0.5449	0.5844	−0.9804
37.5	0.2220	0.6147	0.5832	−1.1191
45.0	0.1800	0.7591	0.4981	−1.2310
52.5	0.1487	0.8845	0.3897	−1.3201

Table 1. Continued

(c) $\alpha = 20°$

ϕ, deg	x_1	y_1	x_2	y_2
−45.0	0.6845	−1.3655	0.2358	−0.5673
−37.5	0.7306	−1.1962	0.2896	−0.4154
−30.0	0.6805	−1.0135	0.3148	−0.4200
−22.5	0.6021	−0.8674	0.3275	−0.4730
−15.0	0.5215	−0.7612	0.3413	−0.5301
−7.5	0.4525	−0.6863	0.3641	−0.5812
0	0.4002	0.6303	0.4002	−0.6303
7.5	0.3641	0.5812	0.4525	−0.6863
15.0	0.3413	0.5301	0.5215	−0.7612
22.5	0.3275	0.4730	0.6021	−0.8674
30.0	0.3148	0.4200	0.6805	−1.0135
37.5	0.2896	0.4154	0.7306	−1.1962
45.0	0.2358	0.5673	0.6845	−1.3655

(d) $\alpha = 23°$

ϕ, deg	x_1	y_1	x_2	y_2
−52.5	0.6009	1.2532	0.2052	−0.7316
−45.0	0.7913	1.4581	0.2848	−0.4061
−37.5	0.7683	1.2370	0.3320	−0.3220
−30.0	0.7193	1.0364	0.3480	−0.3723
−22.5	0.6331	0.8813	0.3545	−0.4483
−15.0	0.5482	0.7692	0.3651	−0.5172
−7.5	0.4767	0.6897	0.3867	−0.5753
0	0.4230	0.6292	0.4230	−0.6292
7.5	0.3867	0.5753	0.4767	−0.6897
15.0	0.3651	0.5172	0.5482	−0.7692
22.5	0.3545	0.4483	0.6331	−0.8813
30.0	0.3480	0.3723	0.7193	−1.0364
37.5	0.3320	0.3220	0.7863	−1.2370
45.0	0.2848	0.4061	0.7913	−1.4581
52.5	0.2052	0.7316	0.6009	−1.2532

Table 1. Continued

(e) $\alpha = 25°$

ϕ, deg	x_1	y_1	x_2	y_2
−52.5	0.6699	1.6241	0.2260	−0.6638
−45.0	0.8451	1.5085	0.3208	−0.2951
−37.5	0.8150	1.2601	0.3595	−0.2684
−30.0	0.7412	1.0506	0.3690	−0.3451
−22.5	0.6512	0.8903	0.3714	−0.4344
−15.0	0.5642	0.7747	0.3799	−0.5101
−7.5	0.4914	0.6923	0.4006	−0.5723
0	0.4370	0.6292	0.4370	−0.6292
7.5	0.4006	0.5723	0.4914	−0.6923
15.0	0.3799	0.5101	0.5642	−0.7747
22.5	0.3714	0.4344	0.6512	−0.8903
30.0	0.3690	0.3451	0.7412	−1.0506
37.5	0.3595	0.2684	0.8150	−1.2601
45.0	0.3208	0.2951	0.8451	−1.5085
52.5	0.2260	0.6638	0.6699	−1.6241

(f) $\alpha = 27°$

ϕ, deg	x_1	y_1	x_2	y_2
−52.5	0.7651	1.7346	0.2571	−0.5446
−45.0	0.8815	1.5460	0.3552	−0.2014
−37.5	0.8389	1.2808	0.3862	−0.2215
−30.0	0.7608	1.0641	0.3892	−0.3211
−22.5	0.6679	0.8992	0.3876	−0.4222
−15.0	0.5791	0.7803	0.3941	−0.5041
−7.5	0.5053	0.6953	0.4140	−0.5700
0	0.4504	0.6298	0.4504	−0.6298
7.5	0.4140	0.5700	0.5053	−0.6953
15.0	0.3941	0.5041	0.5791	−0.7803
22.5	0.3876	0.4222	0.6679	−0.8992
30.0	0.3892	0.3211	0.7608	−1.0641
37.5	0.3862	0.2215	0.8389	−1.2808
45.0	0.3552	0.2014	0.8815	−1.5460
52.5	0.2571	0.5446	0.7651	−1.7346

Table 1. Concluded

(g) $\alpha = 30°$

ϕ, deg	x_1	y_1	x_2	y_2
−52.5	0.9161	1.9155	0.3327	−0.2283
−45.0	0.9164	1.5864	0.4021	−0.0925
−37.5	0.8688	1.3081	0.4247	−0.1606
−30.0	0.7873	1.0830	0.4185	−0.2887
−22.5	0.6907	0.9118	0.4105	−0.4060
−15.0	0.5996	0.7884	0.4140	−0.4963
−7.5	0.5245	0.6997	0.4328	−0.5672
0	0.4690	0.6307	0.4690	−0.6307
7.5	0.4328	0.5672	0.5245	−0.6997
15.0	0.4140	0.4963	0.5996	−0.7884
22.5	0.4105	0.4060	0.6907	−0.9118
30.0	0.4185	0.2887	0.7873	−1.0830
37.5	0.4247	0.1606	0.8688	−1.3081
45.0	0.4021	0.0925	0.9164	−1.5864
52.5	0.3327	0.2283	0.9161	−1.9155

(h) $\alpha = 40°$

ϕ, deg	x_1	y_1	x_2	y_2
−52.5	0.9932	2.0498	0.4799	0.1583
−45.0	0.9831	1.6812	0.5384	0.1248
−37.5	0.9468	1.3884	0.5469	−0.0152
−30.0	0.8629	1.1428	0.5127	−0.2057
−22.5	0.7574	0.9536	0.4831	−0.3659
−15.0	0.6610	0.8172	0.4766	−0.4787
−7.5	0.5834	0.7175	0.4915	−0.5636
0	0.5269	0.6381	0.5269	−0.6381
7.5	0.4915	0.5636	0.5834	−0.7175
15.0	0.4766	0.4787	0.6610	−0.8172
22.5	0.4831	0.3659	0.7574	−0.9536
30.0	0.5127	0.2057	0.8629	−1.1428
37.5	0.5469	0.0152	0.9468	−1.3884
45.0	0.5384	−0.1248	0.9831	−1.6812
52.5	0.4799	−0.1583	0.9932	−2.0498

Table 2. Nondimensional Vortex Strengths
for Selected Values of tan α/tan δ

tan α/tan δ	C_k
0	0
0.25	0.3366
0.50	0.4885
0.75	0.5687
1.00	0.6076
1.50	0.6558
2.00	0.6901
3.00	0.7415
3.30	0.7534
4.00	0.7818
5.00	0.8159

REPORT DOCUMENTATION PAGE

Form Approved
OMB No. 0704-0188

1. REPORT DATE *(DD-MM-YYYY)*	2. REPORT TYPE	3. DATES COVERED *(From - To)*
12-2002	Technical Publication	

4. TITLE AND SUBTITLE
A Discrete-Vortex Method for Studying the Wing Rock of Delta Wings

5a. CONTRACT NUMBER

5b. GRANT NUMBER

5c. PROGRAM ELEMENT NUMBER

6. AUTHOR(S)
Gainer, Thomas G.

5d. PROJECT NUMBER

5e. TASK NUMBER

5f. WORK UNIT NUMBER
537-07-22-24

7. PERFORMING ORGANIZATION NAME(S) AND ADDRESS(ES)
NASA Langley Research Center
Hampton, VA 23681-2199

8. PERFORMING ORGANIZATION REPORT NUMBER
L-17796

9. SPONSORING/MONITORING AGENCY NAME(S) AND ADDRESS(ES)
National Aeronautics and Space Administration
Washington, DC 20546-0001

10. SPONSOR/MONITOR'S ACRONYM(S)
NASA

11. SPONSOR/MONITOR'S REPORT NUMBER(S)
NASA/TP-2002-211965

12. DISTRIBUTION/AVAILABILITY STATEMENT
Unclassified - Unlimited
Subject Category 02
Availability: NASA CASI (301) 621-0390 Distribution: Standard

13. SUPPLEMENTARY NOTES
Gainer, Langley Research Center
An electronic version can be found at http://techreports.larc.nasa.gov/ltrs/ or http://techreports.larc.nasa.gov/cgi-bin/NTRS

14. ABSTRACT

A discrete-vortex method is developed to investigate the wing rock problem associated with highly swept wings. The method uses two logarithmic vortices placed above the wing to represent the vortex flow field and uses boundary conditions based on conical flow, vortex rate of change of momentum, and other considerations to position the vortices and determine their strengths. A relationship based on the time analogy and conical-flow assumptions is used to determine the hysteretic positions of the vortices during roll oscillations. Static and dynamic vortex positions and wing rock amplitudes and frequencies calculated by using the method are generally in good agreement with available experimental data. The results verify that wing rock is caused by hysteretic deflections of the vortices and indicate that the stabilizing moments that limit wing rock amplitudes are the result of the one primary vortex moving outboard of the wing where it has little influence on the wing.

15. SUBJECT TERMS
Wing rock; Vortex flow; Discrete-vortex method; Dynamic stability

16. SECURITY CLASSIFICATION OF:			17. LIMITATION OF ABSTRACT	18. NUMBER OF PAGES	19a. NAME OF RESPONSIBLE PERSON
a. REPORT	b. ABSTRACT	c. THIS PAGE			STI Help Desk (email: help@sti.nasa.gov)
					19b. TELEPHONE NUMBER *(Include area code)*
U	U	U	UU	79	(301) 621-0390